

**APPLICATIONS OF ELECTROABSORPTION SPECTROSCOPY
TO ENZYMOLOGY AND MOLECULAR ELECTRONICS**

A Dissertation
Submitted to
the Temple University Graduate Board

In Partial Fulfillment
of the Requirements for the Degree
DOCTOR OF PHILOSOPHY

by
Cornelius Jonathan Van Galen III
August 2023

Examining Committee Members:

Robert Stanley, Advisory Chair, Chemistry Department

Spiridoula Matsika, Chemistry Department

Vincent Voelz, Chemistry Department

Johannes Schelvis, External Member, Montclair State University

ABSTRACT

Absorption spectra of molecules encode structural details of the local electrostatic environment via coupling of the local electric field with charge redistribution through the molecule upon optical excitation. Electroabsorption spectroscopy, also known as Stark spectroscopy, provides a simple method for determining dependence of electronic transition energies on the local field by measuring and interpreting perturbations to the absorption spectrum due to a well-characterized external electric field. In this dissertation, electroabsorption spectroscopy has been utilized, first, to estimate the second-harmonic generation cross section of the intracellular signaling metabolite lumichrome, second, to measure optical band gap tuning of the molecular electronic component perylene diimide by an external electric field, and, third, to exploit optical transition energies of the ubiquitous enzyme cofactor flavin to measure flavoenzyme active site electric fields. Experimental measurements are complemented by time-dependent density functional theory calculations to interpret experimental results and localize charge redistribution within the molecular frame.

Lumichrome is a photodegradation product and catabolite of flavin cofactors that additionally serves as a signaling molecule for plants and bacteria. As a mediator of bacterial quorum sensing, lumichrome is transported across bacterial membranes. While transiting bacterial membranes, the average orientation of the trafficked lumichrome may be sufficiently anisotropic to allow detection by second-harmonic generation spectroscopy, the magnitude of which is a function of charge redistribution upon optical excitation and may be estimated by Stark spectroscopy. Using Stark spectroscopy we

have estimated lumichrome's second harmonic generation cross-section to be approximately 80% that of flavin adenine dinucleotide, which has previously successfully been used as a second-harmonic generation probe.

Perylene diimide is an n-type organic semiconductor that is widely used in organic photovoltaics, light emitting diodes, and other molecular opto-electronics. Electric fields within electronic devices utilizing monomeric and / or aggregated perylene diimide alter the band structure of the chromophore, possibly providing a tunable parameter for the improvement of these devices. Stark spectroscopy has been used to measure tuning of the optical bandgap of monomeric perylene diimide by an external electric field. The centrosymmetry of the molecule causes the difference permanent dipole moment of the first singlet electronic excitation to approach zero. The change in polarizability following excitation is also modest, with the trace of the difference polarizability equal to 42 \AA^3 and the component of the difference polarizability along the transition dipole moment equal to 29 \AA^3 . Electric fields within molecular electronics are on the order of 1 MV/cm. Such an electric field would redshift the S_{10} transition energy of monomeric perylene diimide by 16.25 cm^{-1} , which is less than 0.1% of the transition energy (18500 cm^{-1}).

Flavin adenine dinucleotide and flavin mononucleotide are ubiquitous enzymatic cofactors mediating catalytic transfer of one or two electrons. Flavin cofactors are ubiquitous because of their versatile and tunable reactivity. For example, the two-electron reduction potential of flavin can be continuously tuned through a range of over 400 mV by differing interactions with flavoenzyme active site residues. We have utilized Stark spectroscopy to measure charge redistribution upon optical excitation for the first two

excited states of oxidized flavin in the aprotic, non-polar solvent toluene, with and without a tridentate hydrogen-bonding ligand. In comparing this data with previously reported measurements, we conclude that charge redistribution is independent of solvent polarity. As such, flavin's optical transition energies may be used to indirectly measure flavoenzyme active site electric fields directly from the perspective of the electrostatically-tuned flavin cofactor, enhancing our understanding of flavin-dependent biochemistry.

DEDICATION

This dissertation is dedicated to the years spent
on good ideas that might still work.

ACKNOWLEDGMENTS

Above all else, I have to thank Dr. Stanley for his mentorship these past several years. His undergraduate biochemistry course was my first exposure to the field, and his graduate biochemistry course was my first opportunity to delve deeply into the biochemical literature. It has been a privilege to learn from him via his collaborative approach to training, and I hope he has enjoyed our late afternoon discussions of quantum mechanics and spectroscopy as much as I have. I look forward to remaining friends through the coming years.

I am also grateful to Dr. Spiridoula Matsika and Dr. Vincent Voelz for serving on my Faculty Oversight Committee. The insights and suggestions they have provided each year during my annual FOC meeting have continually helped me to focus and sharpen my research program. Furthermore, I am grateful to them, and to my external reader, Dr. Johannes Schelvis of Montclair State University, for their flexibility in the scheduling of this summer's defense.

A number of other professors were instrumental in my education and training as an undergraduate. Dr. Timothy Sipe at Franklin and Marshall College in Lancaster, PA was a good friend and an excellent teacher. Dr. Rod Andrade provided me with my first research opportunity here at Temple, working on functionalization of macrolide antibiotics. His experimentalist's mantra of "Show me, don't tell me" has stayed with me through the years. Dr. Frank Spano was my professor for thermodynamics, quantum mechanics, and molecular spectroscopy, and also hired me for a summer through the Undergraduate Research Program to study the photophysics of dyes that aggregate upon interaction with amyloid beta. Dr. Spano and his student Nick Hestand, now a professor

at Evangel University in Missouri, taught me to program in FORTRAN and to work with Gaussian, which was the beginning of the computational work included in this thesis. Dr. Vladi Wilent was my professor for Biochemistry Research Techniques, the capstone course for the biochemistry major. I was excited about the material we were learning, and definitely added too much detail to my lab reports and exam free responses (in terrible handwriting to boot), but she encouraged my interest and with Dr. Stanley inspired me to pursue biochemistry professionally. I was lucky enough to work as her teaching assistant in the Spring 2023 semester.

Talking data, science, and not science with my friends in the Stanley group has been a highlight of each day of grad school. David Barnard and Rylee McBride, who preceded me in the group, taught me the ropes and worked with me to improve my ability to communicate science verbally. They helped me prepare for group meetings and my literature seminar slide-by-slide, and even still when preparing and improving a presentation I think of what their comments might be. Nadim Russel's drive and work ethic are infectious, and I thank him for his camaraderie.

I have been fortunate to be able to mentor a number of undergrads in the group, specifically Jared Ford, AJ Azimov, and Anna Freidman. I look forward to seeing the excellent work I know they will continue to do.

Finally, I would like to thank Temple University for awarding me a University Fellowship, as well as the National Aeronautics and Space Administration for funding my Research Assistantships.

My success in graduate school has stemmed from patience, focus, and the loving support of family. Obtaining a PhD in chemistry has been roughly the plan since 1997

when I was six years old and captivated by science-themed educational programming. I have only been able to arrive now at this goal because of the continuous encouragement and support of my parents, Neil and Marianna.

I met Mouy, my wife, in Dr. Serge Jasmin's Organic Chemistry course in 2013. Since that time, Mouy has been my partner and companion through all of my trials and triumphs as a student and scientist. She has helped me to maintain perspective and resolve. This dissertation would not have been possible without her.

TABLE OF CONTENTS

	Page
ABSTRACT.....	ii
DEDICATION.....	v
ACKNOWLEDGMENTS	vi
LIST OF TABLES.....	xi
LIST OF FIGURES	xii
CHAPTER	
1. INTRODUCTION	1
1.1 General Introduction	1
1.2 Specific Applications of Electroabsorption Spectroscopy Presented in this Thesis	4
1.2.1 Stark Spectroscopy of Lumichrome: A Possible Candidate for Stand-Off Detection of Bacterial Quorum Sensing.....	5
1.2.2 Optical Bandgap Tuning of Monomeric Perylene Diimide.....	8
1.2.3 Flavin Charge Redistribution Upon Optical Excitation is Independent of Solvent Polarity.....	12
2. MEASURING AND INTERPRETING ELECTROABSORPTION SPECTRA.....	19
3. STARK SPECTROSCOPY OF LUMICHROME: A POSSIBLE CANDIDATE FOR STAND-OFF DETECTION OF BACTERIAL QUORUM SENSING.....	25
3.1 Overview.....	25
3.2 Sample Preparation and Computational Methods.....	25
3.3 Results.....	28
3.4 Discussion.....	31

4. OPTICAL BAND GAP TUNING OF MONOMERIC PERYLENE DIIMIDE.....	46
4.1 Overview.....	46
4.2 Sample Preparation and Computational Methods.....	46
4.3 Results.....	47
4.4 Discussion.....	49
5. FLAVIN CHARGE REDISTRIBUTION UPON OPTICAL EXCITATION IS INDEPENDENT OF SOLVENT POLARITY.....	57
5.1 Overview.....	57
5.2 Sample Preparation and Computational Methods.....	57
5.3 Results.....	59
5.4 Discussion.....	68
6. NEXT STEPS AND FUTURE DIRECTIONS	88
6.1 Introduction.....	88
6.2 Determining local field magnitude and direction as a function of flavin charge redistribution upon optical excitation and flavin optical transition energies	89
6.3 Comparison of flavoenzyme active site electric fields of <i>E. coli</i> photolyase and <i>S. pastorianus</i> old yellow enzyme	90
7. CONCLUDING REMARKS.....	97
REFERENCES CITED.....	98

LIST OF TABLES

Table	Page
3.1 Fit charge redistribution parameters for lumichrome in dry ethanol at 77K	38
3.2 DFT results for gas phase lumichrome and lumiflavin.....	38
3.3 Molecular geometry of lumichrome optimized in the gas phase	40
3.4 Molecular geometry of lumiflavin optimized in the gas phase.....	41
3.5 First ten excited states of gas phase lumichrome.....	42
3.6 First ten excited states of gas phase lumiflavin	42
3.7 Vector components of theoretical transition and difference dipole moments	44
4.1 First ten excited states of Perylene Orange implicitly solvated in toluene	56
5.1 Comparison of absorption spectra of TPARF and TPARF:DBAP.....	82
5.2 Fit charge redistribution parameters for TPARF and TPARF:DBAP in toluene	82
5.3 Theoretical $ \Delta\vec{\mu}_{fi} $ and ζ_A for Lf and LF:DFAP implicitly solvated in toluene.....	82
5.4 Comparison of flavoenzyme experimental charge redistribution parameters	83
5.5 Molecular geometry of lumiflavin optimized in implicit toluene solvent	84
5.6 Molecular geometry of lumiflavin: diformamidopyridine optimized in implicit toluene solvent	85
5.7 First ten excited states of lumiflavin implicitly solvated in toluene	86
5.8 First ten excited states of lumiflavin:diformamidopyridine implicitly solvated in toluene.....	86
5.9 Transition energies, ΔE_{10} vs. ΔE_{20} , of flavin in different solvents	87
5.10 Solvent dependence of flavin charge redistribution parameters (S_{20}/S_{10})	87
6.1 Flavoenzyme S_{10} and S_{20} transition energies relative to flavin in 2-MTHF	95
6.2 Flavoenzyme active site electric field components relative to $\Delta\vec{\mu}_{10}$ and angle relative to flavin long axis.....	95

LIST OF FIGURES

Figure	Page
1.1 Lumichrome and related compounds.....	17
1.2 Line structure of Perylene Orange	17
1.3 Structure of TPARF ligated to DBAP, with hydrogen bonds indicated.....	18
2.1 An overview of the Stark spectrometer in use in our group	24
3.1 298K and 77K absorption spectra of lumichrome in dry ethanol.....	36
3.2 Lumichrome Stark spectra at two χ angles	37
3.3 Vector diagrams and difference density maps for lumichrome and lumiflavin.....	39
3.4 Standard orientations of lumichrome and lumiflavin	43
3.5 Possible molecular orientations of experimental difference dipole moments	45
4.1 298K and 77K extinction spectra of Perylene Orange, with fit to 77K spectrum	53
4.2 Experimental and fitted Stark spectra.....	54
4.3 Perylene Orange S ₁₀ electronic transition difference density map	55
5.1 298K absorption spectra of TPARF and TPARF:DBAP in toluene.....	76
5.2 77K absorption spectra of TPARF and TPARF:DBAP in toluene.....	77
5.3 Stark spectra of TPARF and TPARF:DBAP in toluene, with fits.....	78
5.4 Vector diagrams of lumiflavin and lumiflavin:diaformamidopyridine	79
5.5 Difference density maps of lumiflavin and lumiflavin:diaformamidopyridine.....	80
5.6 Flavin solvatochromism and electrochromism	81
6.1 Experimental transition and difference permanent dipole moments in flavin molecular frame	93
6.2 Reference frame for determination of local field orthogonal components	94
6.3 Orientation of flavoenzyme electric field unit vectors in the molecular frame	96
6.4 Crystal structures of PL (L) and OYE (R) active sites	96

CHAPTER 1

INTRODUCTION

1.1 General Introduction

Non-covalent intermolecular forces, including hydrogen-binding, the hydrophobic effect, and the various interactions between charged, polar, and polarizable groups, organize the higher order structure of polymeric biomolecules, such as proteins, nucleic acids, carbohydrates, and lipids.¹ These forces mediate the transient interactions among small molecule metabolites and biopolymers that underly cell signaling and communication, and tune the chemical reactivities of enzyme active site groups to optimize biochemical thermodynamics and regulate flux through anabolic and catabolic pathways. Beyond biochemistry, non-covalent intermolecular forces control conformations and tune electronic properties of conjugated polymers,² molecular aggregates,³ and liquid crystals.⁴

Non-covalent intermolecular interactions are primarily electrostatic in nature, meaning that the strength of the interaction between two chemical groups is, via Coulomb's law, a function of the charge distribution of each group and their relative orientation. The potential energy of interaction between two ionic groups can be modelled as the Coulomb potential of interaction between two point charges. Models for pairwise potentials of interaction involving permanent and induced dipoles include additional terms.⁵ Complex distributions of charged, polar and polarizable groups through space, as are present in enzyme active sites and at molecular ligand-binding interfaces,

present complex superpositions of interacting electric potentials that can be simplified concisely and cohesively in terms of the total electric field.⁶

The potential energy of interaction of a polarizable, dipolar molecule with the local electric field evolved by surrounding chemical groups, representing for example the interaction of an enzyme's substrate with the electric field generated by residues of the enzyme active site, is given by the power series expansion⁷

$$V = -\vec{\mu} \cdot \vec{F} - \frac{1}{2} \vec{F} \cdot \vec{\alpha} \cdot \vec{F} \quad (1.1)$$

Here, $\vec{\mu}$ is the permanent dipole moment of the molecule, $\vec{\alpha}$ is the dipolar polarizability of the molecule, and \vec{F} is the dipolar electric field. For most biochemically relevant systems and field magnitudes, higher order polarizabilities contribute negligibly to the total potential energy of interaction.

Improving our understanding of the mechanism of electrostatic tuning of biochemical processes via perturbations by the local electric field requires knowledge of the electric field on the molecular scale.⁶ For systems absorbing or emitting light, the electric field interacts with the unique charge distributions of the ground and excited states differently due to the redistribution of charge upon the transition between states.⁸ For the transition from an initial state i to a final state f , the change in the transition energy ΔE_{fi} due to the local field \vec{F} is

$$\begin{aligned} \Delta E_{fi} &= \left(\left(-\vec{\mu} \cdot \vec{F} - \frac{1}{2} \vec{F} \cdot \vec{\alpha} \cdot \vec{F} \right)_f - \left(-\vec{\mu} \cdot \vec{F} - \frac{1}{2} \vec{F} \cdot \vec{\alpha} \cdot \vec{F} \right)_i \right) \\ &= -\Delta \vec{\mu}_{fi} \cdot \vec{F} - \frac{1}{2} \vec{F} \cdot \Delta \vec{\alpha}_{fi} \cdot \vec{F} \quad (1.2) \end{aligned}$$

This perturbation of the transition energy of an atom or molecule due to the interaction with an external electric field is termed electrochromism, or the Stark effect, after the German physicist Johannes Stark, who observed splitting of hydrogen atomic emission lines in an external electric field in 1913.⁹ The measurement of the perturbation of an external electric field on the absorption (emission) spectrum of an atom or molecule is termed electroabsorption (electroemission) spectroscopy, or absorption (emission) Stark spectroscopy. In this work electrochromism is used interchangeably with the Stark effect, and electroabsorption spectroscopy is used interchangeably with Stark spectroscopy. The use of “Stark” is more common historically, especially in the chemical literature, but the alternative names have the benefit of actually describing the physical observable and avoid the fallacy that simply observing Nature endows ownership.

Initial applications of electroabsorption and electroemission spectroscopies in the first half of the twentieth century focused on analysis of gas phase systems, and contributed to the early development of quantum theory.¹⁰ A model for understanding electrochromism of isotropically distributed chromophores immobilized in the condensed phase was developed by Wolfgang Liptay in the 1960s¹¹, extending the technique to a much larger set of chemically and physically interesting systems. Liptay’s formalism interprets the field-dependent change in the absorption band shape of a sample of immobilized, usually isotropically oriented chromophores excited in the presence of well-characterized external electric field in terms of a number of molecular parameters characterizing the difference in the chromophore’s charge distribution following excitation. These parameters include the magnitude of the molecule’s difference

permanent dipole moment upon excitation from the ground state $|0\rangle$ to the excited state $|n\rangle$, $|\Delta\vec{\mu}_{n0}|$, the angle between the difference permanent dipole moment $\Delta\vec{\mu}_{n0}$ and the transition dipole moment \vec{m}_{n0} , ζ_{n0} , the trace of the difference polarizability tensor, $Tr\Delta\vec{\alpha}_{n0}$, and the component of the difference polarizability tensor parallel to the transition dipole moment, $\vec{m}_{n0} \cdot \Delta\vec{\alpha}_{n0} \cdot \vec{m}_{n0}$. The construction of the electroabsorption spectrometer, as well as the method of measuring and interpreting electroabsorption spectra, are given in Chapter 2.

By measuring changes in the absorption spectrum of an isotropically-distributed chromophore due to perturbation by a well-characterized field and determining the chromophore's characteristic charge redistribution parameters, it is possible to introduce the chromophore to a new environment, such as the active site of an enzyme or binding interface of a receptor, measure the spectral perturbation of the chromophore induced by the novel environment, and extract the information regarding the magnitude and direction of the local electric field via the chromophore's known charge redistribution parameters.

1.2 Specific Applications of Electroabsorption Spectroscopy Presented in this Thesis

A number of excellent reviews summarize the wide variety of systems previously studied using Stark spectroscopy.^{6, 7, 12, 13} The Stanley group, specifically, has previously utilized electroabsorption spectroscopy to study the excited state structures of enzymatic flavin cofactors and their derivatives in simple solvents¹⁴⁻¹⁶ and bound by flavoenzymes¹⁷⁻¹⁹, as well as of fluorescent nucleic acid base analogs.²⁰⁻²² In this thesis, I will present applications of electroabsorption spectroscopy in evaluating, first, the utility of the flavin photodegradation product lumichrome as a possible candidate for stand-off

detection of bacterial quorum sensing via second harmonic generation,¹⁶ second, the electro-optical band gap tunability of the n-type organic semiconductor perylene diimide in the monomeric state, and, third, the dependence of charge redistribution in flavin upon optical excitation on solvent polarity.²³

1.2.1 Stark Spectroscopy of Lumichrome: A Possible Candidate for Stand-Off Detection of Bacterial Quorum Sensing

Lumichrome (7,8-dimethyl-1H-benzo[g]pteridine-2,4-dione or LC) is a tautomer of flavin (7,8-dimethylbenzo[g]pteridine-2,4(3H,10H)-dione or 7,8-dimethylisoalloxazine or FL) in which the N10 hydrogen shifts to the N1 atom with a resultant decrease in conjugation of the tricyclic aromatic system (see Figure 1.1). LC is not enzymatically synthesized directly, but its biological precursor riboflavin (N10-ribytl-7,8-dimethylisoalloxazine or RBF) is biosynthesized in copious amounts by plants and bacteria by RBF synthase.²⁴ Animals lack the riboflavin synthase enzyme and must obtain RBF by ingestion.²⁵ Lumichrome is one of the primary products of the facile photodegradation of riboflavin and its derivatives flavin mononucleotide (FMN) and flavin adenine dinucleotide (FAD).²⁶ Additionally, LC is a product of the enzymatic catabolic degradation of riboflavin.²⁷

While FAD and FMN are critical enzymatic cofactors due to their favorable reduction potentials in both ground and electronic excited states^{28, 29} for performing electron-transfer mediated reactions, lumichrome has not (yet) been found in this role. Its ground state reduction potential, which has only recently been determined by cyclic voltammetry, is significantly more negative than oxidized RBF,³⁰ and more negative than

most biological redox cofactors in the ground state, including nicotinamide cofactors³¹.

This suggests a rationale for it not being found as a redox cofactor.

The facile photodegradation of oxidized vitamin B₂ and its derivatives efficiently produces lumichrome with the concomitant loss of the ribityl side chain, probably through a triplet-induced electron transfer reaction.^{26, 32} Since flavins are ubiquitous in cellular biochemistry,²⁹ LC can build up in the cell with a variety of physiological consequences, principally that of a feedback regulator of riboflavin synthesis or catabolism, which proceeds via riboflavin hydrolase,^{27, 33, 34} an enzyme that has been known since the 1940s.³⁵

Another recent discovery is that lumichrome inhibits riboflavin transport in rat³⁶ and human³⁷⁻⁴⁰ retinæ, possibly leading to riboflavin deficiency and ocular issues.^{36, 38, 40, 41} Studies on the human retina have shown similar results.⁴² Lumichrome's apparent deleterious effects on cellular function render lumichrome transport essential. For this purpose, the RBF transport protein dodecin also binds LC with high affinity, presumably for cellular waste disposal.⁴³ Coincidentally, the wide adoption of white light-emitting diode (LED) lamps with significant blue intensity appears to have accelerated the rate of RBF/FMN photodegradation and concomitant increase in LC formation in the retina.⁴⁴ Also of potential consequence is the use of blue light LEDs for treating seasonal affective disorder and jetlag.^{45, 46}

FMN is utilized as a genetically encoded singlet oxygen generator (SOG) in miniSOG proteins, parts of LOV domains^{28, 47, 48} in which a molecule of FMN absorbs blue light to generate ¹O₂ with high yield. The inevitable photodegradation of the FMN to

LC gives a LC-miniSOG with a singlet O₂ yield an order of magnitude larger than for FMN-miniSOG, given LC's high intersystem crossing rate.⁴⁹

LC functions as a signaling molecule. In concert with RBF, it can affect plant growth at the nanomolar level in a species-dependent manner.⁵⁰ When LC is secreted outside of the cell, it appears to provide a bacterial quorum sensing signal leading to biofilm formation.⁵¹⁻⁵³ Since biofilms of pathogenic organisms represent a human health risk, their early detection would be an important achievement. LC exhibits low fluorescence emission⁵⁴ which is advantageous for second-harmonic generation (SHG) detection.

Since secretion of LC would require passage through the cell membrane, interface-sensitive stand-off spectroscopic techniques should produce sensitive optical signatures. We hypothesize that lumichrome has a sufficiently large difference dipole moment, $\Delta\vec{\mu}_{fi} = \vec{\mu}_f - \vec{\mu}_i$, to facilitate noninvasive spectroscopic stand-off detection of biofilm formation⁵¹⁻⁵³ through second-harmonic generation.^{55, 56} SHG efficiency requires a large β (hyperpolarizability) value, which correlates positively with the magnitude of the difference dipole moment. The molecular prerequisites for efficient SHG have been discussed in the literature.⁵⁷

The only experimental data on LC charge redistribution are the molecular relaxation studies on methylated LC derivatives by Shcherbatska *et al.*, giving a $\Delta\vec{\mu}_{10} \sim 1 D$.⁵⁸ Here, we present low-temperature absorption and Stark spectra to determine the degree and direction of charge redistribution in the two lowest-energy bright excited electronic states of lumichrome. Density functional theory calculations at

the TD-B3LYP/6-311+G(2d,p) level of theory were used support these assignments. The hyperpolarizability of LC was estimated relative to FAD, a tautomeric derivative. The $|\Delta\vec{\mu}_{10}|$ obtained here confirms the result obtained by Shcherbatska *et al.*, and is ~30% lower than that of flavin, suggesting that LC would be a modest probe of bacterial quorum sensing. However, the charge-transfer character of higher excited transitions, we will argue, will provide for stand-off detection of biofilms.

1.2.2 Optical Bandgap Tuning of Monomeric Perylene Diimide

Perylene diimide (PDI) and its derivatives are among the most promising building blocks for next-generation molecular electronics poised to reduce the cost of efficient organic solar cells (OSCs)⁵⁹, organic light-emitting diodes (OLEDs)⁶⁰, organic field effect transistors (OFETs)⁶¹, and medical photoactive diagnostic and therapeutic agents⁶². PDIs possess such wide applicability for a number of reasons. PDI molecular electronics are solution-processable and are characterized by favorable chemical and photostability.^{63, 64} From a functional perspective, PDIs exhibit strong visible absorption, high fluorescence quantum yields, large Stokes shifts, high electron mobilities, and a HOMO / LUMO band structure conducive to action as an n-type semiconductor.^{63, 64} Many of the properties of PDIs responsible for their wide applicability emerge as PDI monomers aggregate to form higher order structures stabilized covalently⁶⁵ or non-covalently⁶⁶. For example, a recent theoretical and experimental paper by Oleson *et al.* demonstrates that altering substituents of the PDI core changes molecular packing of derivatized PDI aggregates sufficiently to shift the relative magnitudes of long-range Coulombic and short-range charge transfer excitonic couplings, selecting between a red-shifted, brightly

emissive J-aggregate state and a blue-shifted, dimly emissive H-aggregate state.⁶⁷ Gregg *et al.* have shown that doping an excitonic semiconductor PDI aggregate with reduced anionic PDI covalently linked to a cationic countercharge causes an exponential increase in conductivity with respect to dopant concentration.⁶⁸

An essential step in expanding applicability of PDI-based organic semiconductors is improving tunability of the molecular HOMO/LUMO band gap, the energy required to promote an electron from a material's localized valence band to delocalized conduction band.^{69, 70} Because the working principles of molecular electronic devices such as OSCs, OFETs, and OLEDs involve generation of internal electric fields varying in space and time,^{61, 71-73} the electric field dependence of PDI's HOMO/LUMO electro-optical band gap is a logical parameter for optimizing PDI band gap engineering. The capacity of internal electric fields to dynamically tune band gaps of single- and many-molecule molecular electronics *in situ* has been explored extensively,⁷⁴⁻⁸⁴ yet the dependence of the optical band gap of PDI on the local electric potential has, to our knowledge, not been reported. In this study, therefore, we determine the electro-optical band gap tunability of monomeric perylene diimide using Stark spectroscopy.

Ara and Ahmed published a Stark absorption spectroscopic study of the perylene core of PDI in a polymethyl methacrylate (PMMA) film,⁸⁵ in addition to a Stark fluorescence study by Ara *et al.* of perylene also in PMMA.⁸⁶ The concentrations of perylene in PMMA in these two studies ranged from a mole percentage of perylene of 0.1% to a mole percentage of 3.0%. As aggregation of perylene in a PMMA thin film begins below a perylene concentration of 0.1%, the charge redistribution parameters

obtained in these studies are for a mixture of monomeric and aggregated perylene.⁸⁷ Perylene is a centrosymmetric molecule, giving a negligible difference dipole moment. The trace of the difference polarizability tensor, however, is non-zero. Ara and Ahmed report that the trace of the difference polarizability tensor for the first singlet excitation of the mixed perylene aggregate in PMMA is 10.07 \AA^3 for a perylene mole percentage of 3.0%,⁸⁶ a modest change in polarizability upon excitation. Aggregation should increase polarizability relative to the monomer, meaning that the independent polarizability of the perylene monomer should be less than 10 \AA^3 . For comparison, the change in polarizability for the S_{10} transition of enzyme-bound flavin mononucleotide, a similarly rigid but asymmetric chromophore with 70% the number of aromatic π -electrons of perylene, is 23 \AA^3 , assuming a local field correction factor for the protein environment of 1.5.⁸⁸ Shen *et al.* have published a Stark absorption study of crystalline 3,4,9,10-perylenetetracarboxylic dianhydride, a structural analog of PDI in which the nitrogen atoms are substituted by oxygen atoms, but this study focused on characterizing exciton formation in the molecular crystal.⁸⁹

We have specifically selected the functionalized PDI N,N'-bis(2,6-diisopropylphenyl)-3,4,9,10-perylenetetracarboxylic diimide (Figure 1.2), commonly called Perylene Orange (PO) or Lumogen Orange (LO), dissolved in anhydrous toluene for this Stark absorption spectroscopy study. Perylene Orange is a derivative of PDI with diisopropylphenyl substituents of the imide nitrogen atoms. Substituents to the imide nitrogen atoms and/or the otherwise hydrogenated perylene carbons tune the photophysical characteristics and reactivity of individual PDI molecules, and also

determine the molecular packing arrangement of PDI aggregates.⁹⁰⁻⁹³ Perylene Orange was selected for this study because it remains monomeric in chloroform below a concentration of 2 mM.⁹⁴ Toluene is less polar than chloroform,⁹⁵ so the predominately aromatic and hydrophobic Perylene Orange should be monomeric in toluene at a concentration of approximately 1 mM, permitting high signal-to-noise Stark spectra to be captured. It is preferable to determine the electro-optical band gap tunability of the PO monomer prior to that of an aggregate because photophysical attributes of the aggregate are influenced by the specific composition and packing arrangement of a given aggregate. The photophysical attributes of the monomer represent the central characteristics of the material without the imprint of a particular aggregate morphology. Also, the vibronic structure of the absorption spectrum of PO has been well-characterized both experimentally and theoretically.^{96, 97} In conjunction with transition dipole moment vector components calculated using density functional theory, the attributes of the difference polarizability given by the Liptay analysis could allow future study of correlation of changes in the electronic structure upon excitation to curvature of the nuclear potential energy surfaces of normal modes strongly coupled to the electronic transition. Finally, PO is a standard chromophore used in the design and optimization of luminescent solar concentrators, an emerging technology that may play a key role in reducing the cost of solar energy.⁹⁸⁻¹⁰⁰

1.2.3 Flavin Charge Redistribution upon Optical Excitation is Independent of Solvent Polarity

Flavin mononucleotide (FMN) and flavin adenine dinucleotide (FAD) are pervasive enzymatic cofactors connecting two-electron and one-electron redox pathways by cycling in the electronic ground state through five biologically-relevant protonation-oxidation states: oxidized quinone, one-electron reduced anionic semiquinone, protonated neutral semiquinone, two electron-reduced anionic hydroquinone, and protonated neutral hydroquinone¹⁰¹⁻¹⁰⁴. These cofactors are also capable of photoinduced electron transfer, as in the case of DNA Photolyase (PL)¹⁰⁵, a bacterial enzyme that utilizes a quantum of blue light to correct UV-induced DNA lesions, and Fatty-Acid Photodecarboxylase (FAP)¹⁰⁶, a microalgal enzyme decarboxylating fatty acids to yield an aliphatic product. Flavin cofactors have recently been found to couple endergonic and exergonic reduction of separate substrates via electron bifurcation¹⁰⁷, and participate in a plethora of covalent catalytic mechanisms¹⁰⁸. Beyond catalysis, flavin cofactors mediate blue light photoreception¹⁰⁹ in Blue-Light Sensing Using FAD (BLUF) domains¹¹⁰, Light-Oxygen-Voltage (LOV) domains¹¹¹, Cryptochromes¹¹², and the intermediate CRY-DASH¹¹³, which exhibits both photoreception and limited DNA Photolyase functionalities. One reason that flavin cofactors are so ubiquitous is that their ground and excited-state reduction potentials, already usefully poised for exchanging electrons among common metabolites, are electrostatically tunable by selective perturbation from flavoprotein active site's charged and polar residues¹¹⁴⁻¹²⁰. The ground-state two-electron reduction potential of flavin at physiological pH is continuously tunable through range of over 500 mV¹²¹. Under biochemical standard conditions, this 500 mV range corresponds to a

difference in free energy of more than 70 kJ/mol. For comparison, hydrolysis of one mole of ATP under biochemical standard conditions releases 30.5 kJ¹²².

Expanding the flavin reactivity vocabulary is an attractive target for developing novel enzymes to accomplish industrially-important reactions in an efficient and sustainable manner, not least of all because there is such an expansive natural library of flavoenzymes from which to begin rational (re-)design and /or directed evolution¹²³⁻¹²⁹. Doing so requires understanding the mechanism of electrostatic tuning of flavin reactivity, which in turn requires simple and accurate methods of measuring flavoenzyme active site tuning electric fields directly from the perspective of the tuned flavin cofactor¹¹⁴. Stark spectroscopy can be used to translate perturbations in spectroscopic observables to magnitudes and directions of perturbing local electric fields.⁸ By measuring the change in molar extinction of a chromophore as a function of a well-characterized externally-applied electric field, it is possible to fit the difference extinction as a weighted sum of the zeroth-, first-, and second-derivatives of the unperturbed extinction spectrum, and, using the Liptay formalism for electrochromism¹¹, extract a series of parameters encoding the redistribution of charge throughout the molecular framework upon optical excitation. In transitions from the ground state to the n th excited state, these charge redistribution parameters include the magnitude of the difference permanent dipole moment, $|\Delta\vec{\mu}_{n0}| = \vec{\mu}_n - \vec{\mu}_0$, the angle between the difference permanent dipole moment and the transition dipole moment, ζ_A , the trace of the difference polarizability tensor, $Tr\Delta\bar{\alpha}_{n0}$, and the component of the difference polarizability tensor along the transition dipole moment, $\vec{m} \cdot \Delta\bar{\alpha}_{n0} \cdot \vec{m}$. The fitted charge

redistribution parameters can then be used to correlate spectroscopic shifts in transition energy to the magnitudes and directions of perturbing local electric fields inducing the shifts. Additionally, Stark spectroscopy provides information regarding the flavin excited state charge distribution that is otherwise challenging to measure, with implications for better understanding the structure and function of light-dependent flavoproteins, as well as testing the accuracy of computational methods to reproduce flavin experimental values.¹³⁰

Our group has previously used Stark spectroscopy to study flavins and flavin analogs¹⁵ in the simple solvents ethanol, butanol, and 2-methyltetrahydrofuran¹⁴, glycerol/buffer mixtures,¹³¹ and in the flavoenzymes *E. coli* photolyase¹³² and *S. pastorianus* old yellow enzyme¹⁹. The broad trend in this work is that the difference dipole moments of the flavin S₁₀ and S₂₀ transitions are independent of the local environment, within experimental uncertainty, but that the difference polarizability does, variably, depend on the local environment. The trace of the difference polarizability of the S₁₀ transition decreases with increasing polarity from $Tr\Delta\bar{\alpha}_{10} = 22 \text{ \AA}^3 f^2$ in 2-methyltetrahydrofuran, to $17 \text{ \AA}^3 f^2$ in butanol, to $14 \text{ \AA}^3 f^2$ in ethanol, where f is the local field correction factor, a quantity that increases with increasing solvent dielectric constant.¹³³ Similarly, the trace of the difference polarizability of the S₂₀ transition decreases with increasing solvent polarity, from $Tr\Delta\bar{\alpha}_{20} = 162 \text{ \AA}^3 f^2$ in 2-methyltetrahydrofuran, to $149 \text{ \AA}^3 f^2$ in butanol, to $79 \text{ \AA}^3 f^2$ in ethanol. In old yellow enzyme, the S₂₀ trace difference polarizability, $198 \text{ \AA}^3 f^2$, is greater than that of the S₁₀, $51 \text{ \AA}^3 f^2$, while in photolyase, the S₂₀ trace difference polarizability, $57 \text{ \AA}^3 f^2$, is less than

that of the S_{10} , $134 \text{ \AA}^3 f^2$. It is logical that the difference polarizability is more sensitive to the local environment than is the difference dipole moment, as the difference polarizability is, roughly, the derivative of the difference dipole moment with respect to the local electric field, and the second derivative of the change in energy of the transition with respect to the local electric field.

In order to interpret these trends in the dependence of flavin's charge redistribution upon optical excitation on the local environment, it is necessary to obtain a baseline measurement of flavin's root electro-optical charge redistribution parameters in a minimally-interacting, non-perturbing, and, most importantly, non-hydrogen-bonding, environment. To analogously study the reduction potential of flavin in a similarly non-interacting environment, Cerda *et al.* synthesized the derivatized flavin tetraphenylacetyl riboflavin (TPARF), which, in contrast to FAD, FMN, and riboflavin, is soluble in benzene to greater than 250 mM^{134} . The researchers found that the two-electron reduction potential of TPARF in benzene was -1252 mV versus ferrocene, 72 mV more negative than that of TPARF in dichloromethane, a solvent which is capable of weakly hydrogen bonding to the diazadiene nitrogen atoms and diimide carbonyls of the flavin heterocycle. By introducing the tridentate hydrogen bonding ligand dibenzylamidopyridine (DBAP) to TPARF in benzene, the researchers found that the two-electron reduction potential shifts $+100 \text{ mV}$, indicating that hydrogen bonding to the flavin diimide moiety preferentially stabilizes the charge distribution of the reduced flavin over that of the oxidized flavin. Structures of TPARF and DBAP, with hydrogen bonds indicated, are given in Figure 1.3. The solubility of TPARF in the non-polar, glass-forming solvent toluene provides a

unique system to study charge redistribution upon optical excitation of flavin in a non-interacting molecular environment. Furthermore, the addition of DBAP allows analysis of the role of specific hydrogen bonds in tuning differences between flavin's ground and excited state electronic structures.

To these ends, we have performed Stark spectroscopy on TPARF and TPARF:DBAP in toluene, and analyzed the results in terms of complementary TD-DFT calculations and in light of previous Stark spectroscopic analyses of flavins in different environments.

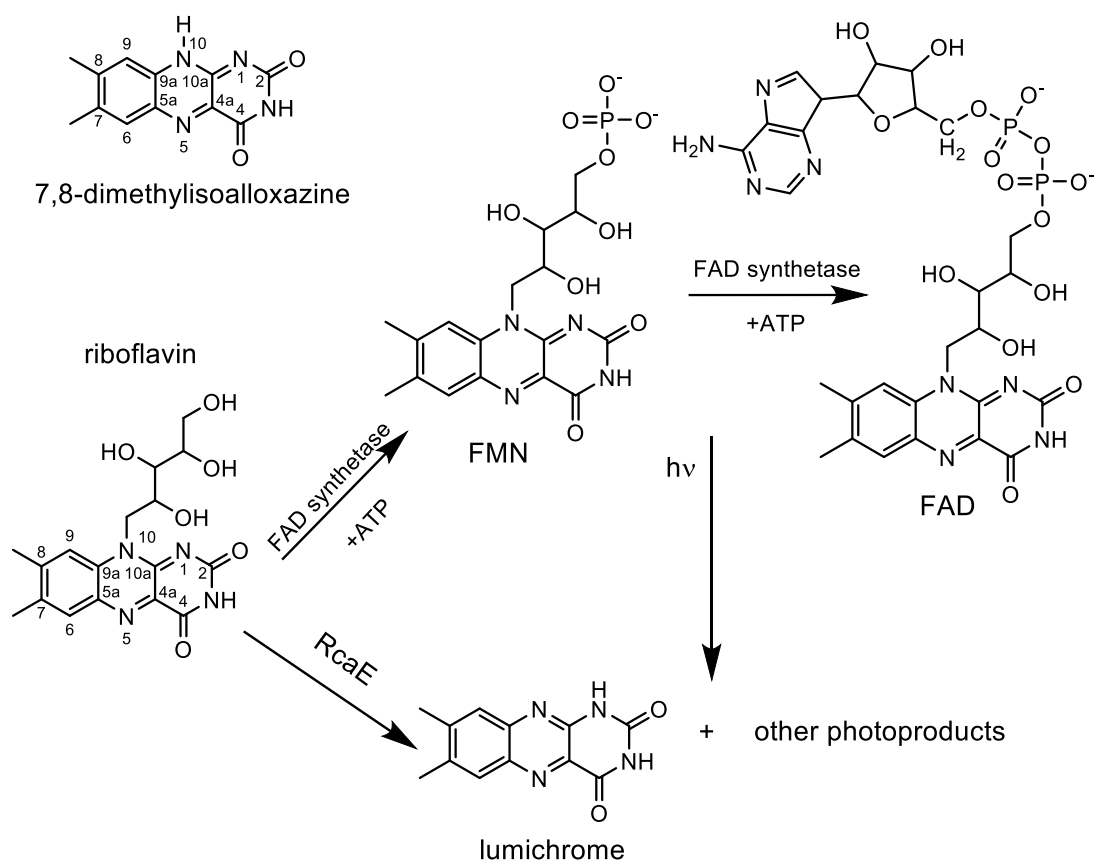


Figure 1.1. Lumichrome and related compounds. Lumichrome and other degradation products are generated from riboflavin, FMN, and FAD through photodegradation and through catabolism of riboflavin by the enzyme riboflavin hydrolase in bacteria.

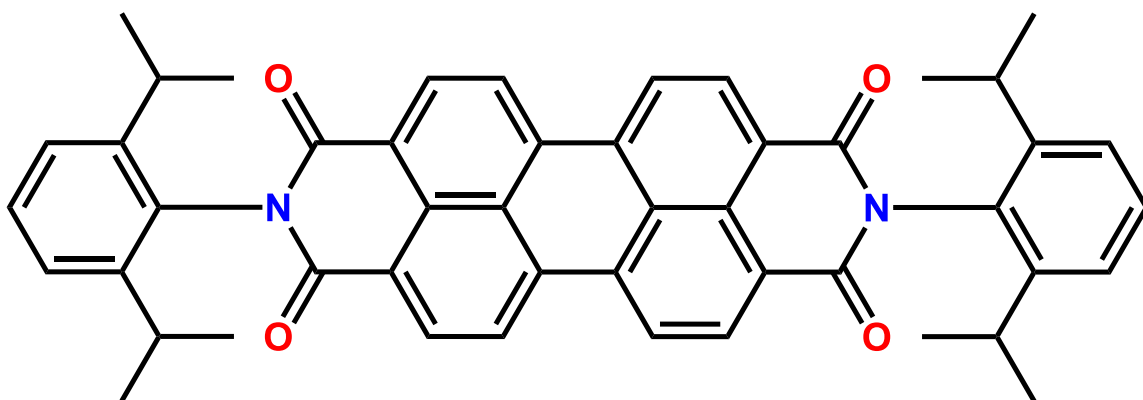


Figure 1.2. Line structure of Perylene Orange. Line structure of N,N'-Bis(2,6-diisopropylphenyl)-3,4,9,10-perylenetetracarboxylic diimide (Perylene Orange).

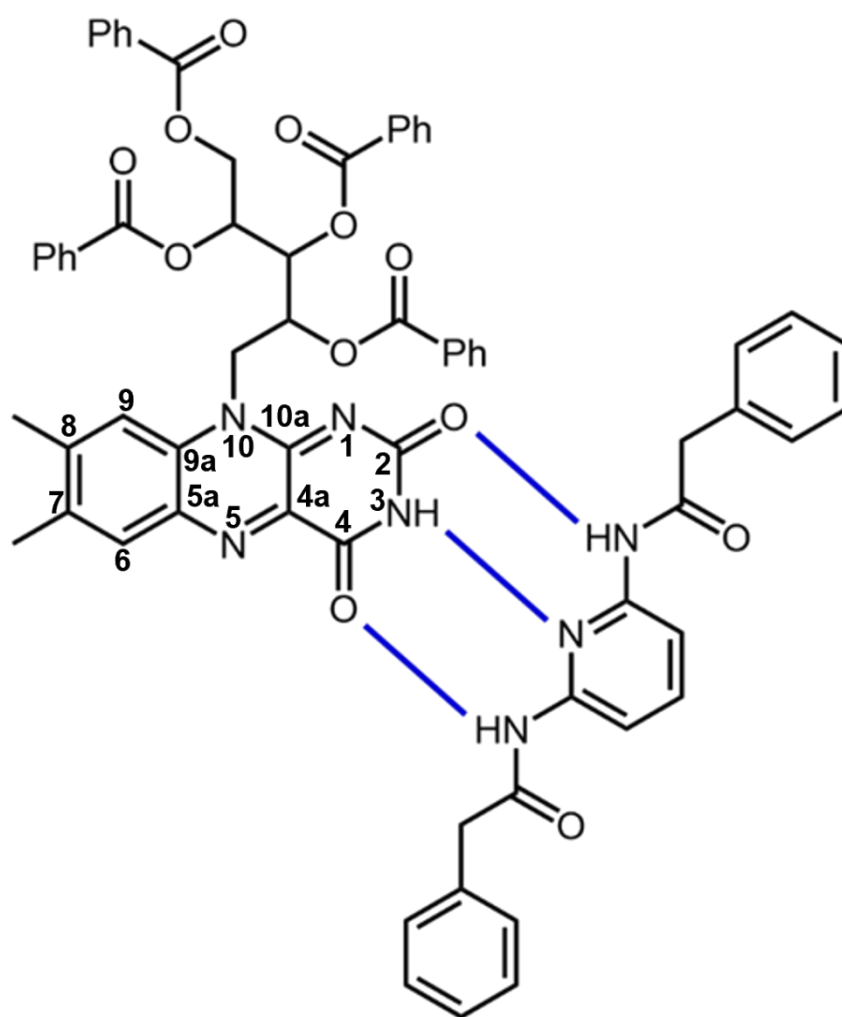


Figure 1.3. Structure of TPARG ligated to DBAP, with hydrogen bonds indicated.

CHAPTER 2

MEASURING AND INTERPRETING ELECTROABSORPTION SPECTRA

The Stark spectrometer has been previously described in detail.^{135, 136} Briefly, emission from a 300 W Xe arc lamp (Oriel) is focused upon the entrance slit of a 1/8 m monochromator (CVI) with a 2 nm bandpass and a wavelength accuracy of ± 0.1 nm. Light exiting the monochromator is then coupled into a 1 m long, 1.000 mm diameter solarized fiber optic (Edmund Optics) that projects the beam through an adjustable Glan-Taylor polarizer onto a lens, which in turn focuses the monochromatic light into the Stark cuvette, itself immersed in liquid nitrogen within a dual-chambered cryostat (Janis). After passing through the sample cuvette, the light is focused onto an unbiased silicon photodiode (Hamamatsu S1226-5BQ) connected to a Keithley 427 current amplifier, in turn connected to a lock-in amplifier, as described below.

The Stark cuvette is constructed of two Corning boro-aluminosilicate glass slides (1.91 cm x 2.54 cm x 0.7 mm), each of which is coated on one side with a transparent, conductive coating of indium tin oxide (ITO, 70-100 Ω /cm, Delta Technologies). The conductive surfaces of the two offset slides are separated by Kapton spacers with a thickness of either 25 μ m or 50 μ m. The shorter pathlength enables formation of a better glass at 77K. The space between the two ITO surfaces serves as the capacitive cuvette, and, after being filled with the sample of interest, is spring-clipped to a cold finger and immersed in the liquid nitrogen bath of the cryostat. The cold finger is designed to be able to be rotated so that the experimentally important χ parameter, the angle between the

polarization vector of the probe beam and the applied electric field, may be accurately controlled.

The cuvette is connected via copper leads to a TREK 609 High Voltage Amplifier. A Stanford Research Systems SR830 digital lock-in amplifier is used to generate a sinusoidal variable amplitude waveform at 3.5 kHz up to approximately 1.500 V_{RMS} . This waveform is amplified by the TREK 609 by 10^3 to give an electric field at the sample of up to 300,000 V/cm for an input voltage of 1.060 V_{RMS} and pathlength of 47 μm . Phase-sensitive detection at the second harmonic of the 3.5 kHz waveform gives the difference in the intensity of the transmitted light as a function of the sinusoidal electric field. Because the field-induced change in transmission is typically on the order of 10^{-6} , a measurement of the transmitted intensity, I_0 , can be made simultaneously by digitizing the amplified photocurrent using a 16-bit analog-to-digital converter (National Instruments PCI-6036E).

The low-temperature absorption spectrum was also measured in the same cuvette and spectrometer using a 1 kHz optical chopper (ThorLabs) to modulate the probe beam for lock-in detection of the transmitted intensity at the 1st harmonic of the chopper frequency. The blank for the low temperature absorption spectrum, measured separately, consists of the glass-forming solvent alone.

Stark spectra were recorded at applied fields ranging from of 2.4×10^5 V/cm to 3.2×10^5 V/cm at both $\chi=55^\circ$ and $\chi=90^\circ$. Cooling from 298K to 77K causes the glass-forming solvent to contract, leading to an increase in the concentration of studied chromophore. The degree of solvent contraction upon freezing is determined by filling a

100 μm demountable quartz cuvette 75% with the solvent of interest, marking the level of fill, immersing the cuvette in liquid nitrogen, and measuring the change in height of the frozen solvent in the cuvette using a NIST-traceable digital micrometer. Ethanol exhibits a solvent contraction of 20%, and toluene exhibits a solvent contraction of 16%. Aqueous 8M LiCl and 1:1 water-glycerol do not change in volume measurably upon freezing. Stark and low-temperature absorption spectra are scanned in equal-energy steps, as the scanned transitions are linear in energy, not wavelength. An overview of the absorption Stark spectrometer are provided in Figure 2.1.

Stark spectra are interpreted using the Liptay formalism.¹¹ The energy-weighted change in extinction for an immobilized, isotropically distributed population of chromophores due to the presence of an applied electric field is modelled as a weighted sum of the zeroth, first, and second derivatives of the energy-weighted extinction in the absence of the field,

$$\frac{\Delta\varepsilon(\bar{\nu})}{\bar{\nu}} = (f_c |\vec{F}|)^2 \left\{ A_\chi \left(\frac{\varepsilon(\bar{\nu})}{\bar{\nu}} \right) + \frac{B_\chi}{15ch} \frac{d}{d\bar{\nu}} \left(\frac{\varepsilon(\bar{\nu})}{\bar{\nu}} \right) + \frac{C_\chi}{30c^2h^2} \frac{d^2}{d\bar{\nu}^2} \left(\frac{\varepsilon(\bar{\nu})}{\bar{\nu}} \right) \right\} \quad (2.1)$$

where $\frac{\Delta\varepsilon(\bar{\nu})}{\bar{\nu}}$ is the energy-weighted change in extinction for $\bar{\nu} = \frac{1}{\lambda}$, f_c is the local field correction factor, $|\vec{F}|$ is the magnitude of the applied external electric field, $\frac{\varepsilon(\bar{\nu})}{\bar{\nu}}$ is the energy-weighted extinction in the absence of the electric field, c is the speed of light, and h is Planck's constant. The A_χ , B_χ , and C_χ terms weighting the different derivatives are functions of molecular quantities characterizing charge redistribution upon optical excitation, and of the experimental parameter χ defined above.

The A_χ term is a function of the polarizability and hyperpolarizability of the molecular transition dipole moment \vec{m} . Because these quantities are small for most chromophores, the A_χ term is usually orders of magnitude lower than the B_χ and C_χ terms, making the contribution of the zeroth-derivative term to the Stark spectrum negligible.

The B_χ term, weighting the first derivative component of the Stark spectrum, describes

$$B_\chi \approx \frac{5}{2} Tr \Delta \bar{\alpha}_{n0} + (3 \cos^2 \chi - 1) \left(\frac{3}{2} \vec{m}_{n0} \cdot \Delta \bar{\alpha}_{n0} \cdot \vec{m}_{n0} - \frac{1}{2} Tr \Delta \bar{\alpha}_{n0} \right) \quad (2.2)$$

the change in polarizability upon excitation. In Eqn. 2 above, $Tr \Delta \bar{\alpha}_{n0}$ is the trace of the difference polarizability tensor for the excited versus ground state of the molecule, and $\vec{m}_{n0} \cdot \Delta \bar{\alpha}_{n0} \cdot \vec{m}_{n0}$ is the component of the difference polarizability that is parallel to the transition dipole moment. Polarization of the chromophore by the applied external electric field lowers the energy of the ground and excited states, leading to a contribution to a first-derivative line shape in the Stark spectrum.

The C_χ term, weighting the second derivative component of the Stark spectrum, is a function of $\Delta \vec{\mu}_{n0}$, the change in permanent dipole moment of the molecule following excitation, and of ζ_{n0} , the angle between the difference permanent dipole moment and the transition dipole moment.

$$C_\chi = |\Delta \vec{\mu}_{n0}|^2 \{5 + (3 \cos^2 \chi - 1)(3 \cos^2 \zeta_{n0} - 1)\} \quad (2.3)$$

Coupling of the external field to the difference permanent dipole moment can shift the excitation energy to higher or lower values depending on the orientation of the molecule to the field, contributing a second derivative line shape to the Stark spectrum.

The Stark and low temperature absorption spectra were simultaneously fit using an in-house MATLAB¹³⁷ program called STARKFIT. Using this program, the low temperature absorption spectrum is first fit to a sum of Gaussian functions. These Gaussian functions are not physically significant, but are useful because of their analytical differentiability. The number of Gaussians used to fit a given transition is the minimum number required to produce random residuals. The program then performs a simultaneous weighted non-linear fit to the Stark and low temperature absorption spectra. The weighting factor instructs the program to bias the fit towards minimizing the Stark versus low-temperature absorption residuals, accommodating different S/N levels among the experimental spectra. STARKFIT also internally corrects the baselines of the input spectra using a user-defined wavelength range. Once the fit is optimized, a Monte Carlo routine determines the sensitivity of the fit to the value of the fitted Liptay charge redistribution parameters, allowing the uncertainty in the fitted values to be estimated.

Local field correction factors are estimated using the method of Mathies¹³³, which assumes the chromophore solute to be in an ellipsoidal cavity of solvent, which in turn is modelled as a continuous dielectric. The local field correction factor for lumichrome in ethanol was found to be 1.65, for perylene diimide in toluene to be 1.25, and for tetraphenylacetylriboflavin and the tetraphenylacetylriboflavin:dibenzylamidopyridine complex in toluene to be 1.24 and 1.26, respectively.

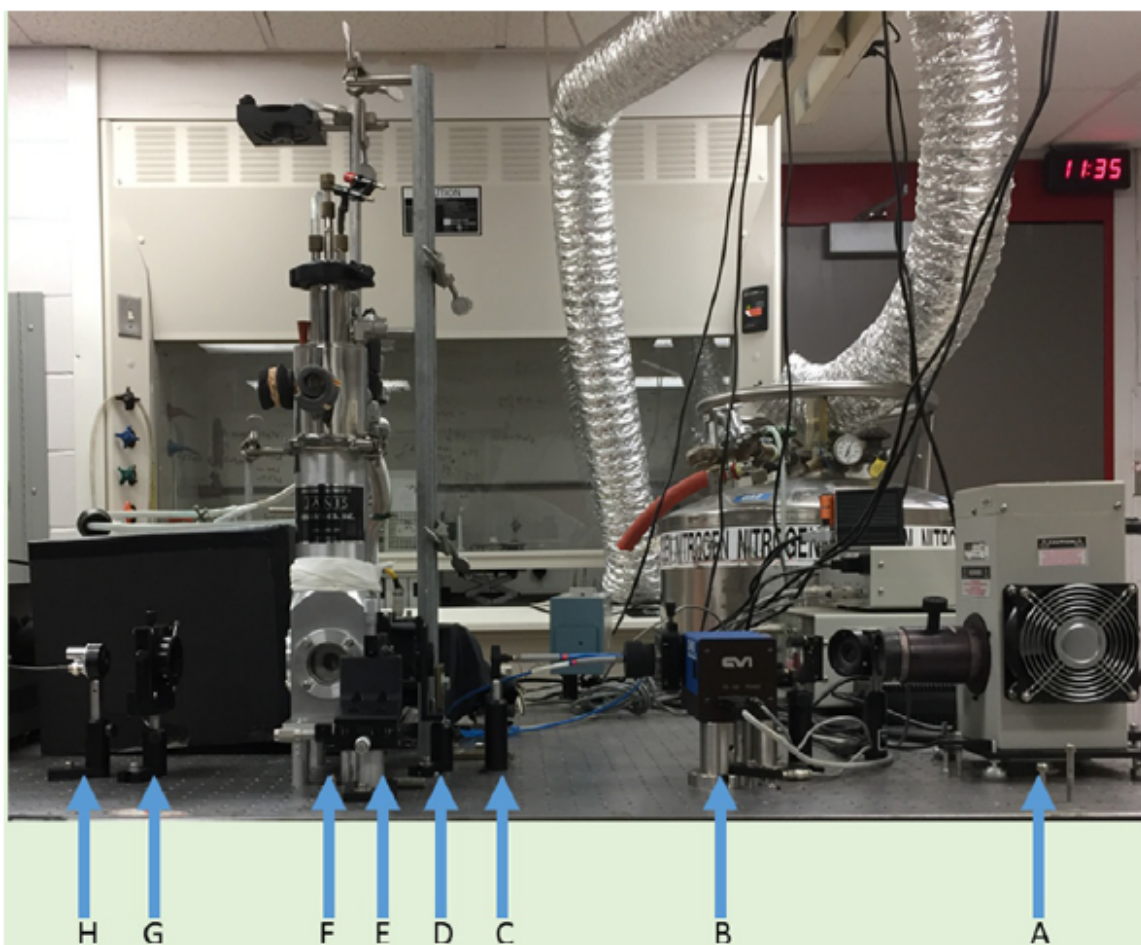


Figure 2.1. An overview of the Stark spectrometer in use in our group. (A) xenon arc lamp and light intensity controller, (B) 1/8-m monochromator, (C) fiber optic outlet, (D) Glan–Taylor polarizer, (E) plano-convex focusing lens, (F) cryostat, (G) double convex focusing lens, and (H) photodiode. The photodiode Faraday cage and current amplifier are not shown in this image.¹³

CHAPTER 3

STARK SPECTROSCOPY OF LUMICHROME: A POSSIBLE CANDIDATE FOR STAND-OFF DETECTION OF BACTERIAL QUORUM SENSING

3.1 Overview

Lumichrome (7,8-dimethylalloxazine, LC) is a natural photodegradation product and catabolite of flavin coenzymes. Although not a coenzyme itself, LC is used for bio-signaling in plants and single-celled organisms, including quorum sensing in the formation of biofilms. The non-invasive detection of in vivo lumichrome would be useful for monitoring this signaling event. For molecules that undergo a large change in charge redistribution upon light excitation (e.g. charge transfer) there are optical detection methods (e.g. second harmonic generation) that would be well suited to this task. Here we have used Stark spectroscopy to measure the extent and direction of charge redistribution in photoexcited LC. Stark and low temperature absorption spectra were obtained at 77 K on LC in ethanol glasses and analyzed using the Liptay analysis to obtain the difference dipole moments and polarizabilities. These data were complemented by a computational analysis of the excited states using DFT at the TD-B3LYP/6-311+G(2d,p) level of theory.

3.2 Sample Preparation and Computational Methods

Lumichrome (99% purity) was obtained from Acros and used without further purification. However, its purity was checked by reverse-phase C18 column chromatography using 1:1 methanol:water, which showed a single peak only (Agilent 126 with diode array detector). All solutions were prepared fresh in anhydrous ethanol (EtOH, Pharmco-Aaper). Extinction coefficients for lumichrome were determined on two

standard solutions made by dissolving ~ 22 (± 0.1) mg LC in 100 mL neat EtOH in a volumetric flask to make a saturated solution. The stoppered solution was sonicated at 65°C for a total of 20 minutes and allowed to cool to room temperature. A 1 mL sample was extracted, filtered using a $0.22\ \mu\text{m}$ poly(vinylidenedifluoride) syringe filter (Fisher), and its absorbance measured. The remaining 99 mL cloudy solution was then filtered under vacuum using a $0.22\ \mu\text{m}$ poly(tetrafluoroethylene) membrane filter (Millipore) that had been pre-weighed. The undissolved LC on the filter was weighed after drying. This mass, along with the absorbance of the 1 mL filtered sample solution gave the room temperature extinction coefficients of the two lowest energy optical transitions of the lumichrome in dry ethanol.

Room-temperature UV-vis spectra were measured in fused silica cuvettes in pathlengths from 0.1-1.0 cm using either a Hewlett-Packard 8453 or 8452A Diode Array Spectrophotometer. Spectra were baseline-corrected using SpectraGryph.¹³⁸ The concentrations of LC/EtOH solutions were determined based on the measured extinction coefficient for LC in EtOH from the standard solutions as described above.

The low-temperature absorption spectrum of LC in EtOH was measured using a cuvette formed from two sapphire windows measuring 1 cm in diameter and 0.52 mm in thickness (Swiss Jewel) separated by a ceramic annulus of thickness $510\ \mu\text{m}$ (Upchurch Scientific). The low temperature spectrum was measured using our in-house constructed Stark spectrometer (see Ch.2). Contraction of the EtOH upon flash-freezing to 77K was $20 \pm 5\%$ based on measuring the change in the height of the solution versus the frozen glass. This contraction leads to an increase in concentration by a factor of 1.25.

All theoretical calculations were completed in the gas phase at the B3LYP/6-311+G(2d,p) level of theory using Gaussian16.¹³⁹ First, the ground state molecular geometry of lumichrome was optimized, and a frequency calculation conducted to verify that the optimized geometry was a minimum of the nuclear potential energy surface. Second, an excited states calculation was completed to determine the transition energies, transition dipole moments, and oscillator strengths of the ten lowest energy electronic excited states of lumichrome. Third, the finite field method was used to determine the difference permanent dipole moments characterizing electronic transitions from the ground state of lumichrome to each of the two lowest energy electronic excited states of lumichrome of experimentally measurable oscillator strength.¹⁴⁰ Briefly, the energy of a molecule in an external electric field, $E(\vec{F})$, may be approximated using a Taylor series truncated at the second term such that $E(\vec{F}) = E(0) - \vec{\mu} \cdot \vec{F}$, where $\vec{\mu}$ is the molecule's permanent dipole moment. Expanding the dot product as $\vec{\mu} \cdot \vec{F} = \mu_x * F_x + \mu_y * F_y + \mu_z * F_z$, and assuming that molecular energy depends linearly on field magnitude for field magnitudes on the order of 0.001 a.u. (5.142 MV/cm), the component $\vec{\mu}_i$ of the permanent dipole moment may be computed as

$$\vec{\mu}_i = - \left(\frac{E(\vec{F}_i = +0.001 \text{ a.u.}) - E(\vec{F}_i = -0.001 \text{ a.u.})}{0.002 \text{ a.u.}} \right) \quad (3.1)$$

Gaussian16 permits single point calculations and excited states calculations to be completed with finite electric fields projected in the positive or negative direction along each of the three Cartesian axes. By cycling through each of the six possible finite field components one at a time and computing molecular energies for the electronic ground

state and each of the relevant electronic excited states in the presence of each finite field, it is possible to determine the components of the permanent dipole moments of each electronic state, and also therefore the components of the difference permanent dipole moment characterizing each relevant electronic transition. Having calculated the difference dipole moment and the transition dipole moment characterizing each transition, it was possible to compute the angle between the difference dipole moment and transition dipole moment, ζ_A . Difference electron densities were computed using Gaussian16, and visualized using GaussView 6.0.16.¹⁴¹ All calculations conducted for lumichrome were repeated for lumiflavin.

3.3 Results

Room temperature and low-temperature absorption spectra were obtained as described above. The 298K spectrum (Figure 3.1) shows two near-UV broad bands centered at 338 nm and 385 nm. Based on a replicate pair of measurements, these bands have peak extinction coefficients of $\epsilon_{385\text{nm}} = 9100 \pm 100 \text{ M}^{-1} \text{ cm}^{-1}$ and $\epsilon_{338\text{nm}} = 9500 \pm 100 \text{ M}^{-1} \text{ cm}^{-1}$.

There are a variety of measurements for the extinction coefficient of LC in ethanol, varying from about $4,600 \text{ M}^{-1} \text{ cm}^{-1}$ to $50,000 \text{ M}^{-1} \text{ cm}^{-1}$.^{54, 142-144} The room temperature absorption spectrum of lumichrome in dry ethanol was acquired at a range of different lumichrome concentrations up to $\sim 1 \text{ mM}$, but no evidence of dimerization was observed (data not shown).

Three separate 77K absorption spectra of LC in anhydrous ethanol were averaged (Figure 3.1). At 77K, the 385 nm band shifts by +2 nm to 387 nm, and becomes more

structured, with apparent vibronic structure at 369 and 405 nm. The extinction falls to $\epsilon_{387\text{nm}} = 8500 \pm 100 \text{ M}^{-1} \text{ cm}^{-1}$. The band centered at 338 nm narrows and shifts +6 nm to 344 nm, with a decreased extinction coefficient of $\epsilon_{344\text{nm}} = 8000 \pm 100 \text{ M}^{-1} \text{ cm}^{-1}$.

High signal/noise ratio Stark spectra were obtained at $\chi=55^\circ$ and 90° (Figure 3.2). The electrochromism of the Stark spectra (change in $\Delta\epsilon$ vs. χ) were examined to determine the minimum number of electronic transitions spanning the wavelength region of interest (~321-476 nm). The differing electrochromism at approximately 340 nm and 380 nm strongly suggests that two electronic transitions span this range.

To verify that two electronic transitions are present, an initial absorption spectrum fit using one set of gaussians (a single transition) was performed for LC where the number of gaussians was varied from 3 to 8. The fits were poor (fits not shown), verifying that at least two electronic transitions form the optical absorption spectrum of LC in dry ethanol.

Fits using two and three electronic transitions were then performed. Since no improvement was obtained in going from two to three transitions, the absorption/Stark spectra were fitted under the assumption that lumichrome in dry ethanol undergoes two distinct electronic transitions ($S_0 \rightarrow S_1$ and $S_0 \rightarrow S_2$) in the spectral range from 312 nm to 476 nm.

The best fit, with the minimal, random residuals, to both the Stark and absorption spectrum for LC in anhydrous ethanol came from the two-transition fit with 14 total gaussians (7 per transition). From this fit (Figure 3.2), we determined the values of the Stark charge redistribution parameters based on the $A\chi$, $B\chi$, and $C\chi$ coefficients

characterizing the electrochromism of LC's two optical transitions. These parameters are compiled in Table 3.1. All values have been corrected for the local field correction factor, f_C , which has a value of 1.65 for LC in ethanol.

The properties of the first ten singlet electronic excited states S_1 - S_{10} of LC and LF were computed and compared to the ground (S_0) states. Based on the generated electron difference density maps (Figure 3.3), all of the transitions have $\pi - \pi^*$ character. The theoretical transition energy, the oscillator strength, f_{osc} , magnitudes of the transition and difference permanent dipole moments, \vec{m}_{fi} and $\Delta\vec{\mu}_{fi}$, as well as the angle between these vectors, ζ_A , are tabulated in Table 3.2 for the two lowest-energy bright electronic transitions of LC and LF. The three lowest energy singlet-singlet transitions are within the spectral scan range (312-476 nm), and have non-negligible oscillator strengths. Based on f_{osc} , the bright (observed) transitions should be assigned as S_{10} and S_{30} . However, if the S_{20} state has significant charge-transfer (CT) character it may appear in the Stark spectra as well as a large difference mean polarizability, $\text{Tr}\Delta\vec{\alpha}_{fi}$. No evidence of this is found. The mean polarizability change for the two observed transitions is modest, and therefore the TD-DFT results suggest that the experimental data is best modeled using $|\Delta\vec{\mu}_{n0}|$ (the second derivative of the absorption spectrum), and that the assignment as S_{10} and S_{30} is correct.

Charge redistribution (excitation difference density) maps and difference dipole vector diagrams are shown in Figure 3.3. The computed transition dipole moment vectors of LC and LF in EtOH are given as dotted arrows. Computed difference permanent dipole moment vectors of LC and LF are given as solid, colored arrows, while the

experimental difference permanent dipole moment vectors of LC are given as black arrows.

As shown in the ρ -CI difference density ($\Delta\rho = \rho_n - \rho_0$) map for LC, the S_{10} transition involves a relatively even redistribution of charge with $|\Delta\vec{\mu}_{10}| = 1.88$ D, confirming the low experimental $|\Delta\vec{\mu}_{10}| = 0.97$ D, as well as a small change in difference polarizability, $\text{Tr}\Delta\vec{\alpha}_{10}$. It can be seen that the S_{10} transition in lumiflavin involves greater concentration of $\Delta\rho$ in the conjugated diazarene group (N5-C4a-C10a-N1). On the contrary, the S_{30} transition shows transfer of charge to the pyrimidine ring from the pyrazine/xylene rings. This redistribution justifies qualitatively the change in direction and increased magnitude of the $\Delta\vec{\mu}_{30} = 5.37$ D, compared to that for LF, $\Delta\vec{\mu}_{20} = 4.32$ D.

3.4 Discussion

The probability of second-harmonic generation by an oriented ensemble of chromophores, such as those transiting a cell membrane,^{145, 146} is directly proportional to the second-harmonic generation cross-section characteristic of each chromophore, σ_{SHG} , which is itself proportional to the squared magnitude of the first optical molecular hyperpolarizability,¹⁴⁷⁻¹⁵⁰ β . Within the two-level approximation, the hyperpolarizability is^{151, 152}

$$\beta = \frac{3e^2}{2\hbar^3} \frac{\omega_{n0} f_{n0} |\Delta\vec{\mu}_{n0}|}{(\omega_{n0}^2 - \omega^2)(\omega_{n0}^2 - 4\omega^2)} \quad (3.2)$$

where e is the elementary unit of charge, \hbar is the reduced Planck's constant, ω_{n0} is the frequency of light exciting the chromophore from the ground state to the n^{th} excited state, f_{n0} is the oscillator strength of the transition, and $|\Delta\vec{\mu}_{n0}|$ is the magnitude of the

chromophore's change in permanent dipole moment upon excitation. The parameter ω is equal to the frequency of the incident light.

The product, $\omega_{n0}f_{n0}|\Delta\vec{\mu}_{n0}|$, in the numerator of this equation quantifies the molecular determinants of the hyperpolarizability and thus the probability of SHG, while the product $(\omega_{n0}^2 - \omega^2)(\omega_{n0}^2 - 4\omega^2)$ in the denominator quantifies the potential for resonance enhancement of second-harmonic generation as a function of the frequency of the incident light. If we assume that separate light sources are available for maximizing the resonance enhancement of two specific transitions of two different molecules, then the relative resonance-enhanced second-harmonic generation cross-sections of the two molecules are a function of only each chromophore's excitation frequency, oscillator strength, and difference dipole moment, such that

$$\frac{\sigma_{SHG_i}}{\sigma_{SHG_j}} = \frac{|\beta_i|^2}{|\beta_j|^2} \cong \frac{|\omega_{n0}f_{n0}|\Delta\vec{\mu}_{n0}|_i|^2}{|\omega_{n0}f_{n0}|\Delta\vec{\mu}_{n0}|_j|^2} = \frac{\left| \left(\omega_{n0} \cdot \int_{band} \frac{\varepsilon(\bar{\nu})}{\bar{\nu}} \cdot |\Delta\vec{\mu}_{n0}| \right)_i \right|^2}{\left| \left(\omega_{n0} \cdot \int_{band} \frac{\varepsilon(\bar{\nu})}{\bar{\nu}} \cdot |\Delta\vec{\mu}_{n0}| \right)_j \right|^2} \quad (3.3)$$

where the oscillator strength f_{n0} has been substituted by the energy-weighted integrated extinction of the transition, $\int_{band} \frac{\varepsilon(\bar{\nu})}{\bar{\nu}}$, to which it is directly proportional.¹⁵³

Second-harmonic generation by flavin derivatives designed to maximize intramolecular charge transfer via push-pull motifs has been studied by our group¹⁵ and others.^{154, 155} Second-harmonic generation by native flavins, however, has been less studied. To our knowledge, the only publication of second-harmonic generation by a native flavin is that of Rinuy, Brevet, and Girault,¹⁵⁶ who measured resonance-enhanced second harmonic generation by the first optical transition of molecules of oxidized flavin

adenine dinucleotide bound by glucose oxidase oriented at an air/water interface. While no Stark spectroscopic study of glucose oxidase has been completed to directly compare LC's potential for second-harmonic generation to that of FAD bound by glucose oxidase in terms of intramolecular charge redistribution, we have published a Stark spectroscopic study of oxidized FAD bound by photolyase.¹⁷ The cofactor binding pockets of glucose oxidase and photolyase differ structurally, but to a first approximation both are predominantly hydrophobic protein environments excluding solvent.

The first optically bright transition of oxidized FAD in photolyase is characterized by an excitation frequency of 674.49 THz (corresponding to a λ_{max} of 444.48 nm), an integrated energy-weighted extinction of 1747.37 M⁻¹cm⁻¹, and a difference dipole moment of 1.7 D. Since the first optically bright transition of LC has a smaller difference dipole moment of ~1 D, we choose to exploit the next optically bright transition, n=0→3, in the TD-DFT result, for comparison to FAD, using the work on two-photon cross sections in higher excited states of trans-stilbene as a guide.¹⁵⁷ The S₃₀ transition of LC in ethanol is characterized by an excitation frequency of 889.98 THz (corresponding to a λ_{max} of 336.98 nm), an integrated energy-weighted extinction of 919.17 M⁻¹cm⁻¹, and a difference dipole moment of 2.2 D.

Assuming resonant illumination of each transition at appropriate energies, these molecular parameters indicate that the relative resonance-enhanced second-harmonic generation cross sections of these transitions of these chromophores to be

$$\begin{aligned}
\frac{\sigma_{SHG_{LC}}}{\sigma_{SHG_{FAD}}} &= \frac{|\beta_{LC}|^2}{|\beta_{FAD}|^2} = \frac{\left| \left(\omega_{n0} \cdot \int_{band} \frac{\epsilon(\bar{\nu})}{\bar{\nu}} \cdot |\Delta\vec{\mu}_{n0}| \right)_i \right|^2}{\left| \left(\omega_{n0} \cdot \int_{band} \frac{\epsilon(\bar{\nu})}{\bar{\nu}} \cdot |\Delta\vec{\mu}_{n0}| \right)_j \right|^2} \\
&= \frac{|889.98 \text{ THz} \cdot 919.17 \text{ M}^{-1} \text{ cm}^{-1} \cdot 2.2 \text{ D}|^2}{|674.49 \text{ THz} \cdot 1747.37 \text{ M}^{-1} \text{ cm}^{-1} \cdot 1.7 \text{ D}|^2} = 0.81 \quad (3.4)
\end{aligned}$$

The S₁₀ transition of oxidized FAD bound in a protein environment is characterized by a lower energy and slightly smaller difference dipole moment than the S₃₀ transition of LC, but also by a significantly greater energy-weighted integrated extinction, giving LC a second-harmonic generation cross section that is approximately 80% that of FAD. Because the first optically bright transition of FAD bound within a protein environment has previously been demonstrated to be robustly capable of resonance-enhanced second-harmonic generation, and the resonance-enhanced second-harmonic-generation cross section of LC is just 20% less than that of FAD's first transition, we conclude that LC should function as an experimentally viable intramembrane second-harmonic generation probe.

Here, we have presented the room-temperature absorption, low-temperature absorption, and Stark spectra for lumichrome in dry ethanol. Since flavin has a useful SHG cross section, we hypothesized that LC might also be a useful nonlinear spectroscopic probe of bacterial quorum sensing, an indicator of retinal health, or in any situation where LC is used as a signaling molecule through an interface as well. Since RBF and FMN must pass through membranes, we speculated that LC, in particular, would also be a good SHG probe of riboflavin/FMN uptake, transport, and photodegradation. Excitation of LC can be accomplished using Ti:sapphire oscillators

from 750 to 840 nm, a range at which light still has a large tissue penetration depth. A further advantage of LC for SHG stand-off detection is its intrinsically small emission quantum yield. FMN and RBF exhibit emission maxima at approximately 530 nm, with a fluorescence quantum yield of 0.25, while LC exhibits an emission maximum at 480 nm, with a fluorescence quantum yield of 0.04.²⁶ However, for SHG detection, fluorescence is an interfering background component, so the lower fluorescence quantum yield of LC results in an approximately six-times reduction of this background.

To conclude, LC is collected and secreted from the cell as a waste product from photodegradation and catabolism of cellular flavins, so that it is not surprising that it is found to act as a biochemical signal for quorum sensing.⁵² An interesting opportunity exists for LC imaging at interfaces by SHG, since it is used in quorum sensing and thus must be transported through the cell membrane, the secretion process will involve LC oriented at interfaces where it may be a useful indicator of metabolic stress and biofilm formation. A final determination of its usefulness as a SHG probe in these cases awaits dedicated experimentation.

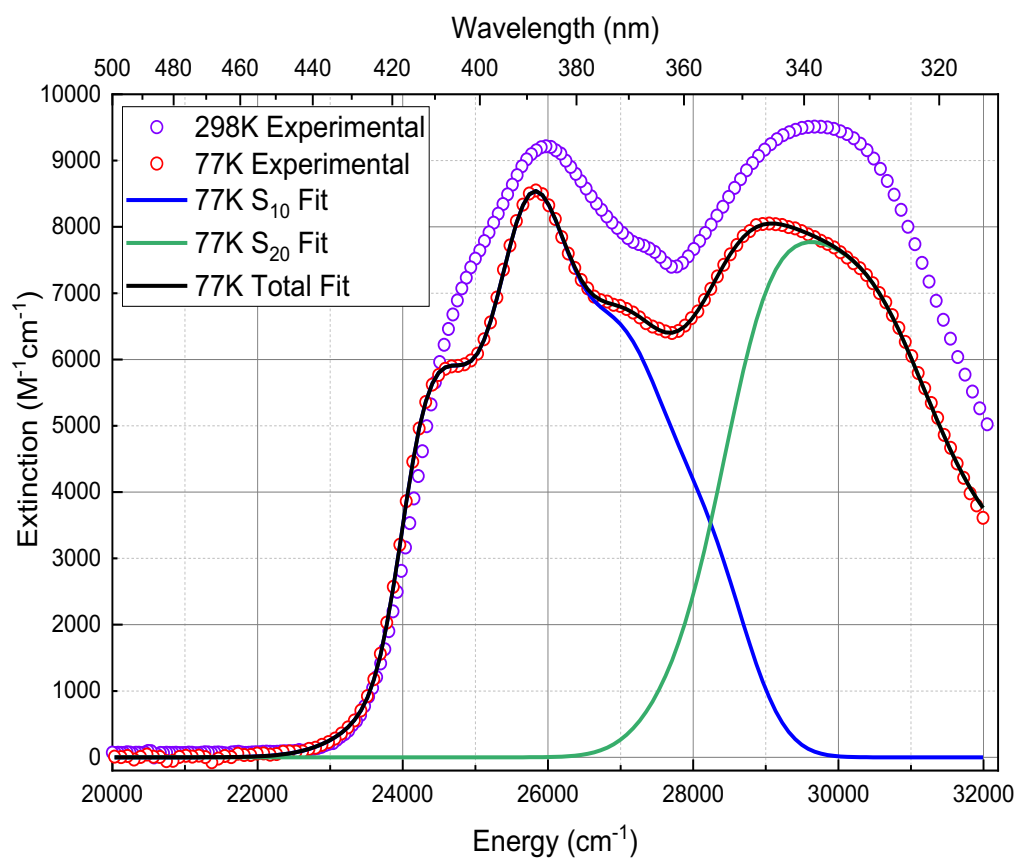


Figure 3.1. 298 K and 77 K absorption spectra of lumichrome in dry ethanol. Also shown are transition-specific (blue/green lines) and total fit (black line) to the low-temperature absorption spectrum (red circles).

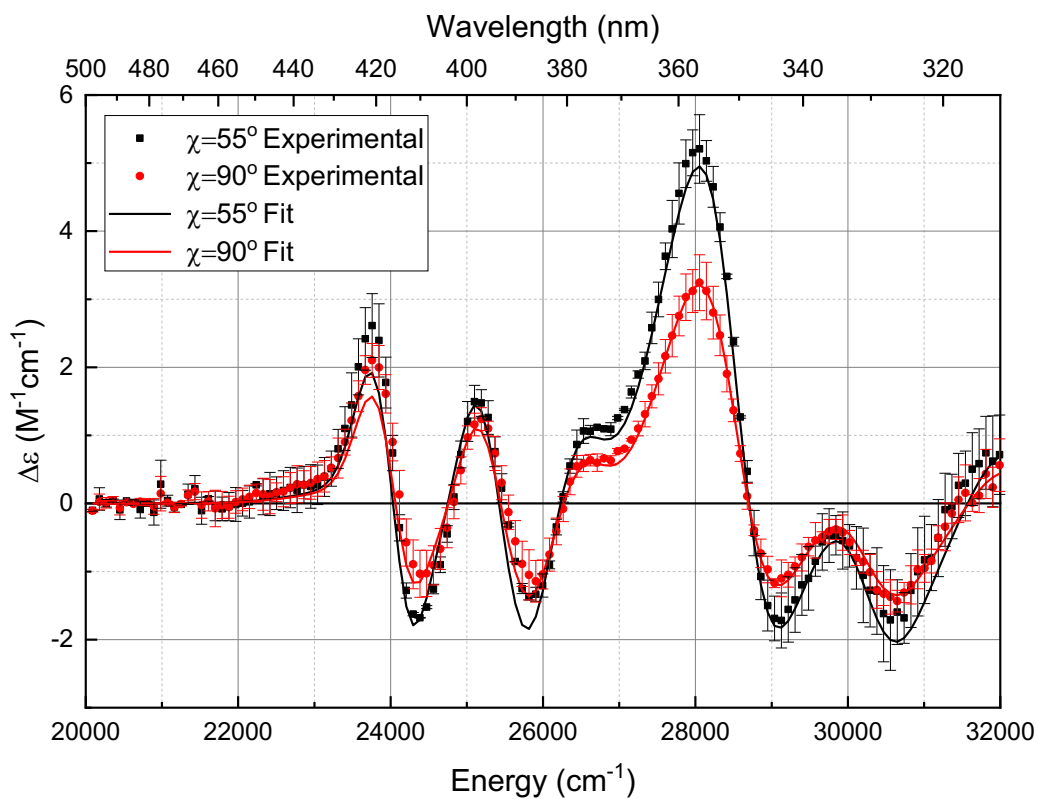


Figure 3.2. Lumichrome Stark spectra at two χ angles. Spectra are normalized to an applied external field of 1 MV/cm. The $\chi = 55^\circ$ results are an average of two spectra averaged over 10 scans each, and the $\chi = 90^\circ$ results are an average of three such spectra. Representative error bars are one standard deviation from the mean.

Table 3.1. Fit charge redistribution parameters for lumichrome in dry ethanol at 77 K.

Transition**	λ_{max} (nm)	ϵ_{max} ($M^{-1}cm^{-1}$)	$Tr\Delta\bar{\alpha}_{fi}$ (\AA^3)	$\bar{m}_{fi} \cdot \Delta\bar{\alpha}_{fi} \cdot \bar{m}_{fi}$ (\AA^3)	$ \Delta\bar{\mu}_{fi} $ (D)	ζ_A ($^\circ$)
S ₁₀	387 ± 2	8541 ± 100	5.9 ± 0.6	1.1 ± 0.6	0.97 ± 0.03	30 ± 11
S ₃₀	344 ± 2	8000 ± 100	38 ± 3	28 ± 4	2.2 ± 0.1	23 ± 9

*The local field correction factor, f_C for lumichrome in ethanol is 1.65.

** From DFT calculations.

Table 3.2. DFT results for gas phase lumichrome and lumiflavin. In this table the designations of the electronic transitions correspond to the optically-bright, experimentally-measurable transitions as determined by the TD-DFT calculations.

Compound	Transition	λ (nm)	f	$ \Delta\mu_{n0} $ (D)	ζ_A ($^\circ$)
Lumichrome	S ₁₀	367.00	0.0649	1.8840	21.05
	S ₃₀	321.84	0.2235	5.3658	17.21
Lumiflavin	S ₁₀	412.92	0.1993	1.7674	65.33
	S ₄₀	325.27	0.1464	4.3219	11.55

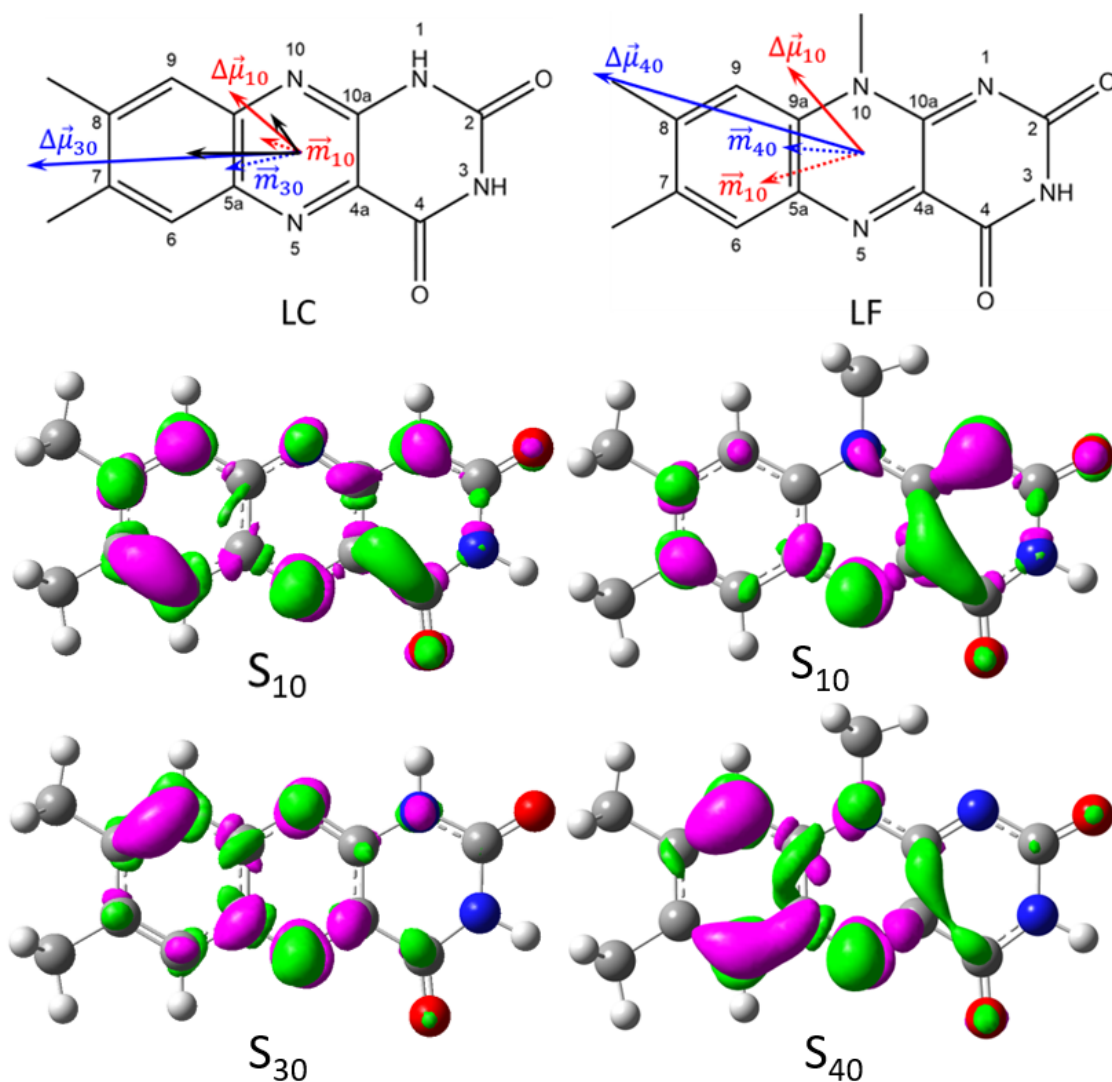


Figure 3.3. Vector diagrams and difference density maps for lumichrome and lumiflavin. Top: Calculated difference dipole moment vector diagrams for gas phase lumichrome and lumiflavin calculated at the B3LYP/6-311+G(2d,p) level of theory using Gaussian16W and visualized using GaussView 6.0.16. Bottom: Difference density maps of LC and LF. The isovalue used is $0.0025 \text{ e}^-/\text{au}^3$. Green represents a region gaining electron density upon excitation, while purple represents a region becoming more electropositive upon excitation.

Table 3.3. Molecular geometry of lumichrome optimized in the gas phase.

Optimization completed at the B3LYP/6-311+G(2d,p) level of theory using Gaussian16. A frequency calculation was conducted to verify that the optimized geometry is a minimum on the nuclear geometry potential energy surface. Coordinates are in angstroms.

Atom	X	Y	Z
C	3.908134	2.988834	0.000000
C	2.547934	2.345093	0.000000
C	1.366475	3.162481	0.000000
C	0.133851	2.560858	0.000000
C	0.000000	1.152087	0.000000
C	1.175041	0.340892	0.000000
C	2.435675	0.974576	0.000000
H	3.317287	0.344753	0.000000
N	1.088214	-1.011596	0.000000
C	-0.120409	-1.520622	0.000000
N	-0.245437	-2.897479	0.000000
C	-1.440517	-3.585008	0.000000
N	-2.567694	-2.770965	0.000000
C	-2.636550	-1.376029	0.000000
C	-1.299000	-0.716646	0.000000
N	-1.228572	0.592992	0.000000
O	-3.699264	-0.802759	0.000000
H	-3.451816	-3.263606	0.000000
O	-1.508489	-4.794555	0.000000
H	0.597983	-3.454754	0.000000
H	-0.777180	3.147367	0.000000
C	1.481644	4.664027	0.000000
H	2.024281	5.025421	0.878275
H	0.496142	5.129128	0.000000
H	2.024281	5.025421	-0.878275
H	4.047148	3.626584	-0.877668
H	4.697515	2.237690	0.000000
H	4.047148	3.626584	0.877668

Table 3.4. Molecular geometry of lumiflavin optimized in the gas phase.

Optimization completed at the B3LYP/6-311+G(2d,p) level of theory using Gaussian16. A frequency calculation was conducted to verify that the optimized geometry is a minimum on the nuclear geometry potential energy surface. Coordinates are in angstroms.

Atom	X	Y	Z
C	-0.039452	0.000000	0.004482
C	2.070364	-0.000148	-1.916940
C	4.650650	-0.000178	-1.143382
C	5.320818	-0.000083	1.627970
H	4.543741	1.663658	2.592499
H	4.543930	-1.663882	2.592558
H	7.368622	0.000034	1.910397
C	6.577083	-0.000304	-2.941022
C	6.033327	-0.000413	-5.541686
C	3.466394	-0.000379	-6.322184
C	1.539611	-0.000249	-4.480369
H	-0.395867	-0.000231	-5.164934
N	2.798667	-0.000458	-8.820730
C	4.583776	-0.000594	-10.506800
C	7.287552	-0.000652	-9.925361
N	7.902593	-0.000533	-7.382632
C	10.577272	-0.000528	-6.639793
H	10.993135	-1.690684	-5.523249
H	10.993152	1.689686	-5.523345
H	11.708303	-0.000589	-8.355484
N	9.106723	-0.000722	-11.599637
C	8.523321	-0.000693	-14.143567
N	5.938596	-0.000584	-14.833383
C	3.864879	-0.000914	-13.248821
O	1.696205	-0.000364	-14.027161
H	5.583823	-0.000450	-16.719859
O	10.117677	-0.000711	-15.810672
H	8.520417	-0.000321	-2.294477
H	0.045121	1.666263	1.237181
H	-1.884347	-0.000144	-0.927904
H	0.045206	-1.665991	1.237539

Table 3.5. First ten excited states of gas phase lumichrome. Excited states calculated at the B3LYP/6-311+G(2d,p) level of theory using Gaussian16.

Excited State	Wavelength (nm)	Oscillator Strength
1	367.00	0.0649
2	362.79	0.0011
3	321.84	0.2235
4	311.12	0.0001
5	258.57	0.0290
6	254.38	0.0000
7	250.81	0.0000
8	248.89	0.2674
9	243.26	0.0000
10	240.99	0.2555

Table 3.6. First ten excited states of gas phase lumiflavin. Excited states calculated at the B3LYP/6-311+G(2d,p) level of theory using Gaussian16.

Excited State	Wavelength (nm)	Oscillator Strength
1	412.92	0.1993
2	391.09	0.0003
3	373.81	0.0003
4	325.27	0.1464
5	315.72	0.0000
6	306.18	0.0110
7	268.28	0.0002
8	264.81	0.0936
9	256.45	0.5767
10	249.32	0.0329

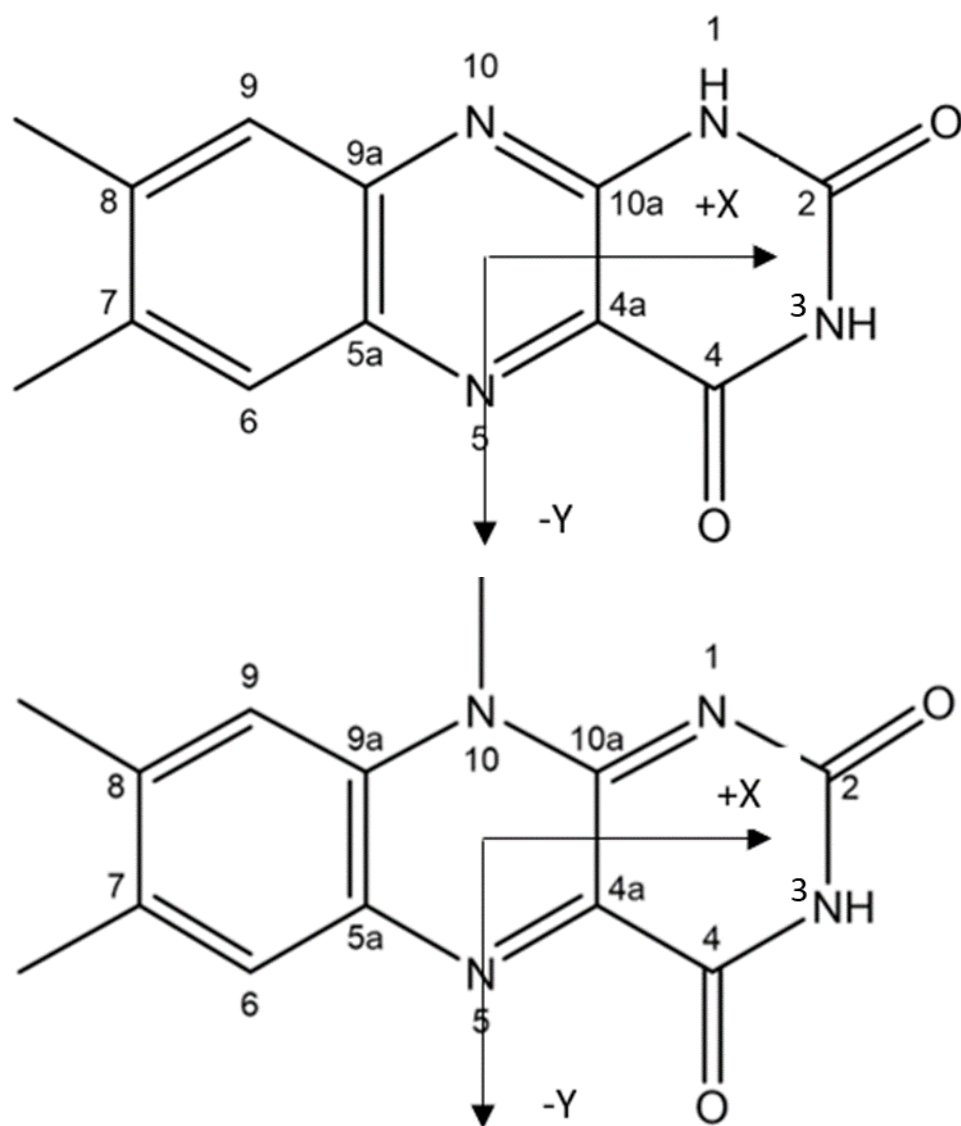


Figure 3.4. Standard orientations of lumichrome and lumiflavin.

Table 3.7. Vector components of theoretical transition and difference dipole moments. Transition dipole moments (\vec{m}) and difference permanent dipole moments ($\Delta\vec{\mu}$) of the two lowest experimentally-measurable electronic transitions of gas phase Lumichrome and Lumiflavin calculated at the B3LYP/6-311+G(2d,p) level of theory using Gaussian16. Vector components are given in the above standard orientation. The finite field method was used to compute the difference permanent dipole moments. Coordinates are in units of Debye.

Compound	Transition	Vector	X	Y	Z
LC	S ₁₀	\vec{m}	-0.83	0.29	0.00
		$\Delta\vec{\mu}$	-1.43	1.22	0.00
	S ₃₀	\vec{m}	-1.44	-0.53	0.00
		$\Delta\vec{\mu}$	-5.36	-0.26	0.00
LF	S ₁₀	\vec{m}	-1.58	-0.47	0.00
		$\Delta\vec{\mu}$	-1.17	1.33	0.00
	S ₄₀	\vec{m}	-1.25	0.10	0.00
		$\Delta\vec{\mu}$	-4.15	1.22	0.00

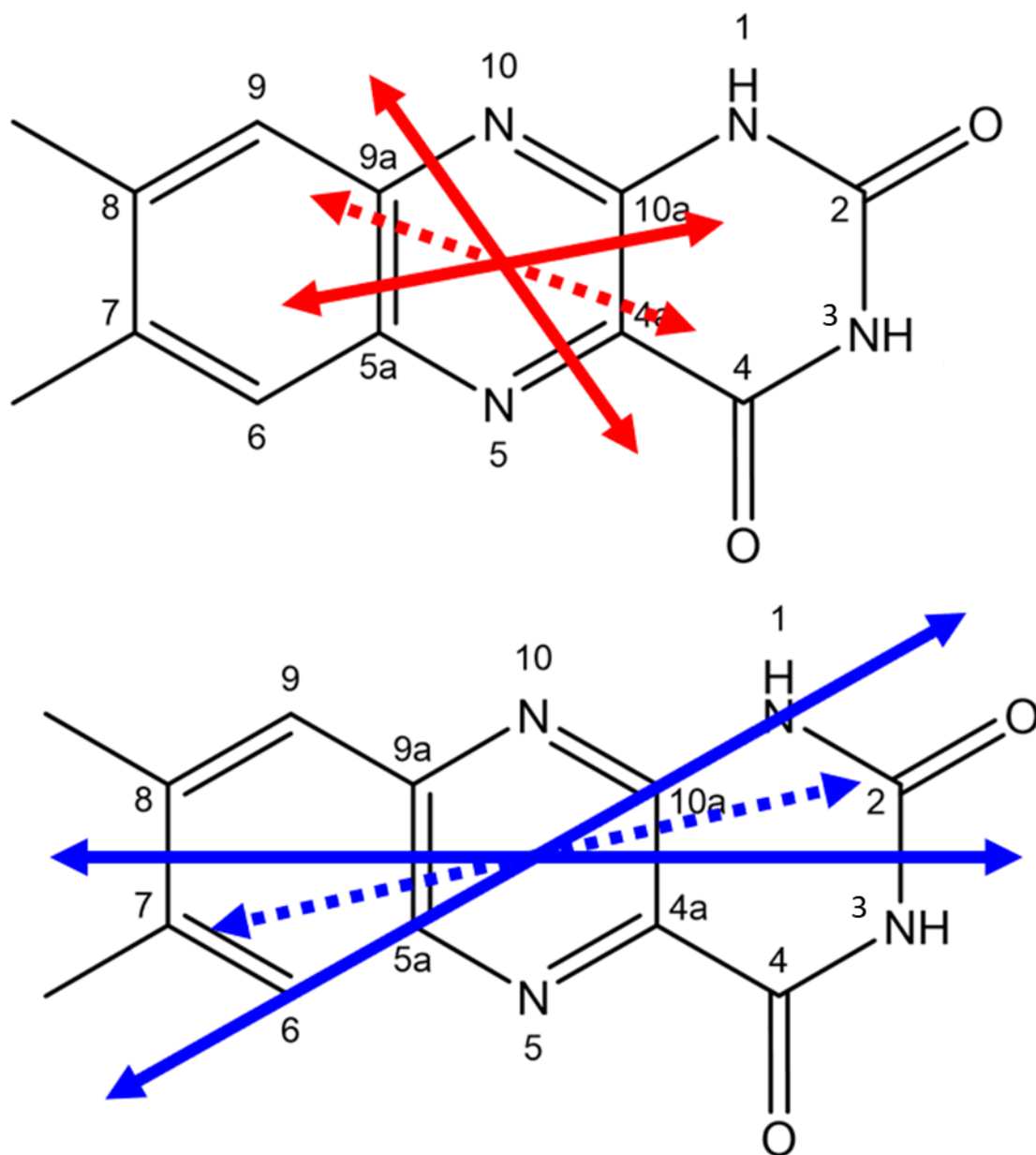


Figure 3.5. Possible molecular orientations of experimental difference dipole moments. The S_{10} difference permanent dipole moment of the lumichrome is given in red, and the S_{30} difference permanent dipole moment of the lumichrome is given in blue, relative to the theoretically determined transition dipole moments. In these figures, the solid lines represent the difference permanent dipole moment possibilities and the dotted line represent the transition dipole moment possibilities.

CHAPTER 4

OPTICAL BAND GAP TUNING OF MONOMERIC PERYLENE DIIMIDE

4.1 Overview

Perylene diimide (PDI) and its derivatives are essential components of organic molecular electronics revolutionizing solar technology and the digital world. These compounds' wide applicability is due to the range of useful photophysical attributes that emerge as monomers aggregate to form higher order structures. In order to better understand how aggregation builds on monomer photophysics in specific, technologically useful ways, we have utilized Stark spectroscopy to measure charge redistribution through the molecular structure of monomeric PDI upon optical excitation. Excitation from the ground to first excited state increases the molecular polarizability by 42 \AA^3 , predominantly along the molecule's long axis. These data are complemented by a TD-DFT study of the chromophore's first excited state.

4.2 Sample Preparation and Computational Methods

N,N'-Bis(2,6-diisopropylphenyl)-3,4,9,10-perylenetetracarboxylic diimide was purchased from TCI America and used without further purification. Experimental solutions were prepared by dissolving PO in anhydrous toluene to a final concentration of $958 \text{ }\mu\text{M}$. Room temperature UV/vis spectra were recorded using an HP8453 Diode Array Spectrophotometer and a 2.0 mm path length quartz cuvette (Spectrocell).

Regarding computational methods, the molecular geometry of Perylene Orange implicitly solvated¹⁵⁸ in toluene was optimized at the B3LYP/6-31+G(d)/PCM level of theory using Gaussian16.¹³⁹ A frequency calculation was completed at the same level of

theory to verify convergence of the geometry optimization, and an excited states calculation was performed to compute the ten lowest energy excited states of the system. The SCF and CI densities were computed for the ground and first excited states, respectively, and the difference density was visualized using GaussView6.1.¹⁵⁹ The finite field method was used to determine the change in polarizability upon excitation from the ground to first excited state.¹⁶⁰

4.3 Results

The 298K absorption spectrum of PO in toluene (Figure 4.1) shows distinct vibronic structure, with four resolved vibronic bands between 16000 cm^{-1} and 25000 cm^{-1} . The maximum extinction of PO in toluene at 298K is 71500 $\text{M}^{-1}\text{cm}^{-1}$, occurring at an energy of 19011 cm^{-1} .⁹⁶ This is presumed to be the 0_0^0 transition. From this lowest-energy band, a second band is centered at 20048 cm^{-1} , a difference in energy of 1037 cm^{-1} from the 0_0^0 transition, and with an extinction of 51600 $\text{M}^{-1}\text{cm}^{-1}$. The next higher energy band is centered at 21739 cm^{-1} , a difference in energy of 1691 cm^{-1} from the second band, with an extinction of 18794 $\text{M}^{-1}\text{cm}^{-1}$. The fourth band is centered at 23148 cm^{-1} , a difference in energy of 1409 cm^{-1} from band three, and with an extinction of 5085 $\text{M}^{-1}\text{cm}^{-1}$. The spacing between bands of the vibronic structure is not constant because multiple vibronic progressions characterized by different Huang-Rhys parameters and similar vibrational quanta sum to give these four bands.⁹⁶

The 77K absorption spectrum of PO in toluene differs considerably from the absorption at 298K. As a result of the increased spectral resolution afforded at 77K, the lowest energy band is split into two components. The 0_0^0 band shifts slightly to lower

energy by 457 cm^{-1} to 18554 cm^{-1} , narrows at half maximum height by approximately 50% and increases in extinction to $74000 \text{ M}^{-1} \text{ cm}^{-1}$. A vibronic band appears as a shoulder at 19065 cm^{-1} , a difference in energy of 511 cm^{-1} , with an extinction of $15735 \text{ M}^{-1} \text{ cm}^{-1}$. The second and third bands present in the 298K spectrum shift to lower energies and to significantly lower extinctions, evidence of a temperature-dependent change in the Huang-Rhys factors contributing to these bands. The fourth band present in the 298K spectrum differs only marginally in extinction from its 77K counterpart, but at the colder temperature shift lower in energy by 228 cm^{-1} to 22866 cm^{-1} . Interestingly, the extinction at 77K begins to increase again from 23500 cm^{-1} , indicating possible partial overlap at 77K between the S_{10} and S_{20} absorption bands.

High signal-to-noise Stark spectra were recorded at $\chi = 55^\circ$ and 90° (Figure 4.2). To avoid contamination of the fitted S_{10} charge redistribution parameters with a contribution from the S_{20} transition beginning at the blue edge of the recorded Stark and 77K absorption spectra, the fit of the Stark spectra was truncated to between 16000 cm^{-1} and 22000 cm^{-1} . The number of Gaussians used to fit the 77K extinction spectrum was increased from four to nine, at which point the residuals of the fit of the sum of the Gaussians to the 77K extinction were minimized and random. The presence of a single electronic transition in this region agrees with prior theoretical analysis,⁹⁷ as well as our own. The best fit to the Stark spectra yielded a difference permanent dipole moment, $|\Delta\vec{\mu}_{10}|$, of 0.00 D, a trace difference polarizability, $Tr\Delta\vec{\alpha}_{10}$, of $42 \pm 1 \text{ \AA}^3$, and a component of the difference polarizability along the transition dipole moment, $\vec{m}_{10} \cdot$

$\Delta\bar{\alpha}_{10} \cdot \vec{m}_{10}$, of $29 \pm 1 \text{ \AA}^3$. These values have been corrected for the local field factor,^{161,}
¹⁶² f_c , which, for PO in toluene, has a value of 1.25.

4.4 Discussion

The negligible difference permanent dipole moment of PO results from the molecule's approximate centrosymmetry. PO occupies the D_{2h} point group when the PDI core of the molecule is planar and the diisopropylphenyl groups are perpendicular to the PDI core. This conformation is, however, strained relative to a lower energy skew-planar conformation that is preferentially populated at room temperature.¹⁶³ Our DFT optimization of PO in toluene concurs with previous theoretical studies^{96, 97} in demonstrating that the diisopropylphenyl substituents of PO are not perpendicular to the PDI plane, and that the plane itself is slightly warped. In the structure of PO implicitly solvated in toluene optimized at the B3LYP/6-31+G(d)/PCM level of theory, the plane of one diisopropylphenyl substituent is 0.062° off-orthogonal to the PDI plane, and the plane of the second one diisopropylphenyl substituent is 0.670° off-orthogonal to the PDI plane, in the opposite direction. The dihedral angle between the two pairs of oxygen atoms of each imide moiety was calculated to be 3.619° . Together, rotation of the diisopropylphenyl substituents and skewing of the PDI plane shift PO to the C_1 point group and reduce strain by 9.0 cm^{-1} , which is $(0.17)k_B T$ at 77K, leading to a nearly 1:1 distribution between the two states at this temperature. Because both the D_{2h} planar and C_1 skew-planar conformational isomers are characterized by theoretical permanent dipole moments of less than 0.00 D in both the ground and first singlet excited states, interconversion between the two states does not alter the measured $|\Delta\vec{\mu}_{10}|$ of the

ensemble. Figure 4.3 shows the change in electron density ($\rho_{CI} - \rho_{SCF}$) upon vertical excitation of skew-planar PO from the ground to first singlet excited state, with green representing regions gaining electron density and purple representing regions becoming more electropositive. The redistribution of electron density is confined to the PDI core of PO, demonstrating that the diisopropylphenyl groups do not contribute to the excitation, and is radially symmetric about the center of mass. Beginning with a loss of electron density from the center of the perylene ring system, regions extending from the center of mass to the imide carbonyls alternately gain and lose electron density, ending with the carbonyl, which predominantly gains electron density. If the PDI core of PO were to adopt an umbrella conformation, with the four imide carbonyl oxygens extending out of the central plane in the same direction, then PO could possess a non-zero difference permanent dipole moment. However, because two carbonyl oxygens are skewed above the plane and two are skewed below the plane, the out of plane components of the change in electron density cancel. Figure 4.3 also shows the theoretical transition dipole moment of the PO S₁₀ transition, which is directed along the long axis of the molecule.

The fitted value of the trace of the difference polarizability tensor for the S₁₀ transition of PO in toluene, when corrected for local field enhancement, gives $Tr\Delta\bar{\alpha}_{10} = 42 \pm 1 \text{ \AA}^3$, with the component of the total polarizability parallel to the S₁₀ transition dipole moment equal to $29 \pm 1 \text{ \AA}^3$. This difference polarizability is significantly larger than the value of 10 \AA^3 reported by Ara and Ahmed for perylene mixed aggregates in a PMMA thin film,⁸⁶ and also larger than the trace of the difference polarizability of the flavin S₁₀ transition, 23 \AA^3 .⁸⁸ The computed transition dipole moment of PO implicitly

solvated in toluene is along the long axis of the PDI ring system, meaning that the component of the difference polarizability along the long axis of the PDI ring system is $29 \pm 1 \text{ \AA}^3$. As the trace of the difference polarizability tensor is equal to the sum of the main-diagonal components of the difference polarizability tensor, the component of the difference polarizability orthogonal to the long axis of the molecule is approximately $42 \text{ \AA}^3 - 29 \text{ \AA}^3 = 13 \text{ \AA}^3$, assuming that the off-diagonal components of the difference polarizability tensor are small. Reviewing Figure 4.3, it appears that the redistribution of electron density following excitation is mostly symmetric about the PDI plane, indicating that the greater component of the 13 \AA^3 of difference polarizability orthogonal to the long axis of the molecule is likely along the short axis of the PDI plane. The theoretically computed $Tr\Delta\bar{\alpha}_{10}$ is 26.7673 \AA^3 , with component of the difference polarizability along the long axis of the molecular, parallel to the transition dipole moment, is $\Delta\bar{\alpha}_{10_{xx}} = 13.973 \text{ \AA}^3$, $\Delta\bar{\alpha}_{10_{yy}} = 12.7666 \text{ \AA}^3$, and $\Delta\bar{\alpha}_{10_{zz}} = 0.0277 \text{ \AA}^3$. This theoretical value for the $Tr\Delta\bar{\alpha}_{10}$ is 36% lower than the measured value of 42 \AA^3 , and indicates a more equitable change in polarizability along the long and short axes of the PO molecule, but confirms the interpretation that the majority of change of polarizability of PO upon excitation is parallel to the PDI plane, and that the change in polarizability perpendicular to the plane is negligible.

Relative shifts in trace polarizability are difficult to conceptualize intuitively. A more useful metric for interpreting the magnitude of the difference polarizability is the role played by the difference polarizability is shifting the vertical excitation energy of PO as a function of the applied electric field. A polarizability volume of $1 \text{ \AA}^3 = 1.113 \times 10^{-40}$

$\text{C m}^2 \text{V}^{-1}$.¹⁶⁴ An electric field of 1 MVcm^{-1} (10^8 Vm^{-1}), which is on the order of internal electric field found within Organic Light Emitting Diodes⁷² and Organic Field Effect Transistors,⁷³ therefore can induce a difference dipole moment of up to $-1.113 \times 10^{-32} \text{ Cm}$ ($-3.337 \times 10^{-2} \text{ D}$) per cubic Angstrom of difference polarizability. PO has a maximum uniaxial difference polarizability of 29 \AA^3 , so that an electric field of 1 MVcm^{-1} directed along the long axis of the molecule would induce a dipole moment of $-3.228 \times 10^{-39} \text{ Cm}$, or -0.9677 D . A dipole moment of 1 D is equal to a band gap Stark tuning rate of $16.79 \frac{\text{cm}^{-1}}{\text{MV/cm}}$, meaning that the change in polarizability of PO upon excitation coupled with an applied electric field of 1 MVcm^{-1} along the molecular long axis tunes the band gap by -16.25 cm^{-1} , which is less than 0.01% of the transition S_{10} transition energy of 19011 cm^{-1} . In this manner, the structural symmetry and limited conformational flexibility of PDI render the monomer's electro-optical band gap nearly independent of tuning by electric fields on the order of those found within molecular electronic devices. Symmetry-breaking derivatization of perylene diimide may, however, allow a tunable parameter for the improvement of PDI-dependent molecular electronic devices.

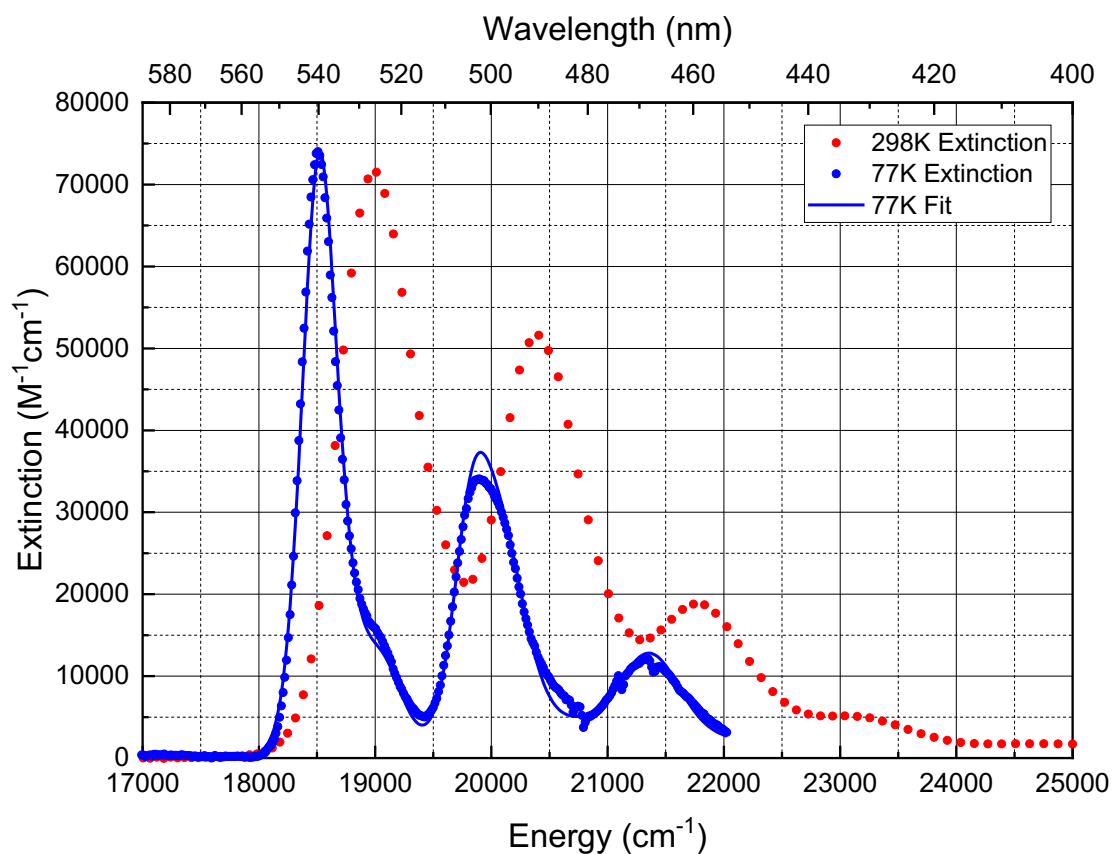


Figure 4.1. 298K and 77K extinction spectra of Perylene Orange, with fit to 77K spectrum. The 77K spectrum is an average of three replicates. Error bars for the 77K extinction signifying ± 1 standard deviation are smaller than the diameter of the blue circles representing the 77K extinction, and are not included.

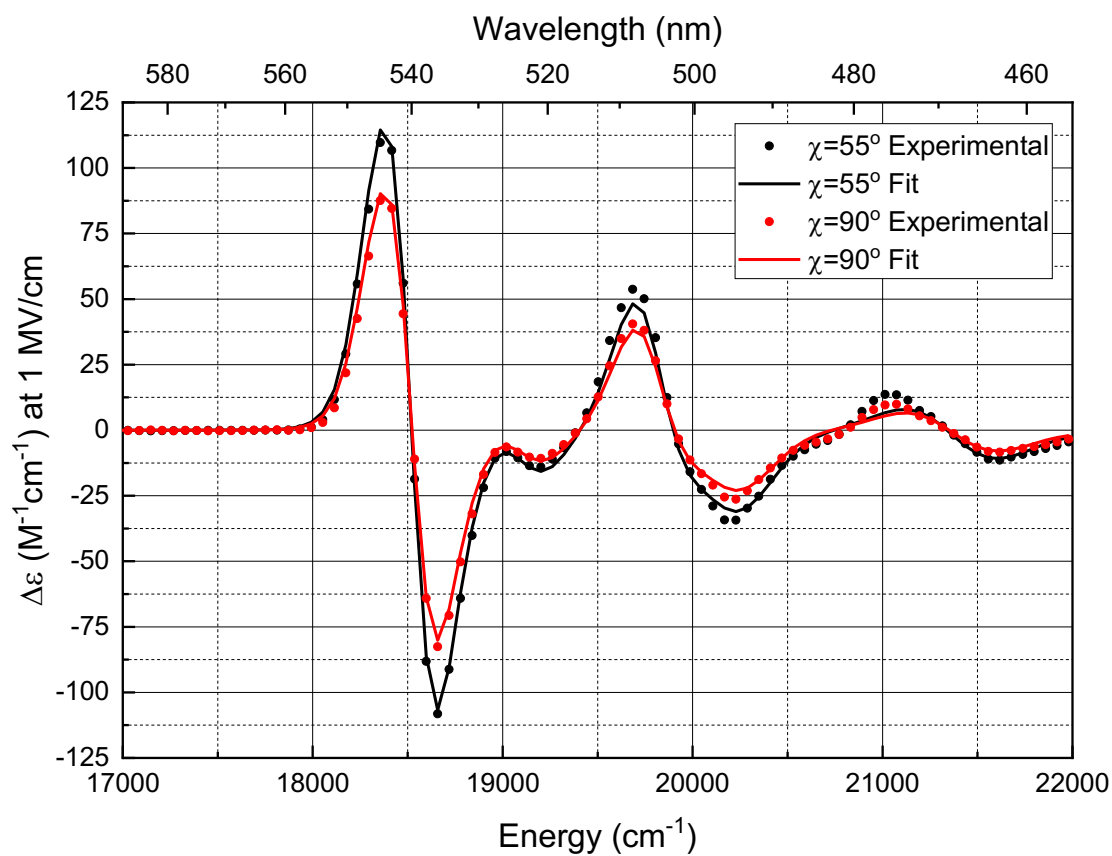


Figure 4.2. Experimental and fitted Stark spectra. Experimental spectra are an average of three replicates. Error bars for both experimental spectra signifying ± 1 standard deviation are smaller than the diameter of the circles representing the data points, and are not included.

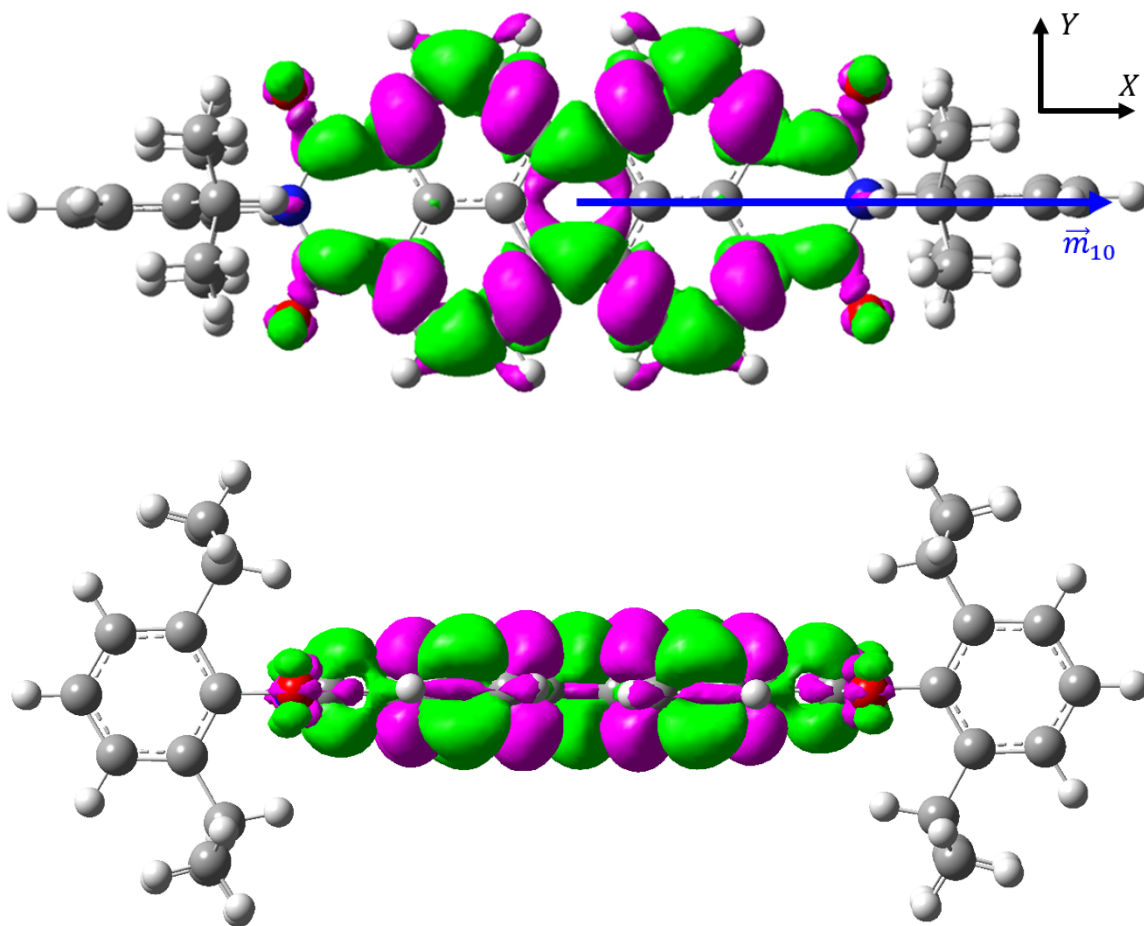


Figure 4.3. Perylene Orange S_{10} electronic transition difference density map. Two views of the change in electron density upon excitation of Perylene Orange, rendered at an isovalue of $0.0025 \text{ e}^-/\text{au}^3$. In this figure, green corresponds to a gain in electron density, whereas purple signifies a more electropositive region. In the upper pane, the vector \vec{m}_{10} is the computed transition dipole moment.

Table 4.1. First ten excited states of Perylene Orange implicitly solvated in toluene. calculated at the B3LYP/6-31+G(d)/PCM level of theory using Gaussian 16W. For the components of the transition dipole moments (TDMs), the origin is located at the center of mass, and the x- and y-axes are in the plane of the perylene core, with the x-axis passing through the two nitrogen atoms.

Excitation Number	Energy (eV)	Wavelength (nm)	Oscillator Strength	TDM X (au)	TDM Y (au)	TDM Z (au)
1	2.3029	538.38	1.0144	4.2402	0.0000	0.0000
2	2.5980	477.23	0.0000	0.0002	0.0000	0.0000
3	2.6025	476.41	0.0055	0.2945	0.0000	0.0000
4	2.7896	444.45	0.0000	0.0000	-0.0121	-0.0002
5	2.7917	444.11	0.0000	0.0000	-0.0004	0.0079
6	3.2482	381.70	0.0001	0.0001	0.0335	0.0008
7	3.2493	381.57	0.0000	0.0000	-0.0032	0.0083
8	3.3526	369.81	0.0000	0.0000	-0.0160	0.0000
9	3.4911	355.14	0.0000	0.0001	0.0050	0.0003
10	3.5351	350.72	0.0000	0.0000	0.0000	0.0000

CHAPTER 5

FLAVIN CHARGE REDISTRIBUTION UPON OPTICAL EXCITATION IS INDEPENDENT OF SOLVENT POLARITY

5.1 Overview

Flavin absorption spectra encode molecular details of the flavin's local environment through coupling of local electric fields with the chromophore's charge redistribution upon optical excitation. Translating experimentally-measured field-tuned transition energies to local electric field magnitudes and directions across a wide range of field magnitudes requires that the charge redistribution be independent of the local field. We have measured the charge redistribution upon optical excitation of the derivatized flavin TPARF in the non-hydrogen bonding, non-polar solvent toluene, with and without a tridentate hydrogen-bonding ligand, DBAP, using electronic Stark spectroscopy. These measurements were interpreted using TD-DFT finite field and difference density calculations. In comparing our present results to previous Stark spectroscopic analyses of flavin in more polar solvents, we conclude that flavin charge redistribution upon optical excitation is independent of solvent polarity, indicating that dependence of flavin transition energies on local field magnitude is linear with local field magnitude.

5.2 Sample Preparation and Computational Methods

Tetraphenylacetyl riboflavin (TPARF) and dibenzylamidopyridine (DBAP) were synthesized and purified as previously described¹³⁴. Toluene was of spectroscopic grade, purchased from Sigma-Aldrich, and freshly dried over 3 Å molecular sieves (Fisher Scientific) before use. Room temperature UV/vis spectra were recorded using an HP8453 Diode Array Spectrophotometer and a 1.0 cm path-length quartz cuvette (Spectrocell).

The extinction coefficient of TPARF in toluene at 298K was determined by dissolving 130 mg of TPARF in 10.00 mL of anhydrous toluene followed by serial dilutions of the initially prepared solution and obtaining the absorption spectrum of each diluted solution. Plotting the absorbance at the maximum of the S₁₀ transitions (~450 nm) as a function of TPARF concentration, gives the S₁₀ extinction coefficient from the slope of the best fit line. The extinction coefficient of TPARF in toluene quantitatively ligated to DBAP was determined by adding DBAP in a 2:1 mole ratio to a solution of known TPARF concentration, and measuring the absorption spectrum of the resulting solution.

Lumiflavin (7,8,10-trimethylisoalloxazine, Lf) was used as a minimal flavin to represent TPARF under the assumption that the TPARF's tetraphenylacetylribose substituent couples weakly with the core flavin heterocycle's electronic transitions. The structure of DBAP was also simplified for computational tractability by substituting methyl groups for the phenyl substituents, yielding diformamidopyridine (DFAP). The nuclear geometries of lumiflavin and the lumiflavin:diformamidopyridine complex implicitly solvated¹⁵⁸ in toluene were optimized, respectively, at the B3LYP/6-311+G(2d,p)/PCM and ω B97/6-311+G(2d,p)/PCM level of theory using Gaussian16 Rev C.01.¹³⁹ The B3LYP functional was used to study local excitations of lumiflavin implicitly solvated in toluene because this functional has previously been shown to yield theoretical flavin electro-optical charge redistribution parameters agreeing closely with experiment. The ω B97 functional was used to model charge-transfer excitations delocalized over the lumiflavin:diformamidopyridine complex because this functional has been shown to offer a good compromise between accurately computing transition

energies and difference dipole moments for delocalized charge transfer excitations in π -stacked nucleobases.¹⁷⁹ A frequency calculation at the same level of theory was used to verify the geometry optimization, and an excited states calculation was performed to compute the ten lowest energy excited states of each system. The SCF and CI densities were computed for the ground and two lowest-energy experimentally-observed excited states, respectively, and the difference density was visualized using GaussView 6.1.¹⁴¹ The finite field method¹⁴⁰ was used to determine the theoretical difference dipole moment and angle between the transition dipole moment and difference dipole moment for the experimentally-observed S₁₀ and S₂₀ transitions of each system.

5.3 Results

Room-temperature absorption spectra of TPARF and TPARF:DBAP in anhydrous toluene are given in Figure 5.1, and the low-temperature absorption spectra are given in Figure 5.2. A TPARF concentration of 2.42 mM was used for the low-temperature absorption spectrum of TPARF in toluene, and a TPARF concentration of 3.60 mM was used for the Stark spectra of TPARF in toluene. A TPARF concentration of 3.30 mM, and a DBAP concentration of 6.60 mM, was used for the low-temperature absorption spectrum of TPARF:DBAP in toluene. For the TPARF:DBAP Stark spectra, the concentration of TPARF was 3.34 mM, and the concentration of DBAP was 6.68 mM.

The solubility of TPARF in benzene is reported to be greater than 250 mM¹³⁴. However, to verify that the no aggregation occurs of TPARF in toluene occurs at, and immediately exceeding, the concentrations used in this study, absorption spectra of TPARF in toluene were recorded for a number of solutions of TPARF in toluene ranging

from 8.00 μM to 4.00 mM (data not shown). No change to the lineshape at the red-edge of the absorption spectrum was observed over this concentration range, indicating either that no aggregation occurs or that aggregation does not perturb the electronic transition. A comparison of the transition energies and extinctions of the first two near-UV transitions of TPARF and TPARF:DBAP in toluene at 298 K and 77 K is summarized in Table 5.1. The 298 K spectrum of TPARF in toluene shows two broad peaks centered at 22470 cm^{-1} and 29150 cm^{-1} , with peak extinction coefficient of 10400 $\text{M}^{-1}\text{cm}^{-1}$ and 6330 $\text{M}^{-1}\text{cm}^{-1}$ at these respective energies. The lower energy band, corresponding to the S_{10} electronic transition, exhibits poorly resolved vibronic structure at 21230 cm^{-1} and 23580 cm^{-1} . Cerda *et al.* report that the maximum extinction for TPARF in benzene at 298 K occurs at 22470 cm^{-1} , with an extinction of 12600 $\text{M}^{-1}\text{cm}^{-1}$,¹³⁴ indicating that the toluene solvent, which is less likely to promote stable π -stacking between solute and solvent than the benzene solvent due to the presence of the sterically-hindering methyl substituent, reduces the extinction of the TPARF solute S_{10} by 17.5% without significantly altering the transition energy. At 77 K, attenuation of inhomogeneous broadening at low-temperature causes both the S_{10} and S_{20} bands to become narrower, with increased peak amplitude and more highly-resolved vibronic structure. The S_{10} band maximum shifts in energy by -220 cm^{-1} to 22250 cm^{-1} , and the peak extinction increases by 51% to 15700 $\text{M}^{-1}\text{cm}^{-1}$, with increased vibronic structure. The S_{20} band maximum shifts in energy by -1960 cm^{-1} , and the peak extinction increases by 9% to 6900 $\text{M}^{-1}\text{cm}^{-1}$, with a vibronic shoulder emerging at 28390 cm^{-1} .

The 298 K absorption spectrum of TPARF:DBAP in toluene is similar in lineshape to that of TPARF without the tridentate hydrogen-bonding ligand with two notable exceptions. First, the S₁₀ peak extinction slightly red-shifts by -50 cm⁻¹ from 22470 cm⁻¹ to 22420 cm⁻¹, with a 42.3% increase in extinction coefficient from 10400 M⁻¹cm⁻¹ to 14800 M⁻¹cm⁻¹. Second, the S₂₀ peak extinction red-shifts by -160 cm⁻¹ from 29150 cm⁻¹ to 28990 cm⁻¹, with a 41.2% increase in peak extinction from 6330 M⁻¹cm⁻¹ to 8940 M⁻¹cm⁻¹. Cerda *et al.* observed a -100 cm⁻¹ red-shift in the TPARF S₁₀ transition energy upon adding DBAP in benzene, which is more negative than the -50 cm⁻¹ shift that we observe in toluene, indicating that the binding energy between TPARF and DBAP in toluene is less negative than in benzene, with a consequently higher dissociation constant. Furthermore, the 42.3% increase in peak extinction from 10400 M⁻¹cm⁻¹ to 14800 M⁻¹cm⁻¹ that we observe for TPARF vs. TPARF:DBAP in toluene is larger than the 15.1% increase in extinction from 12600 M⁻¹cm⁻¹ to 14500 M⁻¹cm⁻¹ that Cerda *et al.* for TPARF vs. TPARF:DBAP in benzene. Cerda *et al.* do not report the S₂₀ transition energy or extinction for either TPARF or TPARF:DBAP in benzene, preventing comparison to our data in toluene.

Upon cooling to 77 K, the TPARF:DBAP absorption spectrum (Figure 5.2) becomes more unique. Most notably, the oscillator strength of the S₁₀ transition redistributes among the coupled vibronic components such that the low-energy vibronic shoulder rises in extinction to 21910 M⁻¹cm⁻¹, nearly equal to that of the S₁₀ transition's central band at 21190 M⁻¹cm⁻¹. Ligation of DBAP to TPARF inductively perturbs electron density in the hydrogen-bonded flavin pyrimidine ring, likely shifting the

overlap between coupled vibrational modes in the electronic ground and first excited state, increasing the Huang-Rhys parameters of one or more low frequency coupled vibrational modes and augmenting extinction at the red edge of the S_{10} band. Similar dependence of vibronic coupling on intermolecular hydrogen bonds has been observed for a heptazine derivative hydrogen-bound to a variety of substituted phenols.¹⁶⁵ In our previous Stark spectroscopy study of flavoenzyme charge transfer, examining the role of a stacked *p*-chlorophenol ligand in tuning the charge distribution upon optical excitation of oxidized FMN in Old Yellow enzyme,¹⁹ interaction of the flavin with a charge transfer ligand also redistributed oscillator strength of the S_{10} transition band, increasing the extinction of the red-edge vibronic shoulder to that of the central band of the S_{10} transition. The hydrogen bonds between DBAP and TPARF increase in strength at low temperature, evidenced by the -410 cm^{-1} red shift upon cooling from 298 K to 77K. On the basis of our ground state frequency calculation of lumiflavin hydrogen bound to diformamidopyridine, implicitly solvated in toluene, five normal modes include oscillation of the three intermolecular hydrogen bonds. The theoretical frequencies of these normal modes range from 180 cm^{-1} to 210 cm^{-1} . These hydrogen bond energies are approximately equal to kT at 298K (207 cm^{-1}), and are approximately four times kT at 77K (53.5 cm^{-1}). At the lower temperature of 77K, therefore, the average intermolecular potential energy of the hydrogen-bound complex is more negative than at 298K because, via the Boltzmann distribution, a greater proportion of the hydrogen bonds will be in the ground vibrational state. The stronger hydrogen bonding, in turn, stabilizes the flavin first excited singlet state to a greater extent. The S_{20} band of the TPARF:DBAP system red-

shifts upon cooling by -2160 cm^{-1} from 28990 cm^{-1} to 26830 cm^{-1} , with extinction increasing from $8940\text{ M}^{-1}\text{cm}^{-1}$ to $11500\text{ M}^{-1}\text{cm}^{-1}$.

High signal-to-noise Stark spectra were obtained for both systems at two angles of incident light polarization to the applied field, $\chi=54^\circ$ and $\chi=90^\circ$. Stark spectra were measured by Raymond F. Pauszek III. Representative Stark spectra normalized to an applied field of 1 MV/cm are shown in Figure 5.3. Stark spectroscopy enables deconvolution of overlapping electronic transitions on the basis of the transitions, electrochromism, the dependence of the amplitude of the Stark signal on χ . The electrochromisms of the two systems are similar, in that for both TPARF and TPARF:DBAP in toluene the S_{10} Stark spectrum is independent of χ , indicating that the angle between $\Delta\mu$ and ζ_A is close to the magic angle, while the S_{20} transition of both systems is χ -dependent, as evidenced by divergence of the Stark spectra measured at the two different χ values employed. The difference in line shape for the S_{10} transition Stark spectrum of TPARF versus TPARF:DBAP around 21000 cm^{-1} results from the difference in relative extinctions of the red-edge of the S_{10} bands as observed in the 77K absorption spectra of the two chromophore systems.

Experimental electro-optical charge redistribution parameters for TPARF in toluene and TPARF:DBAP in toluene are summarized in Table 5.2. Theoretical values for $|\Delta\vec{\mu}_{fi}|$ and ζ_A of Lf and Lf:DFAP implicitly solvated in toluene are given in Table 5.3. Figure 5.4 presents the theoretical ground state dipole moment and theoretical S_{10} and S_{20} transition dipole moments for Lf and Lf:DFAP implicitly solvated in toluene, as well as the experimental S_{10} and S_{20} difference dipole moments positioned in the molecular

frame relative to the respective theoretical transition dipole moments via the experimental ζ_A value. Figure 5.5 presents the difference density maps ($\Delta\rho = \rho_n - \rho_0$) for the S_{10} and S_{20} transitions of Lf and Lf:DFAP at different isovalues. For both TPARF and TPARF:DBAP in toluene, the S_{20} transition is characterized by greater charge redistribution than the S_{10} transition, which is generally consistent with our previous studies of flavin Stark spectroscopy. The difference permanent dipole moment for the S_{10} transition of free TPARF in toluene, 1.7 ± 0.015 D, increases by 153% to 2.6 ± 0.23 D upon binding to the DBAP ligand, with ζ_A , $52^\circ \pm 21^\circ$ for TPARF and $51^\circ \pm 9.7^\circ$ for TPARF:DBAP, remaining constant within experimental error. The finite field calculations for Lf and Lf:DFAP implicitly solvated in toluene, however, predict that the difference permanent dipole moment of Lf falls by 13% from 1.9665 D to 1.7116 D upon DFAP ligation, with ζ_A , 66.27° for Lf and 64.77° for Lf:DFAP, changing little. Similarly, the experimental difference dipole moment of the S_{20} transition increases by 142% from 6.7 ± 0.018 D for free TPARF in toluene to 9.5 ± 1.0 D for TPARF:DBAP, with ξ_A , $34^\circ \pm 0.14^\circ$ for TPARF and $29^\circ \pm 12^\circ$ for TPARF:DBAP, remaining constant within experimental error. Finite field calculations concur with experimental results for the S_{20} difference dipole moment, in that the theoretical difference dipole moment increases by 263% from 5.7746 D for Lf to 7.2945 D for Lf:DFAP, with ξ_A , 11.31° for Lf and 17.11° for Lf:DFAP, showing little variation upon complex formation.

The increase in the difference dipole moment for both transitions upon formation of the TRAPF:DBAP complex suggests the possibility of introduction of a novel charge transfer component to the excitations resulting from delocalization of the electronic

excited states through the co-planar adjacent aromatic pi-electron systems of the isoalloxazine and pyrimidine heterocycles, mediated by the intervening hydrogen bonds. Interestingly, one would expect that introducing charge transfer character to the electronic excitations would induce the ζ_A angle formed between the transition and difference permanent dipole moments for the transitions to shift towards zero.¹⁶⁶ However, the experimental values of ζ_A for both the S_{10} and S_{20} remain unchanged following complex formation, within estimated experimental error, even with the increase in the difference permanent dipole moment induced by DBAP binding. The large change in difference dipole moment and lack of change in ζ_A indicates that the charge transfer component of the S_{10} and S_{20} electronic excitations induced by binding of TPARF to DBAP is small relative to the redistribution of electron density localized to the flavin heterocycle, and ζ_A for these transitions is determined by the dominant local redistribution of electron density upon excitation. This conclusion is consistent with the theoretical calculations. In Figure 5.4, the center of mass of the two systems is offset relative to one another due to the addition of the DFAP ligand, but the transition dipole moments are similarly positioned relative to the flavin molecular framework. The S_{10} transition dipole moments of Lf and Lf:DFAP are nearly parallel, while the S_{20} transition dipole moment of Lf:DFAP is 18° further below the long axis of the flavin ring system than that of Lf.

The difference densities presented in Figure 5.5 show that at an isovalue of $0.0025 \text{ e}^-/\text{\AA}^3$ the S_{10} transition for both Lf and Lf:DFAP is concentrated along the diazarene bridge connecting the pyrazine and pyrimidine rings of the flavin heterocycle,

while the S_{20} transition is characterized by more delocalized charge redistribution from the xylene to pyrimidine rings of the flavin heterocycle. The DFAP ligand does not contribute to either transition at this isovalue. Only upon reducing the isovalue 10-fold to $0.00025 \text{ e}/\text{\AA}^3$ does the involvement of the DFAP ligand become apparent, validating the previous conclusion that first two singlet transitions of TPARF:DBAP include a minor contribution from intermolecular charge transfer, augmenting the difference dipole moments of the transitions without significantly changing the position of the difference dipole moment relative to the flavin molecular framework.

The isotropic trace of the difference polarizability for the S_{10} transition of free TPARF in toluene increases by 683% from $12 \text{ \AA}^3 \pm 3.1 \text{ \AA}^3$ to $81.9 \text{ \AA}^3 \pm 7.6 \text{ \AA}^3$ upon binding to DBAP, and the trace difference polarizability of the S_{20} transition of TPARF in toluene increases by 242% from $156 \text{ \AA}^3 \pm 4.9 \text{ \AA}^3$ to $378 \text{ \AA}^3 \pm 34 \text{ \AA}^3$ following complex formation. The increase in the trace polarizability upon binding of TPARF to DBAP further substantiates the conclusion that the S_{10} and S_{20} transitions acquire charge transfer character with ligation, expanding the volumes occupied by the delocalized excited states relative to the more localized ground state. Unlike as is observed for the difference dipole moment of TPARF, the difference polarizability does indicate a change in the direction of charge redistribution within the molecular frame following DBAP ligation for both the S_{10} and S_{20} transitions, with the anisotropic component of the difference polarizability projected along the transition dipole moment increasing by 1318% for the S_{10} transition from $2.2 \text{ \AA}^3 \pm 1.0 \text{ \AA}^3$ for free TPARF to $29.0 \text{ \AA}^3 \pm 15 \text{ \AA}^3$ for TPARF:DBAP, and increasing by 183% for the S_{20} transition from $117 \text{ \AA}^3 \pm 10 \text{ \AA}^3$ to $214 \text{ \AA}^3 \pm 88 \text{ \AA}^3$.

Returning to the theoretical transition dipole moments plotted in Figure 5.4, it is apparent that the S_{10} transition dipole moment, and to a lesser extent the S_{20} transition dipole moment, is oriented directly away from the symmetry axis of the DFAP ligand. The increase in polarizability imparted to the excited states of the ligated complex upon charge transfer through the co-planar π -electron systems is parallel to the symmetry axis of the tridentate ligand, meaning that the increased polarizability should also predominantly be along the transition dipole moments of the two excitations, as is observed.

The TD-DFT calculations correctly predict that the oscillator strength of the Lf S_{10} transition significantly increases by 223% upon ligation to DFAP, to 0.6274 from 0.2818. This increase compares favorably with the 123% increase in integrated energy-weighted extinction for the S_{10} transition at 77K of TPARF upon DBAP binding, from 2380.29 $M^{-1}cm^{-1}$ to 3425.73 $M^{-1}cm^{-1}$. A potentially useful consequence of the increase in charge redistribution and increase in S_{10} oscillator strength for TPARF upon DBAP binding is the possibility of using a charge transfer ligand such as DBAP that hydrogen bonds to the flavin pyrimidine ring to tag flavin cofactors *in vivo* via second harmonic generation. Such hydrogen-bond enhanced second harmonic generation has previously been observed in non-polar chiral coordination polymers,¹⁶⁷ and could be used to follow flavin localization, transport, and metabolism in living cells. The probability of resonance-enhanced second harmonic generation by an oriented ensemble of chromophores, such as flavin cofactors transiting cellular or sub-cellular, i.e. mitochondrial, membranes,^{145, 146} is proportional to the product of the squared difference

dipole moment and the squared integrated energy-weighted extinction of a given electronic transition in resonance with the excitation source.¹⁴⁷⁻¹⁵² The S₁₀ transition of flavin is in resonance with common Ti:sapphire oscillators, and has previously been used to measure resonance-enhanced second harmonic generation by the first optical transition of molecules of oxidized flavin adenine dinucleotide bound by glucose oxidase at an air/water interface.¹⁵⁶ The difference dipole moment of the S₁₀ transition of TPARF:DBAP is 1.53 times that of TPARF, and the integrated energy-weighted extinction of TPARF:DBAP is 1.23 times that of TPARF, meaning that the probability of second harmonic generation by the ligated flavin should be 3.54 times that of the free flavin.

5.4 Discussion

Our primary purpose in measuring charge redistribution upon optical excitation of TPARF in toluene was to establish a baseline set of flavin electro-optical charge redistribution parameters minimally perturbed by the local molecular environment with which to interpret the specific role of more perturbing environments in tuning flavin's ground and excited state electronic structures. However, a global, quantitative comparison of measured electro-optical charge redistribution parameters for flavins in different environments is complicated by the difficulty in accurately computing the local field correction factor, f_C , that is specific to each molecular environment. A first-order approximation of the local field correction factor is possible for chromophores dissolved in isotropically-distributed simple solvents by assuming the solvent to be a continuous dielectric solvating the chromophore in an elliptical shell, with no specific interactions,

i.e., hydrogen bonds, punctuating the structure of the shell. This approximation is most valid for solvents such as toluene. For comparison of the electro-optical charge redistribution parameters of flavin in toluene reported in this contribution to previously published charge redistribution parameters in other environments characterized by hydrogen-bonding, for example N(3)-methyl-N(10)-isobutyl-flavin (N3FI) in ethanol, butanol, and 2-methyltetrahydrofuran (2-MTHF), it is possible to eliminate uncertainty in determination of the local field correction factor by taking ratios of charge redistribution parameters for the flavin S₂₀ and S₁₀ transitions. As the local field correction factor is constant for a given environment, the contribution of the local field correction factor to each transition will cancel upon division. Figure 5.6 presents plots comparing transition energies and ratios electro-optical charge redistribution parameters for the S₁₀ and S₂₀ transitions of all flavin-solvent systems studied. Ratios of charge redistribution parameters for the solvents utilized are plotted in terms of solvent polarity indicators, (E_N^T), derived from the solvatochromic behavior of betaine dyes.¹⁶⁸

We begin our comparison of flavin charge redistribution upon optical excitation in different solvents with a discussion of the flavin S₁₀ and S₂₀ transition energies in these solvents. The transition energies reported here are the energies at the maximum extinction for each band, and therefore include both the pure electronic transition energy and additional energy exciting one or more coupled vibrational modes. A single set of charge redistribution parameters adequately fits the Stark signal from each electronic transition for all flavin-solvent systems studied, so it is reasonable to assume that at the spectral resolution employed the interaction of coupled vibrations with the applied field

contributes minimally to the field-tunability of the flavin S₁₀ and S₂₀ transitions, and, therefore, that consideration of energies at the maximum extinction of each band is sufficient to understand the net role of the local environment in tuning the energetics of the electronic transition corresponding to the band.

Two general assumptions underlie the Onsager reaction field approach¹⁶⁹ to solvatochromism. The first of these assumptions is that the more polar the solvent, the larger the magnitude of the solvent reaction field induced by the ground state permanent dipole moment of the chromophore. The second of these assumptions is that electronic transitions with an angle between the ground state permanent dipole moment and difference dipole moment less than 90° are more red-shifted with increasing solvent polarity. Both the S₁₀ and S₂₀ electronic transitions of flavin are characterized by angles between the ground state permanent dipole moment and difference dipole moment that are less than 90°. Based on the solvent polarity indicators given in Figure 5.6b, therefore, it should be expected that the order of the transition energies for both transitions from the highest energy to the lowest energy should be TPARF in toluene, to N3Fl in 2-MTHF, to N3Fl in butanol, to N3Fl in ethanol. TPARF:DBAP does not fit cleanly into this analysis because of the strong hydrogen bonds forming the complex and stabilizing the flavin electronic excitations. The observed trend in transition energies shown in Figure 5.6a is very different than what is expected simply on the basis of solvent polarity.

The most red-shifted electronic transitions are those of TPARF:DBAP in toluene. These electronic transitions are stabilized by strong hydrogen bonds ligating the TPARF and DBAP molecules, as well as the tip-to-tail orientation of the molecules' ground state

permanent dipole moments. The second most red-shifted electronic transition energies are those of TPARF in toluene. Toluene is a low-dielectric material with a small dipole moment, and solely on the basis of polarity should minimally stabilize flavin's electronic transitions. However, toluene is capable of forming highly stabilizing $\pi - \pi$ stacking interactions with flavin, rationalizing the red-shift imparted to TPARF's S_{10} and S_{20} electronic transitions.

Koziol *et al.* have utilized density functional and perturbation electronic structure methods in conjunction with Monte Carlo simulated annealing and the Effective Fragment Potential method to determine the structure and binding energy of lumiflavin:benzene dimers.¹⁷⁰ They conclude that the most stable dimer orientation places the benzene above the diazarene bridge connecting the pyrazine and pyrimidine rings of the flavin heterocycle, imparting a stabilization energy of -13.29 kcal/mol, which is equivalent to -4648 cm^{-1} . Recalling the difference densities in Figure 5.5, both the S_{10} and S_{20} transitions involve significant charge redistribution through the flavin diazarene bridge moiety, establishing that these transitions are likely sensitive to stabilizing interactions with the $\pi - \pi$ stacking toluene solvent. As our purpose in completing Stark spectroscopy of TPARF in toluene was to measure flavin's native electro-optical charge redistribution parameters in a minimally-perturbing environment, this evidence of significant stabilization of flavin's electronic transitions through interaction with solvent suggests that a better choice of solvent would have been *n*-methylpentane, which also forms a transparent glass at 77 K and is both non-polar and incapable of $\pi - \pi$ stacking interactions. The next most stabilizing solvents were butanol and ethanol. Butanol is less

polar than ethanol, yet further red-shifts the transition energies than does ethanol. Finally, the highest-energy, most blue-shifted flavin electronic transitions are those of N3F1 in 2-MTHF, a non-polar, non-aromatic solvent incapable of $\pi - \pi$ stacking interactions.

Electronic transition energies are tuned by the local solvent environment via solvent electric field with a given transition's characteristic charge redistribution parameters. To better understand how specific fields yield specific shifts in transition energy, it is necessary to examine how the charge redistribution parameters themselves depend on the local electric field. As shown in Figure 5.6b, the charge redistribution parameters for flavin in a variety of solvent environments and polarities are, within experimental error, independent on the polarity or chemical interactivity of the solvents utilized. Because the S_{20} and S_{10} transitions are localized to different regions of the flavin heterocycle, if the charge redistribution parameters varied with the applied solvent reaction field, the S_{20}/S_{10} ratio of the charge redistribution parameters would be expected to diverge at larger solvent polarities, as the S_{20} transition is characterized by greater charge redistribution than the S_{10} transition, and the S_{20} difference dipole moment makes a smaller angle with the solvent reaction field templated by the flavin ground state permanent dipole moment.

The heterogeneous dielectric environment of flavoenzyme cofactor binding pockets also precludes approximation of the local field correction factors for these environments. The group has previously published on the Stark spectroscopy of oxidized FMN bound to *S. pastorianus* Old Yellow Enzyme (SpOYE) with and without a *p*-chlorophenol ligand,¹⁹ as well as oxidized and semiquinone FAD bound to *E. coli*

photolyase (EcPL).¹³² Table 5.4 summarizes the results of the oxidized flavoenzyme Stark spectroscopy studies.

The structure of the cofactor binding pockets of SpOYE and EcPL differ considerably. In SpOYE (PDB 1OYC),¹⁷¹ the flavin cofactor forms hydrogen bonds to the protein matrix at both carbonyls, with C2O hydrogen-bound to a positively charged arginine residue. N5 also forms a hydrogen bond with the hydrogen of a backbone amide nitrogen. In addition to the two hydrogen bonds to the flavin pyrimidine ring carbonyls, the pyrimidine ring is bounded by a histidine residue and a glutamine residue. A number of aromatic residues surround the substrate binding site adjacent to the flavin cofactor, but they are not in van der Waals contact with the flavin, attenuating the possibility of $\pi - \pi$ stacking interactions. However, the charge transfer ligand *p*-chlorophenol does form $\pi - \pi$ stacking interactions with the flavin cofactor once it binds within the pocket formed by the aromatic residues. The EcPL (PDB 1DNP)¹⁷² cofactor binding pocket is unique among flavoenzymes in that the FAD cofactor adenine heterocycle is stacked on the flavin heterocycle. Also, N1 of the flavin forms an intramolecular hydrogen bond with a proximal ribose hydroxyl group, C2O forms two hydrogen bonds with conserved water molecules, N3H forms a hydrogen bond with a backbone amide carbonyl, C4O forms a hydrogen bond with a backbone amide nitrogen, and N5 forms a hydrogen bond with an asparagine residue. Finally, photolyases exhibit a conserved arginine-aspartic acid salt bridge parallel to the flavin heterocycle plane and within 4 Å, with the dipole moment of the salt bridge directed nearly 180° to the flavin dipole moment.

Despite these significant structural differences, as can be seen in Table 5.4, the magnitudes of the S_{10} and S_{20} difference dipole moments are all within their respective experimental errors, as are the values of ζ_A for EcPL and SpOYE in the absence of the CT ligand, indicating that these parameters are weakly dependent on flavoenzyme active site cofactor binding pocket electric fields. The change in polarizability, however, is strongly dependent on the local environment. As was observed for the ligation of DBAP to TPARF in toluene, $\pi - \pi$ stacking interactions formed upon introduction of the *p*-chlorophenol ligand to SpOYE significantly increases the change in polarizability following optical excitation as the excited states delocalize through the coupled aromatic π -electron system.

To conclude, we have measured the charge redistribution upon optical excitation of the derivatized flavin TPARF in the non-hydrogen bonding, non-polar solvent toluene, with and without a tridentate hydrogen-bonding ligand, DBAP, using electronic Stark spectroscopy. These measurements were interpreted using TD-DFT finite field and difference density calculations. Our key finding is confirmation of earlier conclusions that flavin charge redistribution upon optical excitation is independent of perturbation by local electric fields, resulting from either interaction with the solvent, as is the case in the systems studied in this contribution, or with residues of flavoenzyme active site cofactor binding pockets, as was observed in previous studies. Independence of flavin electro-optical charge redistribution on the local environment causes flavin S_{10} and S_{20} visible transition energies to vary linearly with the component of the local environment electric field projected along the relevant difference dipole moment. As the S_{10} and S_{20} difference

dipole moments are both in the plane of the flavin heterocycle and make an angle of $\sim 40^\circ$ with one another, they offer complementary axes for estimating the magnitude and direction of local environment electric fields tuning flavin photophysics and reactivity directly from the perspective of the tuned flavin cofactor.

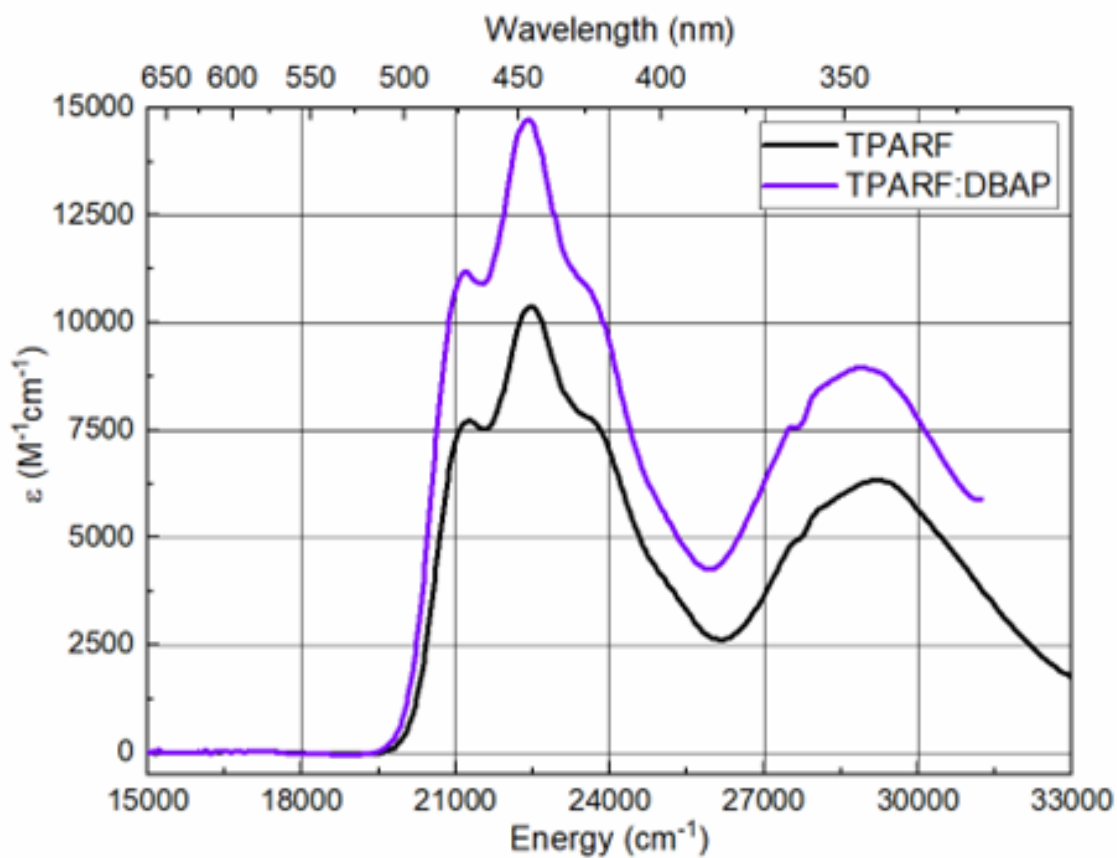


Figure 5.1. 298K absorption spectra of TPARF and TPARF:DBAP in toluene. The concentration of TPARF was 101 μM , and the concentration of TPARF:DBAP was 101 μM : 204 μM . The absorption spectrum of TPARF:DBAP was truncated at 31250 cm^{-1} (320 nm) to eliminate contribution of the DBAP absorption.

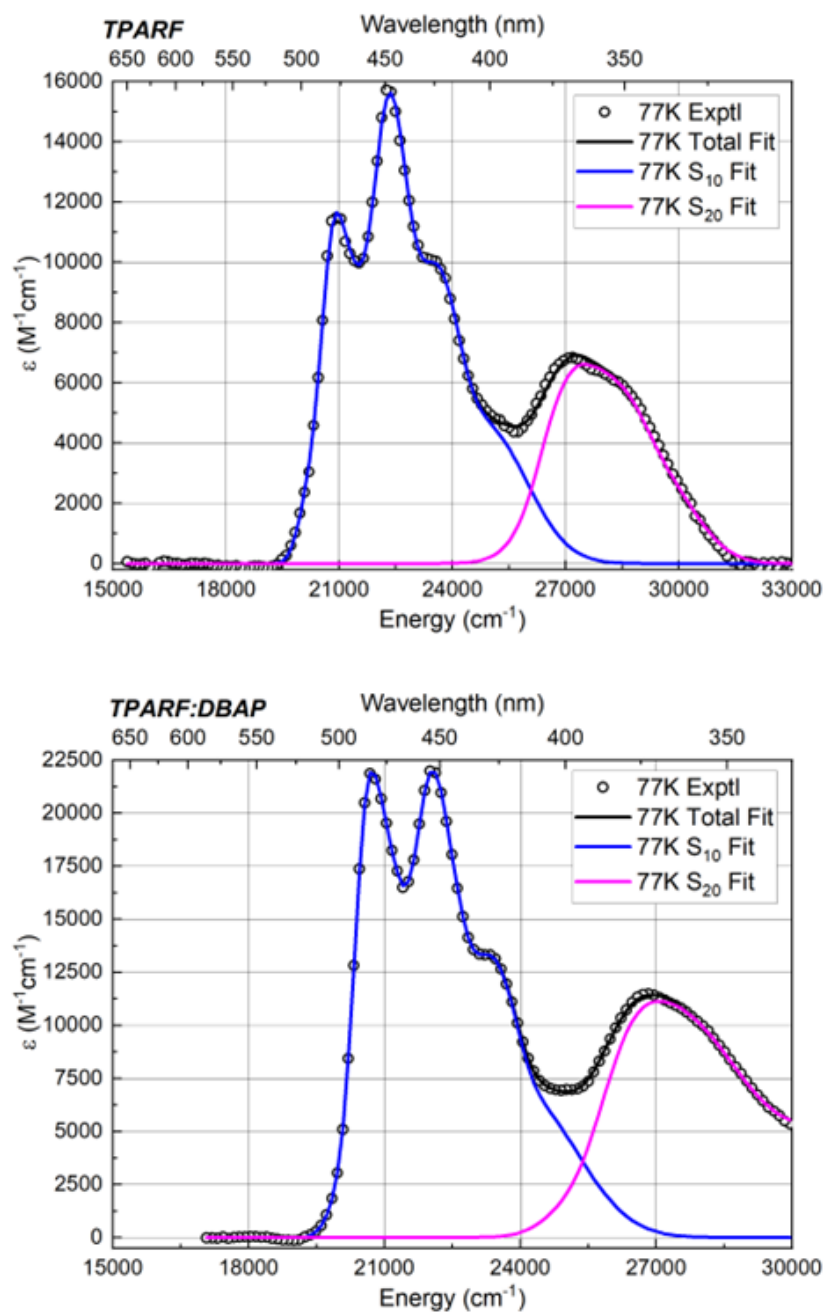


Figure 5.2. 77 K absorption spectra of TPARF and TPARF:DBAP. Transition-specific fits are in blue (S_{10}) and pink (S_{20}), and the total fit in black. For TPARF in toluene, the concentration of TPARF was 2.42 mM. For TPARF:DBAP in toluene, the concentration of TPARF was 3.30 mM and the concentration of DBAP was 6.60 mM.

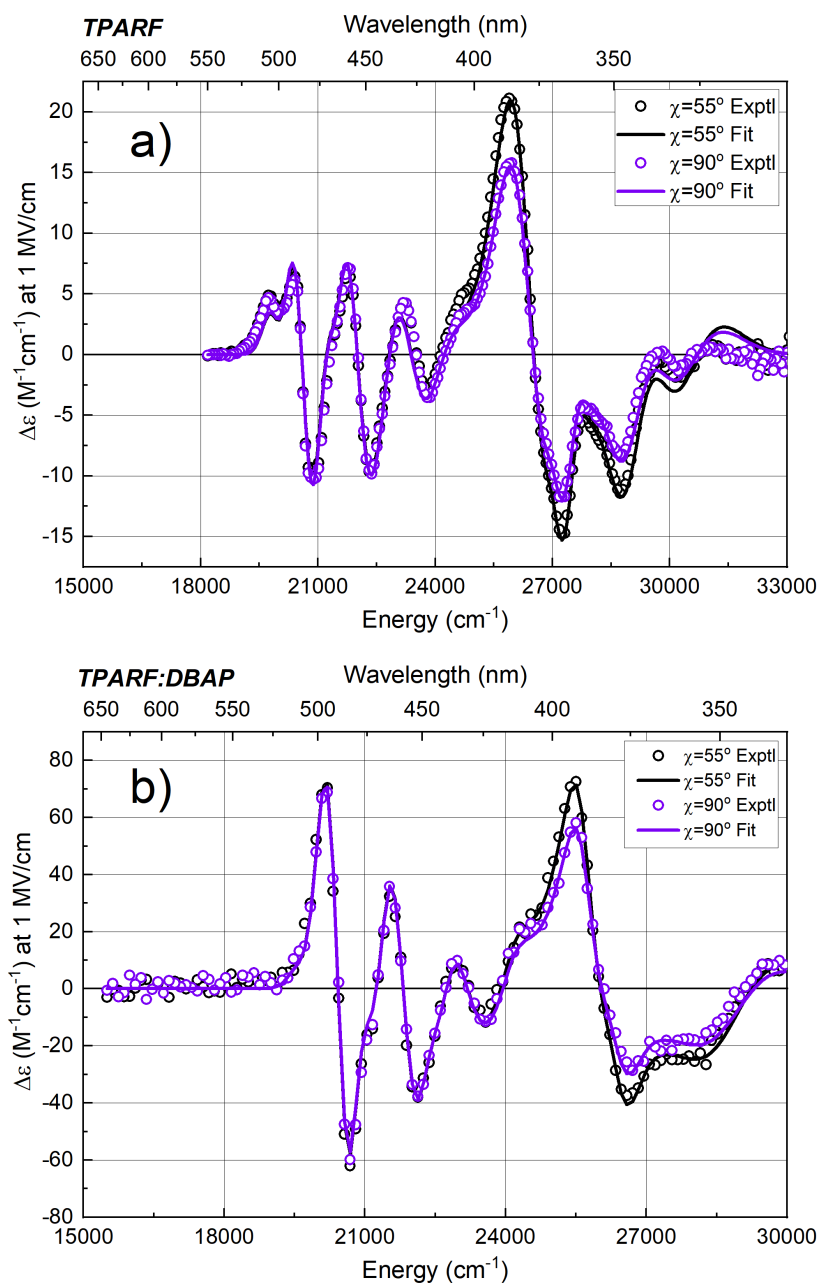


Figure 5.3. Stark spectra of TPARF and TPARF:DBAP in toluene, with fits. Spectra are normalized to an applied field of 1 MV/cm. TPARF in toluene, the concentration of TPARF was 3.60 mM. For TPARF:DBAP in toluene, the concentration of TPARF was 3.34 mM and the concentration of DBAP was 6.68 mM.

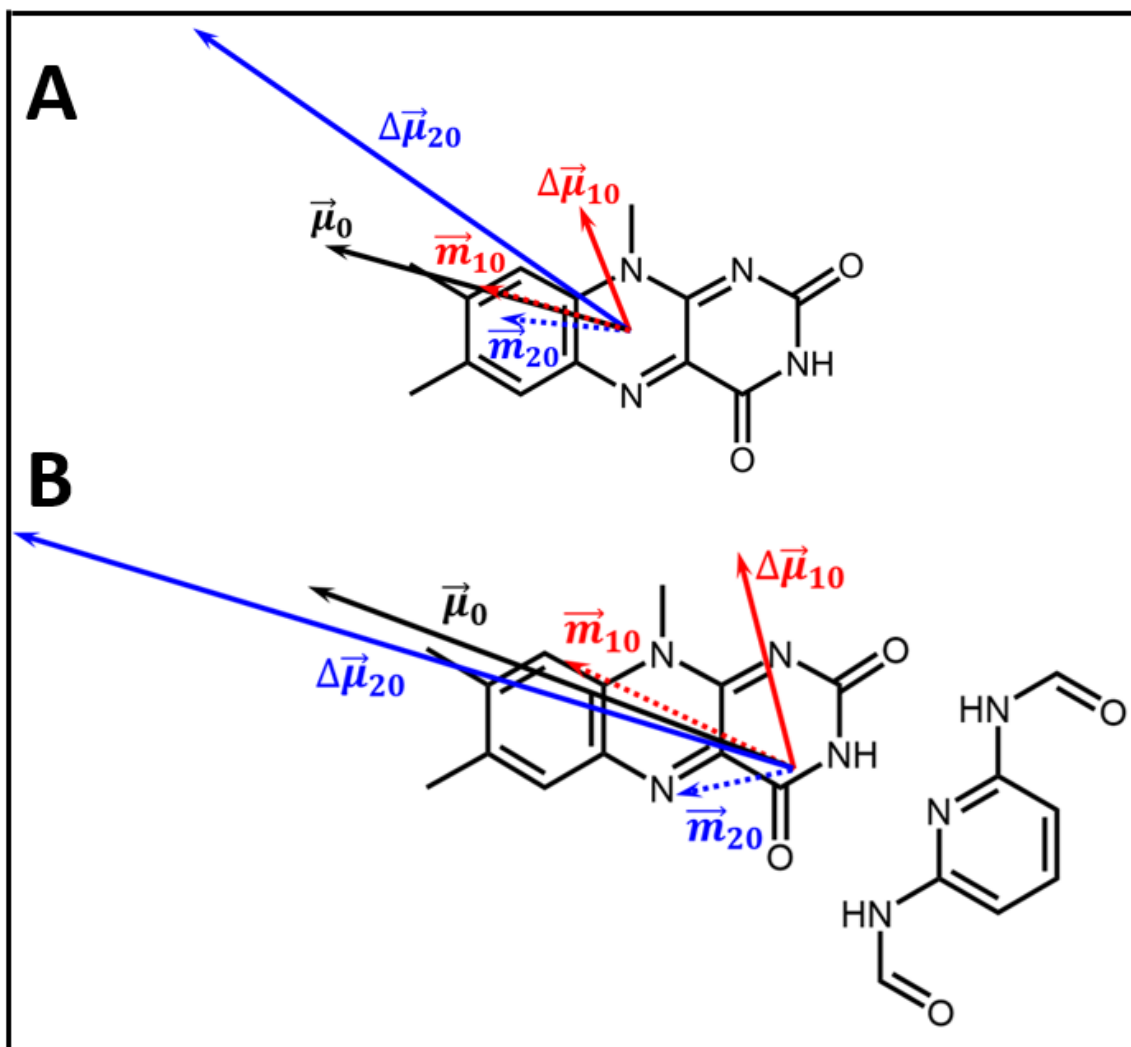


Figure 5.4. Vector diagrams of lumiflavin and lumiflavin:DFAP. Theoretical transition dipole moments (dotted arrows) with experimentally determined difference dipole moments (solid red and blue arrows) for (a) lumiflavin and (b) the lumiflavin:DFAP complex. All vectors are to scale except for the ground-state permanent dipole moments, which are at 1/3-scale.

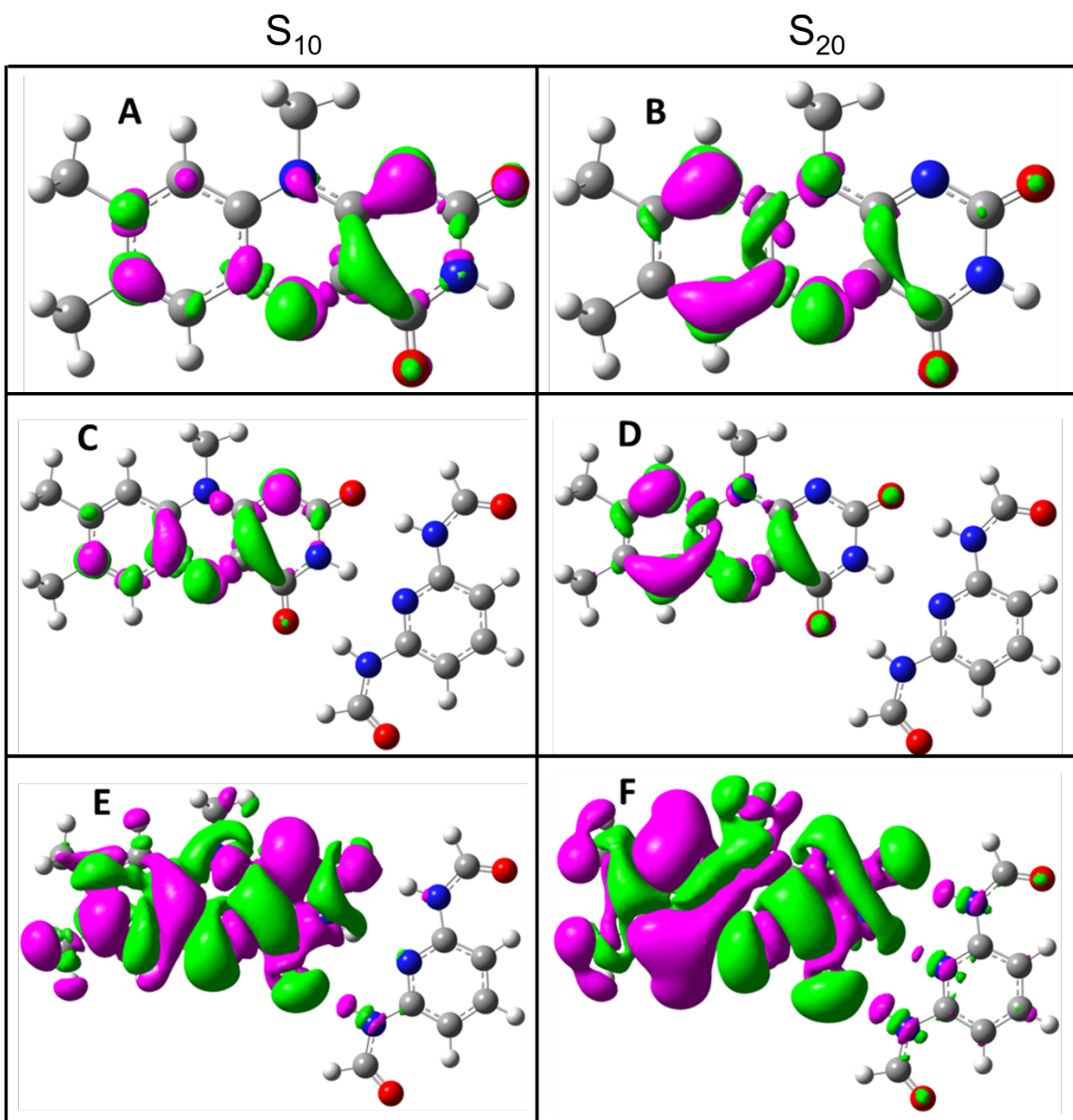


Figure 5.5. Difference density maps of lumiflavin and lumiflavin:diaformamidopyridine. Lumiflavin S_{10} (A) and S_{20} (B) transitions at an isovalue of $0.0025 \text{ e}^-/\text{\AA}^3$, and of lumiflavin:diaformamidopyridine S_{10} (C, E) and S_{20} (D, F) transitions at isovalues of $0.0025 \text{ e}^-/\text{\AA}^3$ (C, D) and $0.00025 \text{ e}^-/\text{\AA}^3$ (E, F). Green corresponds to regions gaining electron density following the electronic transition, and purple corresponds to regions becoming more electropositive following the electronic transition.

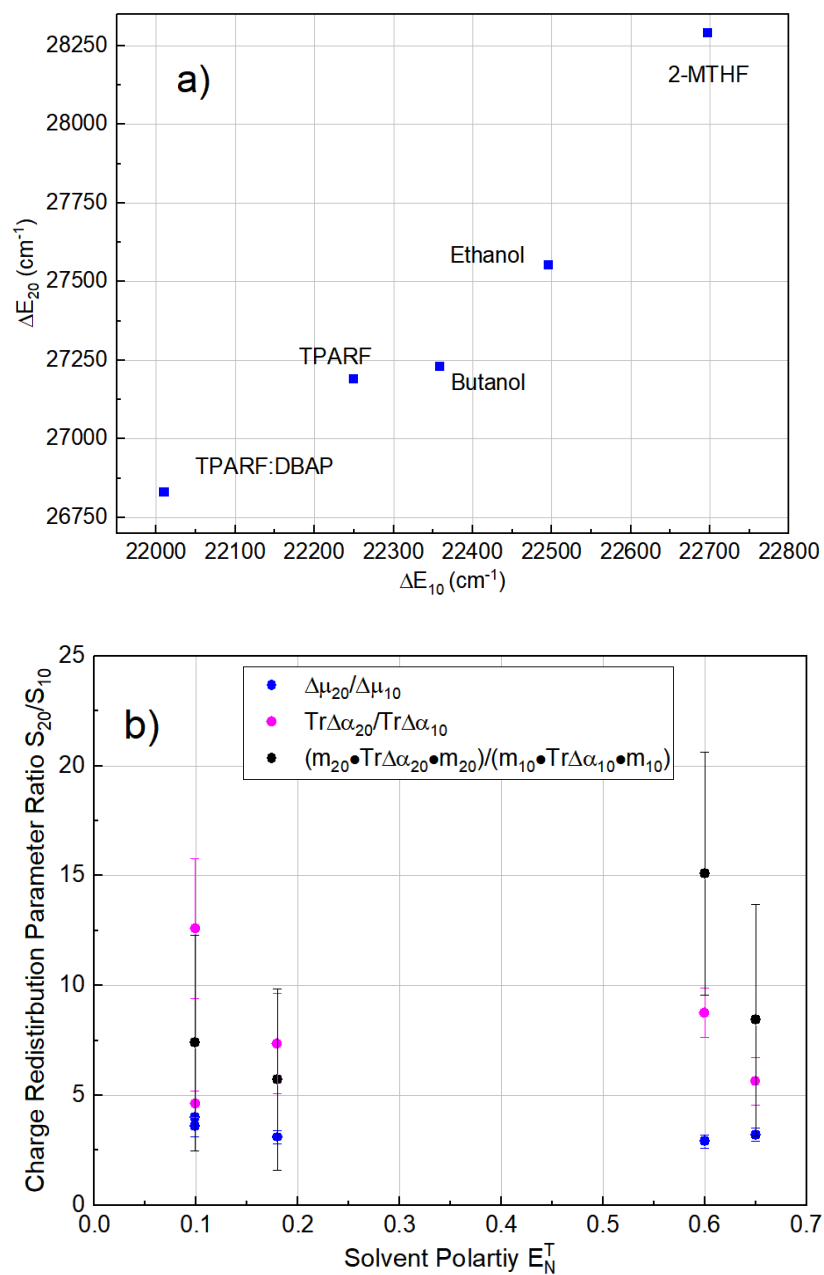


Figure 5.6 Flavin solvatochromism and electrochromism. a) Comparison of S_{10} and S_{20} transition energies for flavin in a variety of solvents. b) Ratio (S_{20}/S_{10}) of electro-optical charge redistribution parameters for flavin in a variety of solvents, plotted against solvent polarity indicator. Uncertainties are estimated via the Monte Carlo analysis discussed in the Methods section.

Table 5.1. Comparison of absorption spectra of TPARF and TPARF:DBAP.

Precision in energy is limited to four significant figures by monochromator wavelength accuracy. Precision in extinction is limited to three significant figures by masses of TPARF and DBAP used. $\bar{\nu}_{MAX}$ is in units of cm^{-1} . ϵ_{MAX} is in units of $\text{M}^{-1}\text{cm}^{-1}$.

Peak	TPARF				TPARF:DBAP			
	298 K		77 K		298 K		77 K	
	$\bar{\nu}_{MAX}$	ϵ_{MAX}	$\bar{\nu}_{MAX}$	ϵ_{MAX}	$\bar{\nu}_{MAX}$	ϵ_{MAX}	$\bar{\nu}_{MAX}$	ϵ_{MAX}
S ₁₀	22470	10400	22250	15700	22420	14800	22010	14756
S ₂₀	29150	6330	27190	6900	28990	8940	26830	11500

Table 5.2. Fit charge redistribution parameters for TPARF and TPARF:DBAP in toluene. Parameters have been corrected for the local field correction factor for the solvent, toluene.

System	Transition	$ \Delta\vec{\mu}_{fi} $ (D)	ζ_A (°)	$Tr\Delta\vec{\alpha}_{fi}$ (\AA^3)	$\vec{m} \cdot \Delta\vec{\alpha}_{fi} \cdot \vec{m}$ (\AA^3)
TPARF	S ₁₀	1.7 ± 0.015	52 ± 21	12 ± 3.1	2.2 ± 1.0
	S ₂₀	6.7 ± 0.018	34 ± 0.14	156 ± 4.9	117 ± 10
TPARF:DBAP	S ₁₀	2.6 ± 0.23	51 ± 9.7	81.9 ± 7.6	29.0 ± 15
	S ₂₀	9.5 ± 1.0	29 ± 12	378 ± 34	214 ± 88

Table 5.3. Theoretical $|\Delta\vec{\mu}_{fi}|$ and ζ_A for Lf and Lf:DFAP implicitly solvated in toluene.

System	Transition	Energy (cm^{-1})	Oscillator Strength	$ \Delta\vec{\mu}_{fi} $ (D)	ζ_A (°)
Lf	S ₁₀	23440	0.2818	1.9665	66.27
	S ₂₀	29290	0.2444	5.7746	11.31
Lf:DFAP	S ₁₀	28150	0.6274	1.7116	64.77
	S ₂₀	35892	0.1718	7.2945	17.11

Table 5.4. Comparison of flavoenzyme experimental charge redistribution parameters. Parameters are for oxidized *E. coli* photolyase and oxidized *S. pastorianus* old yellow enzyme, with and without the p-chlorophenol ligand. The component of the difference polarizability along the transition dipole moment for FAD in photolyase was not reported.

Flavin	Environment	Transition	$\bar{\nu}_{max}$ (cm ⁻¹)	$ \Delta\vec{\mu}_{fi} \cdot f$ (D)	ζ_A (°)	$Tr\Delta\vec{\alpha}_{fi} \cdot f^2$ (Å ³)	$\frac{m \cdot \Delta\vec{\alpha}_{fi} \cdot m \cdot f^2}{m \cdot f^2}$ (Å ³)
FAD	<i>E. coli</i> Photolyase	S ₁₀	22540	2.7 ± 0.3	55 ± 3	134 ± 13	NR
		S ₂₀	26160	7.3 ± 0.5	35 ± 7	57 ± 26	NR
FMN	<i>S. pastorianus</i> Old Yellow Enzyme (No Ligand)	S ₁₀	21290	2.9 ± 0.3	57 ± 1	51 ± 5	23 ± 2
		S ₂₀	25860	7.1 ± 0.7	40 ± 4	198 ± 40	161 ± 32
	<i>S. pastorianus</i> Old Yellow Enzyme (With Ligand)	CT	15330	12 ± 1	0 ± 10	376 ± 75	210 ± 42
		S ₁₀	22500	2.8 ± 0.6	42 ± 8	68 ± 10	26 ± 4
		S ₂₀	26480	8.2 ± 1.6	13 ± 3	376 ± 75	229 ± 46

Table 5.5. Molecular geometry of lumiflavin optimized in implicit toluene solvent. Optimization completed at the B3LYP/6-311+G(2d,p)/PCM level of theory using Gaussian16. A frequency calculation was conducted to verify that the optimized geometry is a minimum on the nuclear geometry potential energy surface. Coordinates are in angstroms.

Atom	X	Y	Z
C	0.00000000	0.00000000	0.00000000
N	0.00000000	0.00000000	1.47120200
C	1.20607100	0.00000000	2.15749900
C	1.17911900	-0.00001500	3.57871300
C	2.39654500	-0.00001800	4.29513500
C	3.62299500	0.00000200	3.65451200
C	3.64365200	0.00002800	2.22644900
C	2.45138600	0.00002600	1.50505200
H	2.50132300	0.00004900	0.42290800
C	4.95679400	0.00006200	1.48513700
H	5.55909600	0.88042300	1.74324100
H	5.55910300	-0.88031500	1.74317300
H	4.80392900	0.00010400	0.40220400
C	4.90633300	0.00000100	4.44940700
H	4.69920100	-0.00003600	5.52335900
H	5.52038800	-0.88160500	4.22549400
H	5.52035400	0.88164500	4.22555000
H	2.33029800	-0.00003200	5.37937400
N	0.00503100	-0.00002000	4.27418100
C	-1.11213400	-0.00001100	3.60521800
C	-1.20192500	0.00001400	2.14874900
N	-2.32329600	0.00006400	1.46349700
C	-3.52493200	0.00006900	2.12944800
N	-3.50770200	0.00008300	3.54298000
C	-2.40093500	-0.00005600	4.36455300
O	-2.48535300	0.00012600	5.58497900
H	-4.41675200	0.00019500	3.99687500
O	-4.61086500	0.00027600	1.55875000
H	0.51066600	0.89457600	-0.36724200
H	-1.03290700	-0.00008000	-0.33695000
H	0.51080900	-0.89449700	-0.36723300

Table 5.6. Molecular geometry of lumiflavin: diformamidopyridine optimized in implicit toluene solvent. Optimization completed at the ω B97/6-311+G(2d,p)/PCM level of theory using Gaussian16. A frequency calculation was conducted to verify that the optimized geometry is a minimum on the nuclear geometry potential energy surface.

Atom	X	Y	Z
C	0.00000000	0.00000000	0.00000000
C	0.00000000	0.00000000	1.50469800
C	1.23599100	0.00000000	2.20936400
C	1.20824900	0.00000100	3.58262000
C	-0.00677100	0.00000000	4.29522800
C	-1.22334300	-0.00000400	3.59567400
C	-1.19951200	-0.00000300	2.19145000
H	-2.12502200	0.00000100	1.62627800
N	-2.41203100	-0.00000800	4.31534400
C	-2.40426200	0.00000500	5.67520500
C	-1.08525400	0.00000900	6.30512000
N	0.03102600	0.00000600	5.66614800
C	-1.05532500	0.00002300	7.80108000
O	-0.02453500	0.00003300	8.45198900
N	-2.28940500	0.00002100	8.37782400
C	-3.51620600	0.00000500	7.69841700
N	-3.53814700	0.00000600	6.33145500
O	-4.53970000	0.00001500	8.37010500
H	-2.33239800	0.00003300	9.40679300
C	-3.68749500	-0.00002600	3.59356100
H	-3.75215200	0.89394400	2.96933600
H	-4.49200000	-0.00005800	4.32337200
H	-3.75210600	-0.89397500	2.96930300
H	2.12603300	0.00000300	4.16541100
C	2.54181700	0.00000200	1.45880800
H	2.62778600	0.88142800	0.81463700
H	2.62776400	-0.88139400	0.81459300
H	3.38717600	-0.00002600	2.15010600
H	0.52310700	-0.88024300	-0.38822400
H	0.52319700	0.88018600	-0.38822700
H	-1.01675900	0.00005000	-0.39815200
H	-6.62155100	0.00006000	10.69875500
C	-5.97849100	0.00005300	11.59625700
N	-4.66027100	0.00005600	11.24828300
H	-4.48290000	0.00004700	10.24124500
C	-3.54139400	0.00007200	12.08992200
C	-3.63558900	0.00009100	13.48155400
C	-2.44729200	0.00010900	14.19533500
C	-1.22131700	0.00011000	13.54736500
C	-1.24064500	0.00009000	12.15341500
N	-2.37191100	0.00007200	11.43775200
N	-0.07590600	0.00008800	11.37392600
H	-0.19840200	0.00007200	10.36108600
C	1.22214100	0.00010900	11.79199900
H	1.91256200	0.00017400	10.93031500
O	1.62110800	0.00019700	12.94065100
H	-0.28076000	0.00012400	14.07960300
H	-2.47702700	0.00012400	15.28195100
H	-4.60389400	0.00009100	13.96161100
O	-6.43911100	0.00008000	12.72206900

Table 5.7. First ten excited states of lumiflavin implicitly solvated in toluene. Excited states calculated at the B3LYP/6-311+G(2d,p)/PCM level of theory using Gaussian16. The difference dipole moment, $|\Delta\vec{\mu}|$, and angle between the difference dipole moment and transition dipole moment, ζ_A , were calculated using the finite field method.

Excited State	Energy (eV)	Wavelength (nm)	Oscillator Strength	$ \Delta\vec{\mu} $ (D)	ζ_A (°)
1	2.9061	426.63	0.2818	1.966555	66.27009
2	3.2938	376.41	0.0007	6.109657	90.053
3	3.3913	365.60	0.0002	4.904213	90.00008
4	3.6315	341.41	0.2444	5.774623	11.3117
5	4.0394	306.93	0.0000	9.426153	100.9051
6	4.1233	300.69	0.0162	9.270433	79.08728
7	4.5574	272.05	0.0768	2.891788	143.6852
8	4.6389	267.27	0.0004	2.647406	90.08261
9	4.7221	262.56	0.8174	0.754002	152.2495
10	5.0457	245.72	0.0444	2.546601	149.1726

Table 5.8. First ten excited states of lumiflavin: diformamidopyridine implicitly solvated in toluene. Excited states calculated at the ω B97/6-311+G(2d,p)/PCM level of theory using Gaussian16. The difference dipole moment, $|\Delta\vec{\mu}|$, and angle between the difference dipole moment and transition dipole moment, ζ_A , were calculated using the finite field method.

Excited State	Energy (eV)	Wavelength (nm)	Oscillator Strength	$ \Delta\vec{\mu} $ (D)	ζ_A (°)
1	3.4901	355.24	0.6274	1.711627	64.27531
2	3.9245	315.92	0.0016	1.199841	91.78455
3	4.45	278.61	0.1718	7.294485	17.11340
4	4.7373	261.72	0.0001	1.073617	89.50158
5	4.7468	261.19	0.3099	6.162212	83.31039
6	5.1192	242.19	0.5782	0.636132	45.77052
7	5.4028	229.48	0.0001	3.162654	90.1693
8	5.4158	228.93	0.0015	3.080663	101.7433
9	5.4196	228.77	0.0475	6.102283	112.4951
10	5.4265	228.48	0.0003	19.96101	42.06359

Table 5.9. Transition energies, ΔE_{10} vs. ΔE_{20} , of flavin in different solvents. All transition energies taken from 77 K absorption spectra.

ΔE_{10} (cm ⁻¹)	ΔE_{20} (cm ⁻¹)
22250	27190
22010	26830
22697	28290
22359	27230
22496	27550

Table 5.10. Solvent dependence of flavin charge redistribution parameters (S_{20}/S_{10}). All transition energies taken from 77 K absorption spectra.

Solvent Polarity	Relative Difference Dipole Moment Magnitude	Estimated Uncertainty in Relative Difference Dipole Moment Magnitude	Relative Difference Trace Polarizability	Estimated Uncertainty in Relative Difference Trace Polarizability	Relative Component of the Difference Polarizability Along the Transition Dipole Moment	Estimated Uncertainty in the Component of the Difference Polarizability Along the Transition Dipole Moment
0.099	4	0.035	12.6	3.2	53.2	8.46
0.099	3.6	0.5	4.6	0.6	7.39	4.91
0.65	3.2	0.3	5.64	1.08	8.43	5.28
0.6	2.9	0.3	8.76	1.13	15.1	5.52
0.18	3.1	0.3	7.36	2.28	5.72	4.12

CHAPTER 6

NEXT STEPS AND FUTURE DIRECTIONS

6.1 Introduction

A major goal of this work is to utilize flavin optical transition energies to measure the magnitude and direction of flavoenzyme active site electric fields directly from the perspective of the reactive flavin cofactor. Different flavin oxidation and protonation states interact with flavoenzyme active site residues uniquely through a given flavoenzyme's catalytic cycle,^{173, 174} meaning that to best understand the role of flavoenzyme active site electric fields in tuning flavin reactivity it is necessary to utilize optical excitations of all catalytically relevant flavin oxidation and protonation states to measure all relevant tuning electric fields. To begin this analysis, however, we will only consider electrostatic tuning of oxidized flavin optical transitions. Most flavin electron-transfer catalysis mechanisms utilize oxidized flavin as an essential intermediate,¹⁷⁵ and, barring significant conformational changes to the flavoenzyme active site as a function of flavin oxidation state, the local field reported by the oxidized flavin should be the operative active site electric field through the flavoenzyme catalytic cycle. This chapter establishes a method for using optical transition energies of oxidized flavin to determine the magnitude and direction of the flavoenzyme active site electric fields, and quantitatively compares field-tuning of flavin cofactors of *E. coli* Photolyase and *S. pastorianus* Old Yellow Enzyme.

6.2 Determining local field magnitude and direction as a function of flavin charge redistribution upon optical excitation and flavin optical transition energies

Charge redistribution upon optical excitation of oxidized flavin is approximately independent of the flavin's local electrostatic environment, meaning that the dependence of oxidized flavin's S_{10} and S_{20} transition energies on the local electric field is given by $\Delta E_{n0} = -\Delta\vec{\mu}_{n0} \cdot \vec{F}$, where ΔE_{n0} is the field-dependent change in excitation energy, $\Delta\vec{\mu}_{n0}$ is the change in permanent dipole moment upon excitation, and \vec{F} is the local electric field. In 1975, Eaton *et al.* measured the polarized absorption spectra of single crystals of flavodoxin,¹⁷⁶ and found that both the S_{10} and S_{20} transition dipole moments of oxidized flavin are in the plane of the isoalloxazine ring system and are approximately parallel to the long axis of the heterocycle. The S_{10} transition dipole moment \vec{m}_{10} deviates $15 \pm 4^\circ$ from the long axis of the flavin, directed from N3 to C8, and that the S_{20} transition dipole moment \vec{m}_{20} deviates $5 \pm 4^\circ$ from the long axis of the flavin, from C2 to C7. Figure 6.1 presents experimentally-determined transition and difference permanent dipole moment unit vectors with respect to the flavin molecular framework. In this work, we have measured the angle between \vec{m}_{10} and $\Delta\vec{\mu}_{10}$ to be $52 \pm 21^\circ$, and the angle between \vec{m}_{20} and $\Delta\vec{\mu}_{20}$ to be $34 \pm 0.14^\circ$, with TD-DFT calculations indicating that for both of these transitions electron density shifts from the xylene ring to the pyrimidine ring of the flavin heterocycle. Combining these two sets of experimentally-determined angles, we can position $\Delta\vec{\mu}_{10}$ at approximately $15^\circ + 52^\circ = 67^\circ$ above the long axis of the flavin directed towards the xylene ring, and $\Delta\vec{\mu}_{20}$ at approximately $34^\circ + (-5^\circ) = 29^\circ$ above the long axis of the flavin, also directed towards the xylene ring.

The in-plane component of the local field \vec{F} interacting with the oxidized flavin S₁₀ and S₂₀ transitions can be written as a sum of projections on any two orthogonal unit vectors \vec{a} and \vec{b} . For simplicity, if we define the unit vector \vec{a} as being parallel to the S₁₀ difference dipole moment $\Delta\vec{\mu}_{10}$, then the magnitude of the component \vec{F}_a will be given by $|\vec{F}_a| = \frac{-\Delta E_{10}}{|\Delta\vec{\mu}_{10}|}$, with its direction along $\Delta\vec{\mu}_{10}$. The magnitude of the orthogonal component of the local field, \vec{F}_b , can then be determined in terms of the projection of the local field on $\Delta\vec{\mu}_{20}$, such that $|\vec{F}_b| = \frac{-\Delta E_{20}}{|\Delta\vec{\mu}_{20}|} \cos(90^\circ - \angle \Delta\vec{\mu}_{10} \Delta\vec{\mu}_{20})$, where the angle between the difference dipole moments is 38°. Determining the angle between the local field and S₁₀ difference permanent dipole moment, and knowing that the angle between $\Delta\vec{\mu}_{10}$ and the component of the long axis of the molecule extending from the center of mass towards the pyrimidine ring is 113°, we can determine the orientation of the local field vector within the flavin molecular frame. Figure 6.2 presents the reference frame for components of the local field determined via this approach.

6.3 Comparison of flavoenzyme active site electric fields of *E. coli* photolyase and *S. pastorianus* old yellow enzyme

The group has previously published high resolution, low temperature absorption spectra of two oxidized flavoenzymes, *E. coli* photolyase¹⁷ (EcPL) and *S. pastorianus* old yellow enzyme (SpOYE).⁸⁸ Taking the magnitudes of the oxidized flavin S₁₀ and S₂₀ difference dipole moments as determined in this work to be $|\Delta\vec{\mu}_{10}| = 1.7 D$ and $|\Delta\vec{\mu}_{20}| = 6.7 D$, and referencing the transition energies of these flavoenzymes to transition energies of oxidized flavin solvated in 2-methyltetrahydrofuran (2-MTHF),¹⁴ the most aliphatic and least perturbing solvent for which low temperature absorption spectra have been

measured, it is possible to evaluate the respective flavoenzyme active site electric fields as described in section 6.2 above. Table 6.1 presents transition energies for flavin in the three relevant environments, as well as the difference in the transition energies for each flavoenzyme relative to flavin in 2-MTHF. Table 6.2 presents the in-plane components of each flavoenzyme's active site electric field parallel and orthogonal to the flavin S_{10} difference permanent dipole moment, as well as the angle made by the local field vector with the long axis of the molecule. Finally, Figure 6.3 presents the flavoenzyme active site electric fields within the flavin molecular frame, and Figure 6.4 presents crystal structures of the PL and OYE active sites showing the molecular origins of the determined fields.^{171, 172}

Both the S_{10} and S_{20} transitions of both photolyase and old yellow enzyme are redshifted relative to flavin in 2-MTHF, with the S_{10} transition energy of OYE approximately 10x more redshifted than that PL. Both transitions involve redistribution of electron density from the xylene to pyrimidine rings, therefore redshifted transition energies indicate stabilization of electron density on the imide moiety via hydrogen bonding, primarily to the C2O and C4O carbonyl oxygens. The C4 carbonyl of flavin in OYE forms hydrogen bonds to two backbone amide hydrogens, as well as one hydrogen bond to a threonine hydroxyl group, whereas the C4 carbonyl of flavin in PL forms only a single hydrogen bond to a backbone amide hydrogen. The C2O carbonyl of flavin in OYE forms a hydrogen bond to a protonated arginine residue, while the C2O of flavin in PL forms hydrogen bonds to two structural water molecules. Furthermore, N5 of the flavin in OYE forms a hydrogen bond to a backbone amide, and the imide moiety of the

flavin cofactor in OYE is bounded by amine groups of asparagine and glutamine residues, as well as a proximal histidine residue. The stronger hydrogen bonding to the arginine group, as well as the placement of additional electropositive residues near to regions of the flavin gaining electron density upon optical excitation from the S_0 to S_1 states causes the component of the flavoenzyme electric field parallel to the S_{10} difference dipole moment to be greater for OYE than PL, and therefore the S_{10} transition energy to be more redshifted for OYE than PL. Also of note is the difference in angle between the OYE and PL electric fields. The PL active site includes a coplanar arginine residue near to the flavin N5 and C4a atoms, as well as an asparagine residue that may hydrogen bond to N5.¹⁷⁷ These residues act to rotate the orientation of the PL active site electric field towards N5 relative to OYE, as is evident in Figure 6.3.

This preliminary analysis demonstrates the application of Stark spectroscopy to measure flavoenzyme active site electric field magnitudes and directions from the perspective of the flavin cofactor, improving our understanding of electrostatic tuning of flavin reactivity. Work is ongoing to extend this analysis to a wider repertoire of flavoenzymes, and to connect specific field magnitudes and directions to changes in flavoenzyme reduction potential.

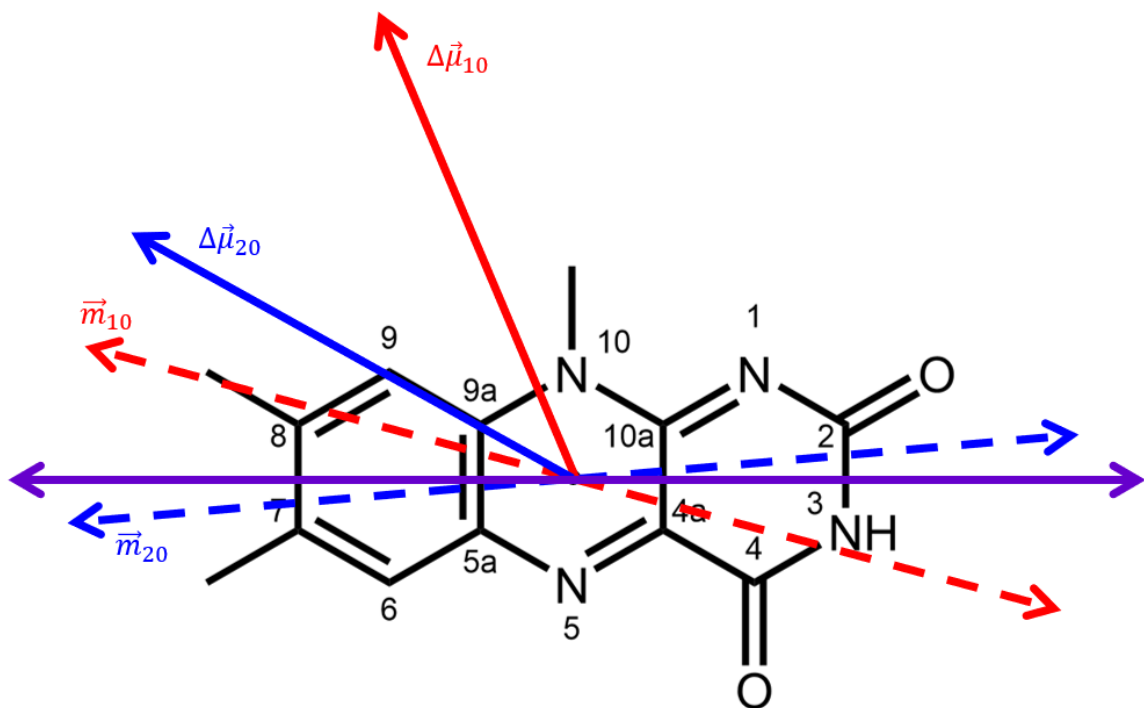


Figure 6.1. Experimental transition and difference permanent dipole moments in flavin molecular frame. All vectors are normalized in magnitude. The purple axis indicates the long axis of the molecule. Transition dipole moments taken from Eaton *et al.*¹⁷⁶ Difference permanent dipole moments taken from this work.

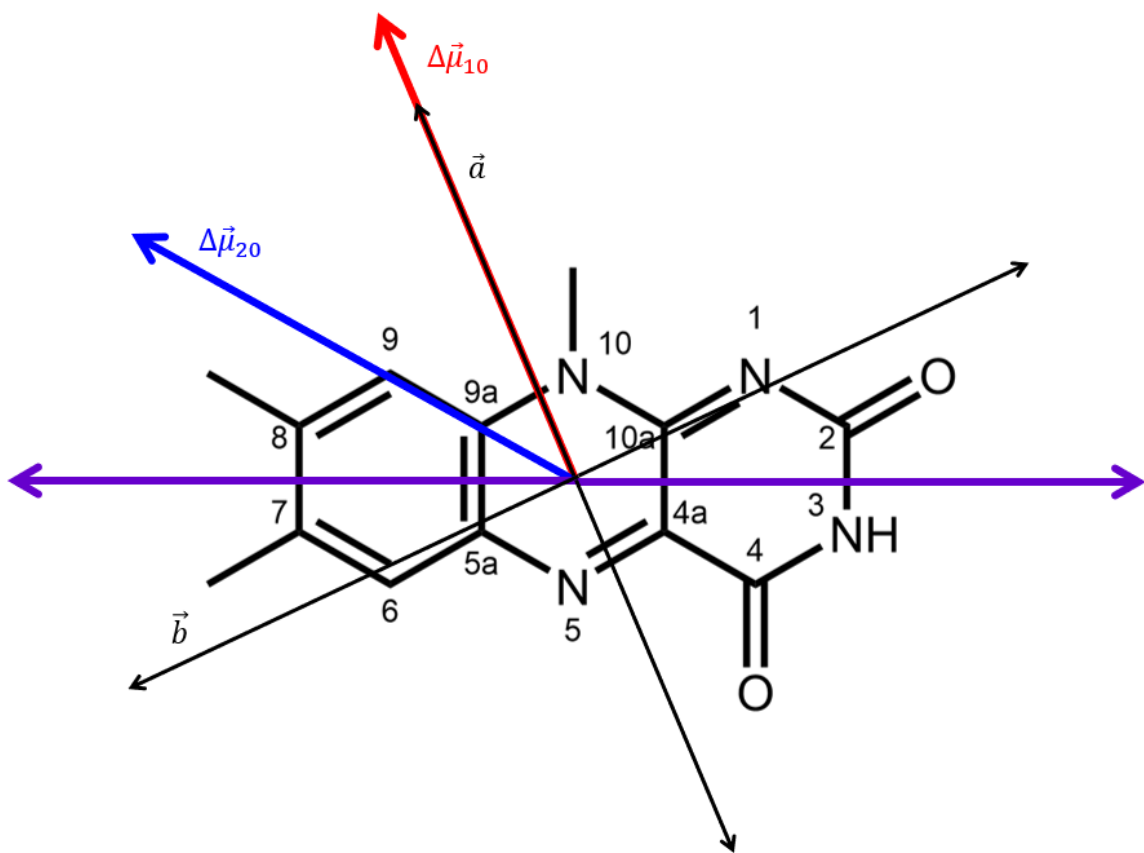


Figure 6.2. Reference frame for determination of local field orthogonal components.

Table 6.1. Flavoenzyme S_{10} and S_{20} transition energies relative to flavin in 2-MTHF. Relative transition energies are determined by subtracting the 2-MTHF transition energy from the flavoenzyme transition energy.

Flavin Environment	$E_{10}(cm^{-1})$	$E_{20}(cm^{-1})$	$\Delta E_{10}(cm^{-1})$	$\Delta E_{20}(cm^{-1})$
2-MTHF	22669	29607		
EcPL	22522	27449	-147	-2158
SpOYE	21259	26625	-1410	-2982

Table 6.2. Flavoenzyme active site electric field components relative to $\Delta\vec{\mu}_{10}$ and angle relative to flavin long axis.

Flavoenzyme	\vec{F}_{\parallel} (MV/cm)	\vec{F}_{\perp} (MV/cm)	Angle relative to flavin long axis
EcPL	5.155	11.81	179.4
SpOYE	49.40	16.31	131.2

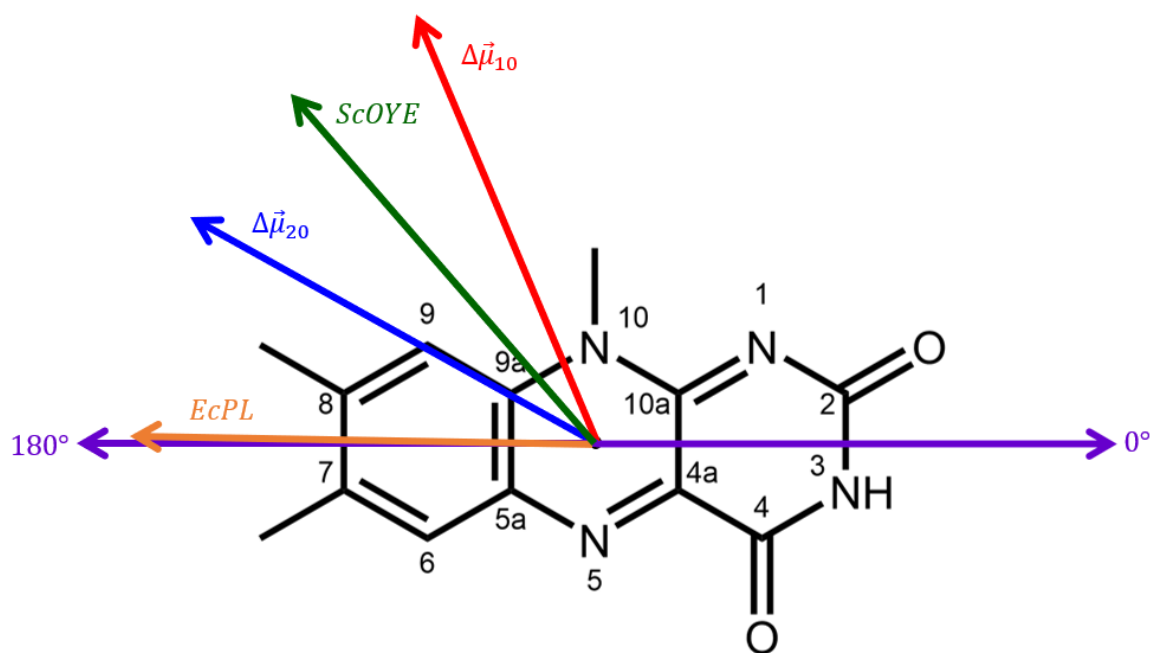


Figure 6.3. Orientation of flavoenzyme electric field unit vectors in the molecular frame.

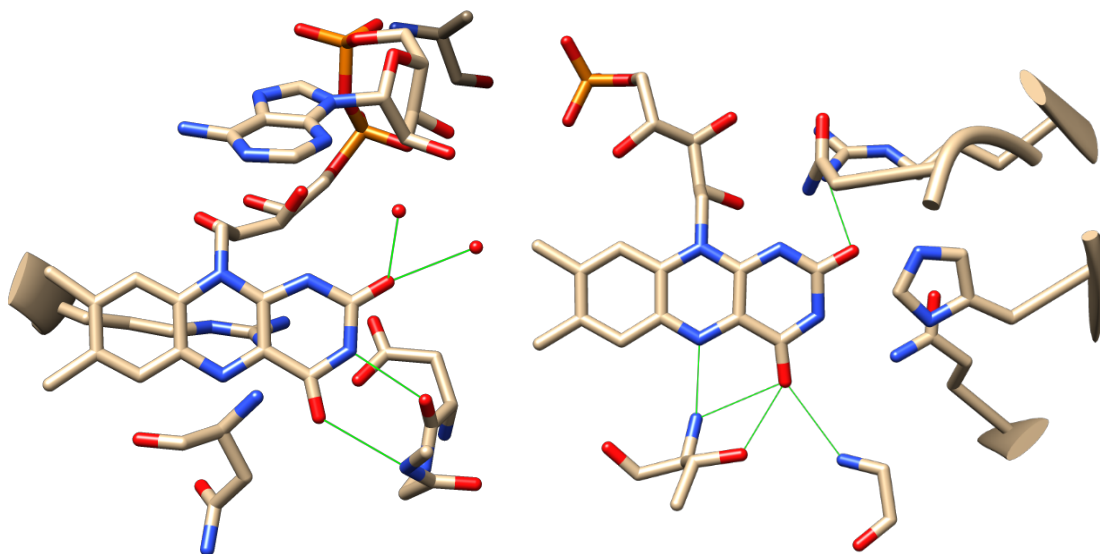


Figure 6.4. Crystal structures of PL (L) and OYE (R) active sites. Images rendered using UCSF Chimera, version 1.14.¹⁷⁸ Hydrogen bonds given by green lines.

CHAPTER 7

CONCLUDING REMARKS

In conclusion, in this dissertation I have presented applications of electroabsorption spectroscopy to enzymology and molecular electronics. First, I have utilized electroabsorption spectroscopy to estimate the second-harmonic generation cross-section of lumichrome, a photodegradation product of flavin cofactors which may have application to stand-off detection of bacterial quorum sensing, determining that the second-harmonic generation cross-section of lumichrome is similar to that of flavin. Second, I determined that the electro-optical band gap of perylene diimide is unlikely to be tuned by electric fields within molecular electronic devices due to the centrosymmetry of the chromophore. Finally, I demonstrated that the charge redistribution upon optical excitation of flavin is independent of solvent polarity, indicating that the excitation energies of oxidized flavin may serve as consistent probes of flavoenzyme active site electric fields. I further demonstrated utility of these transitions as such probes for comparing the active site electric fields of the flavoenzymes *E. coli* photolyase and *S. pastorianus* old yellow enzyme.

REFERENCES CITED

- (1) Cantor, C. R.; Schimmel, P. R. *Biophysical Chemistry*; W.H. Freeman and Company, 1980.
- (2) Liu, B.; Rocca, D.; Yan, H.; Pan, D. Beyond Conformational Control: Effects of Noncovalent Interactions on Molecular Electronic Properties of Conjugated Polymers. *Jacs Au* **2021**, *1* (12), 2182-2187, Article. DOI: 10.1021/jacsau.1c00284.
- (3) Sautter, A.; Thalacker, C.; Heise, B.; Wurthner, F. Hydrogen bond-directed aggregation of diazadibenzoperylene dyes in low-polarity solvents and the solid state. *Proceedings of the National Academy of Sciences of the United States of America* **2002**, *99* (8), 4993-4996, Article. DOI: 10.1073/pnas.062606099.
- (4) Lugger, S. J. D.; Houben, S. J. A.; Foelen, Y.; Debije, M. G.; Schenning, A.; Mulder, D. J. Hydrogen-Bonded Supramolecular Liquid Crystal Polymers: Smart Materials with Stimuli-Responsive, Self-Healing, and Recyclable Properties. *Chemical Reviews* **2022**, *122* (5), 4946-4975. DOI: 10.1021/acs.chemrev.1c00330.
- (5) Yoder, C. H. Teaching Ion-Ion, Ion-Dipole, And Dipole-Dipole Interactions. *Journal of Chemical Education* **1977**, *54* (7), 402-408. DOI: 10.1021/ed054p402.
- (6) Fried, S. D.; Boxer, S. G. Measuring Electric Fields and Noncovalent Interactions Using the Vibrational Stark Effect. *Accounts of Chemical Research* **2015**, *48* (4), 998-1006. DOI: 10.1021/ar500464j.
- (7) Boxer, S. G. Stark Realities. *Journal of Physical Chemistry B* **2009**, *113* (10), 2972-2983, Review. DOI: 10.1021/jp8067393.
- (8) Liptay, W. Electrochromism and Solvatochromism. *Angewandte Chemie-International Edition* **1969**, *8* (3), 177-&, Article. DOI: 10.1002/anie.196901771.
- (9) Stark, J. Observation of the separation of spectral lines by an electric field. *Nature* **1914**, *92*, 401-401, Letter.
- (10) R.S.W. An electrical analogy of the Zeeman effect. *Nature* **1914**, *93*, 280-280, Article.
- (11) Liptay, W. Dipole Moments and Polarizabilities of Molecules in Excited Electronic States. In *Excited States*, Lim, E. C. Ed.; Vol. 1; Academic Press, Inc., 1974; pp 129-229.
- (12) Bublitz, G. U.; Boxer, S. G. Stark spectroscopy: Applications in chemistry, biology, and materials science. *Annual Review of Physical Chemistry* **1997**, *48*, 213-242, Review. DOI: 10.1146/annurev.physchem.48.1.213.

- (13) Stanley, R. J.; van Galen, C. J. Measuring electronic structure properties of flavins and flavoproteins by electronic Stark spectroscopy. In *Methods in Enzymology*, Palfey, B. A. Ed.; New Approaches for Flavoenzyme Catalysis, Vol. 620; Elsevier, 2019; pp 215-250.
- (14) Stanley, R. J.; Siddiqui, M. S. A stark spectroscopic study of N(3)-methyl, N(10)-isobutyl-7,8-dimethylisalloxazine in nonpolar low-temperature glasses: Experiment and comparison with calculations. *Journal of Physical Chemistry A* **2001**, *105* (49), 11001-11008, Article. DOI: 10.1021/jp011971j.
- (15) Pauszek, R. F.; Kodali, G.; Caldwell, S. T.; Fitzpatrick, B.; Zainalabdeen, N. Y.; Cooke, G.; Rotello, V. M.; Stanley, R. J. Excited State Charge Redistribution and Dynamics in the Donor-pi-Acceptor Flavin Derivative ABFL. *Journal of Physical Chemistry B* **2013**, *117* (49), 15684-15694, Article. DOI: 10.1021/jp406420h.
- (16) van Galen, C.; Barnard, D. T.; Stanley, R. J. Stark Spectroscopy of Lumichrome: A Possible Candidate for Stand-Off Detection of Bacterial Quorum Sensing. *Journal of Physical Chemistry B* **2020**, *124* (52), 11835-11842, Article. DOI: 10.1021/acs.jpcc.0c09498.
- (17) Kodali, G.; Siddiqui, S. U.; Stanley, R. J. Charge Redistribution in Oxidized and Semiquinone E. coli DNA Photolyase upon Photoexcitation: Stark Spectroscopy Reveals a Rationale for the Position of Trp382. *Journal of the American Chemical Society* **2009**, *131* (13), 4795-4807, Review. DOI: 10.1021/ja809214r.
- (18) Pauszek, R. F.; Kodali, G.; Siddiqui, M. S. U.; Stanley, R. J. Overlapping Electronic States with Nearly Parallel Transition Dipole Moments in Reduced Anionic Flavin Can Distort Photobiological Dynamics. *Journal of the American Chemical Society* **2016**, *138* (45), 14880-14889, Article. DOI: 10.1021/jacs.6b06449.
- (19) Hopkins, N.; Stanley, R. J. Measurement of the Electronic Properties of the Flavoprotein Old Yellow Enzyme (OYE) and the OYE:p-Cl Phenol Charge-Transfer Complex Using Stark Spectroscopy. *Biochemistry* **2003**, *42* (4), 991-999.
- (20) Kodali, G.; Kistler, K. A.; Matsika, S.; Stanley, R. J. 2-aminopurine excited state electronic structure measured by stark spectroscopy. *Journal of Physical Chemistry B* **2008**, *112* (6), 1789-1795, Article. DOI: 10.1021/jp076374x.
- (21) Kodali, G.; Kistler, K. A.; Narayanan, M.; Matsika, S.; Stanley, R. J. Change in Electronic Structure upon Optical Excitation of 8-Vinyladenosine: An Experimental and Theoretical Study. *Journal of Physical Chemistry A* **2010**, *114* (1), 256-267, Article. DOI: 10.1021/jp908055h.

- (22) Kodali, G.; Narayanan, M.; Stanley, R. J. Excited-State Electronic Properties of 6-Methylisoxanthopterin (6-MI): An Experimental and Theoretical Study. *Journal of Physical Chemistry B* **2012**, *116* (9), 2981-2989, Article. DOI: 10.1021/jp2110083.
- (23) Van Galen, C. J.; Pauszek, R. F.; Koder, R. L.; Stanley, R. J. Flavin Charge Redistribution upon Optical Excitation Is Independent of Solvent Polarity. *Journal of Physical Chemistry B* **2023**, 661-672, Article; Early Access. DOI: 10.1021/acs.jpccb.2c07266661J.
- (24) Bacher, A.; Eberhardt, S.; Fischer, M.; Mortl, S.; Kis, K.; Kugelbrey, K.; Scheuring, J.; Schott, K. Biosynthesis of riboflavin: Lumazine synthase and riboflavin synthase. In *Vitamins and Coenzymes, Pt J*, McCormick, D. B., Suttie, J. W., Wagner, C. Eds.; Methods in Enzymology, Vol. 280; 1997; pp 389-399.
- (25) Abbas, C. A.; Sibirny, A. A. Genetic Control of Biosynthesis and Transport of Riboflavin and Flavin Nucleotides and Construction of Robust Biotechnological Producers. *Microbiology and Molecular Biology Reviews* **2011**, *75* (2), 321-+. DOI: 10.1128/mnbr.00030-10.
- (26) Holzer, W.; Shirdel, J.; Zirak, P.; Penzkofer, A.; Hegemann, P.; Deutzmann, R.; Hochmuth, E. Photo-induced degradation of some flavins in aqueous solution. *Chemical Physics* **2005**, *308* (1-2), 69-78, Article. DOI: 10.1016/j.chemphys.2004.08.006.
- (27) Xu, H.; Chakrabarty, Y.; Philmus, B.; Mehta, A. P.; Bhandari, D.; Hohmann, H. P.; Begley, T. P. Identification of the First Riboflavin Catabolic Gene Cluster Isolated from *Microbacterium maritopicum* G10. *Journal of Biological Chemistry* **2016**, *291* (45), 23506-23515. DOI: 10.1074/jbc.M116.729871.
- (28) Losi, A. Flavin-based blue-light photosensors: a photobiophysics update. *Photochemistry and Photobiology* **2007**, *83* (6), 1283-1300.
- (29) Macheroux, P.; Kappes, B.; Ealick, S. E. Flavogenomics - a genomic and structural view of flavin-dependent proteins. *Febs Journal* **2011**, *278* (15), 2625-2634. DOI: 10.1111/j.1742-4658.2011.08202.x.
- (30) Hong, J.; Lee, M.; Lee, B.; Seo, D. H.; Park, C. B.; Kang, K. Biologically inspired pteridine redox centres for rechargeable batteries. *Nature Communications* **2014**, *5*. DOI: 10.1038/ncomms6335.
- (31) Nelson, D. L.; Cox, M. M. *Lehninger Principles of Biochemistry*; w.h. freeman, 2017.
- (32) Song, S. H.; Dick, B.; Penzkofer, A. Photo-induced reduction of flavin mononucleotide in aqueous solutions. *Chemical Physics* **2007**, *332* (1), 55-65. DOI: 10.1016/j.chemphys.2006.11.023.

- (33) Giancaspero, T. A.; Busco, G.; Panebianco, C.; Carmone, C.; Miccolis, A.; Liuzzi, G. M.; Colella, M.; Barile, M. FAD Synthesis and Degradation in the Nucleus Create a Local Flavin Cofactor Pool. *Journal of Biological Chemistry* **2013**, *288* (40), 29069-29080. DOI: 10.1074/jbc.M113.500066.
- (34) Maruta, T.; Yoshimoto, T.; Ito, D.; Ogawa, T.; Tamoi, M.; Yoshimura, K.; Shigeoka, S. An Arabidopsis FAD Pyrophosphohydrolase, AtNUDX23, is Involved in Flavin Homeostasis. *Plant and Cell Physiology* **2012**, *53* (6), 1106-1116. DOI: 10.1093/pcp/pcs054.
- (35) Foster, J. W. Microbiological aspects of riboflavin I introduction II Bacterial oxidation of riboflavin to lumichrome. *Journal of Bacteriology* **1944**, *47* (1), 27-41. DOI: 10.1128/jb.47.1.27-41.1944.
- (36) Kubo, Y.; Yahata, S.; Miki, S.; Akanuma, S.; Hosoya, K. Blood-to-retina transport of riboflavin via RFVTs at the inner blood-retinal barrier. *Drug Metabolism and Pharmacokinetics* **2017**, *32* (1), 92-99. DOI: 10.1016/j.dmpk.2016.09.006.
- (37) Kansara, V.; Pal, D.; Jain, R.; Mitra, A. K. Identification and functional characterization of riboflavin transporter in human-derived retinoblastoma cell line (Y-79): Mechanisms of cellular uptake and translocation. *Journal of Ocular Pharmacology and Therapeutics* **2005**, *21* (4), 275-287. DOI: 10.1089/jop.2005.21.275.
- (38) Said, H. M.; Wang, S. L.; Ma, T. Y. Mechanism of riboflavin uptake by cultured human retinal pigment epithelial ARPE-19 cells: possible regulation by an intracellular Ca²⁺-calmodulin-mediated pathway. *Journal of Physiology-London* **2005**, *566* (2), 369-377. DOI: 10.1113/jphysiol.2005.085811.
- (39) Kelley, R. A.; Al-Ubaidi, M. R.; Sinha, T.; Genc, A. M.; Makia, M. S.; Ikelle, L.; Naash, M. I. Ablation of the riboflavin-binding protein retbindin reduces flavin levels and leads to progressive and dose-dependent degeneration of rods and cones. *J. Biol. Chem.* **2017**, *292* (51), 21023-21034. DOI: 10.1074/jbc.M117.785105.
- (40) Kelley, R. A.; Al-Ubaidi, M. R.; Naash, M. I. Retbindin Is an Extracellular Riboflavin-binding Protein Found at the Photoreceptor/Retinal Pigment Epithelium Interface. *Journal of Biological Chemistry* **2015**, *290* (8), 5041-5052. DOI: 10.1074/jbc.M114.624189.
- (41) Kubo, Y.; Akanuma, S.; Hosoya, K. Recent advances in drug and nutrient transport across the blood-retinal barrier. *Expert Opinion on Drug Metabolism & Toxicology* **2018**, *14* (5), 513-531. DOI: 10.1080/17425255.2018.1472764.
- (42) D'Amico Donald, J.; Masonson, H. N.; Patel, M.; Adamis, A. P.; Cunningham, E. T., Jr.; Guyer, D. R.; Katz, B. Pegaptanib sodium for neovascular age-related macular

degeneration: two-year safety results of the two prospective, multicenter, controlled clinical trials. *Ophthalmology* **2006**, *113* (6), 992-1001 e1006.

(43) Grininger, M.; Zeth, K.; Oesterhelt, D. Dodecins: A family of lumichrome binding proteins. *Journal of Molecular Biology* **2006**, *357* (3), 842-857. DOI: 10.1016/j.jmb.2005.12.072.

(44) Jaadane, I.; Rodriguez, G. E. V.; Boulenguez, P.; Chahory, S.; Carre, S.; Savoldelli, M.; Jonet, L.; Behar-Cohen, F.; Martinsons, C.; Torriglia, A. Effects of white light-emitting diode (LED) exposure on retinal pigment epithelium in vivo. *Journal of Cellular and Molecular Medicine* **2017**, *21* (12), 3453-3466. DOI: 10.1111/jcmm.13255.

(45) Bonmati-Carrion, M. A.; Arguelles-Prieto, R.; Martinez-Madrid, M. J.; Reiter, R.; Hardeland, R.; Rol, M. A.; Madrid, J. A. Protecting the Melatonin Rhythm through Circadian Healthy Light Exposure. *International Journal of Molecular Sciences* **2014**, *15* (12), 23448-23500. DOI: 10.3390/ijms151223448.

(46) Stephenson, K. M.; Schroder, C. M.; Bertschy, G.; Bourgin, P. Complex interaction of circadian and non-circadian effects of light on mood: Shedding new light on an old story. *Sleep Medicine Reviews* **2012**, *16* (5), 445-454. DOI: 10.1016/j.smrv.2011.09.002.

(47) Kennis, J. T. M.; Crosson, S.; Gauden, M.; van Stokkum, I. H. M.; Moffat, K.; van Grondelle, R. Primary Reactions of the LOV2 Domain of Phototropin, a Plant Blue-Light Photoreceptor. *Biochemistry* **2003**, *42* (12), 3385-3392.

(48) Swartz, T. E.; Corchnoy, S. B.; Christie, J. M.; Lewis, J. W.; Szundi, I.; Briggs, W. R.; Bogomolni, R. A. The photocycle of a flavin-binding domain of the blue light photoreceptor phototropin. *Journal of Biological Chemistry* **2001**, *276* (39), 36493-36500. DOI: 10.1074/jbc.M103114200.

(49) Torra, J.; Lafaye, C.; Signor, L.; Aumonier, S.; Flors, C.; Shu, X. K.; Nonell, S.; Gotthard, G.; Royant, A. Tailing miniSOG: structural bases of the complex photophysics of a flavin-binding singlet oxygen photosensitizing protein. *Scientific Reports* **2019**, *9*. DOI: 10.1038/s41598-019-38955-3.

(50) Dakora, F. D.; Matiru, V. N.; Kanu, A. Rhizosphere ecology of lumichrome and riboflavin, two bacterial signal molecules eliciting developmental changes in plants. *Frontiers in Plant Science* **2015**, *6*. DOI: 10.3389/fpls.2015.00700.

(51) Mattmann, M. E.; Blackwell, H. E. Small Molecules That Modulate Quorum Sensing and Control Virulence in *Pseudomonas aeruginosa*. *Journal of Organic Chemistry* **2010**, *75* (20), 6737-6746. DOI: 10.1021/jo101237e.

(52) Rajamani, S.; Bauer, W. D.; Robinson, J. B.; Farrow, J. M.; Pesci, E. C.; Teplitzki, M.; Gao, M. S.; Sayre, R. T.; Phillips, D. A. The Vitamin Riboflavin and Its Derivative

Lumichrome Activate the LasR Bacterial Quorum-Sensing Receptor. *Molecular Plant-Microbe Interactions* **2008**, *21* (9), 1184-1192. DOI: 10.1094/mpmi-21-9-1184.

(53) Cooper, J. E. Early interactions between legumes and rhizobia: disclosing complexity in a molecular dialogue. *Journal of Applied Microbiology* **2007**, *103* (5), 1355-1365. DOI: 10.1111/j.1365-2672.2007.03366.x.

(54) Moyon, N. S.; Mitra, S. Fluorescence Solvatochromism in Lumichrome and Excited-State Tautomerization: A Combined Experimental and DFT Study. *Journal of Physical Chemistry A* **2011**, *115* (12), 2456-2464. DOI: 10.1021/jp1102687.

(55) Gh, M. S.; Wilhelm, M. J.; Moore, M.; Dai, H. L. Spatially Resolved Membrane Transport in a Single Cell Imaged by Second Harmonic Light Scattering. *Biochemistry* **2019**, *58* (14), 1841-1844. DOI: 10.1021/acs.biochem.9b00110.

(56) Sharifian, G. H. M.; Wilhelm, M. J.; Dai, H. L. Azithromycin-Induced Changes to Bacterial Membrane Properties Monitored in Vitro by Second-Harmonic Light Scattering. *Acs Medicinal Chemistry Letters* **2018**, *9* (6), 569-574. DOI: 10.1021/acsmchemlett.7b00499.

(57) Reeve, J. E.; Anderson, H. L.; Clays, K. Dyes for biological second harmonic generation imaging. *Physical Chemistry Chemical Physics* **2010**, *12* (41), 13484-13498. DOI: 10.1039/c003720f.

(58) Shcherbatska, N. V.; van Hoek, A.; Visser, A. J. W. G.; Koziol, J. Molecular Relaxation spectroscopy of lumichrome. *Journal of Photochemistry and Photobiology A: Chem.* **1994**, *78*, 241-246.

(59) Macedo, A. G.; Christopholi, L. P.; Gavim, A. E. X.; de Deus, J. F.; Teridi, M. A. M.; Yusoff, A. B.; da Silva, W. J. Perylene derivatives for solar cells and energy harvesting: a review of materials, challenges and advances. *Journal of Materials Science-Materials in Electronics* **2019**, *30* (17), 15803-15824, Review. DOI: 10.1007/s10854-019-02019-z.

(60) Kozma, E.; Mroz, W.; Villafiorita-Monteleone, F.; Galeotti, F.; Andicsova-Eckstein, A.; Catellani, M.; Botta, C. Perylene diimide derivatives as red and deep red-emitters for fully solution processable OLEDs. *Rsc Advances* **2016**, *6* (66), 61175-61179, Article. DOI: 10.1039/c6ra10467c.

(61) Lamport, Z. A.; Haneef, H. F.; Anand, S.; Waldrip, M.; Jurchescu, O. D. Tutorial: Organic field-effect transistors: Materials, structure and operation. *Journal of Applied Physics* **2018**, *124* (7). DOI: 10.1063/1.5042255.

- (62) Yang, Z.; Chen, X. Y. Semiconducting Perylene Diimide Nanostructure: Multifunctional Phototheranostic Nanoplatform. *Accounts of Chemical Research* **2019**, *52* (5), 1245-1254, Review. DOI: 10.1021/acs.accounts.9b00064.
- (63) Guo, X. G.; Facchetti, A.; Marks, T. J. Imide- and Amide-Functionalized Polymer Semiconductors. *Chemical Reviews* **2014**, *114* (18), 8943-9021, Review. DOI: 10.1021/cr500225d.
- (64) Huang, C.; Barlow, S.; Marder, S. R. Perylene-3,4,9,10-tetracarboxylic Acid Diimides: Synthesis, Physical Properties, and Use in Organic Electronics. *Journal of Organic Chemistry* **2011**, *76* (8), 2386-2407, Article. DOI: 10.1021/jo2001963.
- (65) Clark, A. E.; Qin, C. Y.; Li, A. D. Q. Beyond exciton theory: A time-dependent DFT and Franck-Condon study of perylene diimide and its chromophoric dimer. *Journal of the American Chemical Society* **2007**, *129* (24), 7586-7595, Article. DOI: 10.1021/ja0687724.
- (66) Ghosh, S.; Li, X. Q.; Stepanenko, V.; Wurthner, F. Control of H- and J-Type pi Stacking by Peripheral Alkyl Chains and Self-Sorting Phenomena in Perylene Bisimide Homo- and Heteroaggregates. *Chemistry-a European Journal* **2008**, *14* (36), 11343-11357, Review. DOI: 10.1002/chem.200801454.
- (67) Oleson, A.; Zhu, T.; Dunn, I. S.; Bialas, D.; Bai, Y.; Zhang, W. Q.; Dai, M. J.; Reichman, D. R.; Tempelaar, R.; Huang, L. B.; et al. Perylene Diimide-Based H_j- and h_J-Aggregates: The Prospect of Exciton Band Shape Engineering in Organic Materials. *Journal of Physical Chemistry C* **2019**, *123* (33), 20567-20578, Article. DOI: 10.1021/acs.jpcc.9b04429.
- (68) Gregg, B. A.; Chen, S. G.; Branz, H. M. On the superlinear increase in conductivity with dopant concentration in excitonic semiconductors. *Applied Physics Letters* **2004**, *84* (10), 1707-1709, Article. DOI: 10.1063/1.1668326.
- (69) Schwarze, M.; Tress, W.; Beyer, B.; Gao, F.; Scholz, R.; Poelking, C.; Ortstein, K.; Gunther, A. A.; Kasemann, D.; Andrienko, D.; et al. Band structure engineering in organic semiconductors. *Science* **2016**, *352* (6292), 1446-1449, Article. DOI: 10.1126/science.aaf0590.
- (70) Coropceanu, V.; Li, H.; Winget, P.; Zhu, L. Y.; Bredas, J. L. Electronic-Structure Theory of Organic Semiconductors: Charge-Transport Parameters and Metal/Organic Interfaces. In *Annual Review of Materials Research, Vol 43*, Clarke, D. R. Ed.; Annual Review of Materials Research, Vol. 43; Annual Reviews, 2013; pp 63-87.
- (71) Lungenschmied, C.; Dennler, G.; Neugebauer, H.; Sariciftci, N. S.; Ehrenfreund, E. Internal electric field in organic-semiconductor-based photovoltaic devices. *Applied Physics Letters* **2006**, *89* (22), 3, Article. DOI: 10.1063/1.2398898.

- (72) Tutis, E.; Berner, D.; Zuppiroli, L. Internal electric field and charge distribution in multilayer organic light-emitting diodes. *Journal of Applied Physics* **2003**, *93* (8), 4594-4602, Article. DOI: 10.1063/1.1558208.
- (73) Weis, M.; Manaka, T.; Iwamoto, M. Origin of electric field distribution in organic field-effect transistor: Experiment and analysis. *Journal of Applied Physics* **2009**, *105* (2), 7, Article. DOI: 10.1063/1.3062601.
- (74) Manaka, T.; Lim, E.; Tamura, R.; Yamada, D.; Iwamoto, M. Probing of the electric field distribution in organic field effect transistor channel by microscopic second-harmonic generation. *Applied Physics Letters* **2006**, *89* (7), 3, Article. DOI: 10.1063/1.2335370.
- (75) Bafekry, A.; Stampfl, C. Band-gap control of graphenelike borocarbonitride g-BC₆N bilayers by electrical gating. *Physical Review B* **2020**, *102* (19), 6, Article. DOI: 10.1103/PhysRevB.102.195411.
- (76) Avetisyan, A. A.; Partoens, B.; Peeters, F. M. Electric field tuning of the band gap in graphene multilayers. *Physical Review B* **2009**, *79* (3), 7, Article. DOI: 10.1103/PhysRevB.79.035421.
- (77) Wickenburg, S.; Lu, J.; Lischner, J.; Tsai, H. Z.; Omrani, A. A.; Riss, A.; Karrasch, C.; Bradley, A.; Jung, H. S.; Khajeh, R.; et al. Tuning charge and correlation effects for a single molecule on a graphene device. *Nature Communications* **2016**, *7*, 7, Article. DOI: 10.1038/ncomms13553.
- (78) Peng, L. L.; Chen, F.; Hong, Z. W.; Zheng, J. F.; Fillaud, L.; Yuan, Y.; Huang, M. L.; Shao, Y.; Zhou, X. S.; Chen, J. Z.; et al. Precise tuning of single molecule conductance in an electrochemical environment. *Nanoscale* **2018**, *10* (15), 7026-7032, Article. DOI: 10.1039/c8nr00625c.
- (79) Tsutsui, M.; Taniguchi, M. Single Molecule Electronics and Devices. *Sensors* **2012**, *12* (6), 7259-7298, Review. DOI: 10.3390/s120607259.
- (80) Kaminski, W.; Topolnicki, R.; Hapala, P.; Jelinek, P.; Kucharczyk, R. Tuning the conductance of benzene-based single-molecule junctions. *Organic Electronics* **2016**, *34*, 254-261, Article. DOI: 10.1016/j.orgel.2016.04.035.
- (81) Li, Y.; Doak, P.; Kronik, L.; Neaton, J. B.; Natelson, D. Voltage tuning of vibrational mode energies in single-molecule junctions. *Proceedings of the National Academy of Sciences of the United States of America* **2014**, *111* (4), 1282-1287, Article. DOI: 10.1073/pnas.1320210111.
- (82) Sun, L.; Diaz-Fernandez, Y. A.; Gschneidner, T. A.; Westerlund, F.; Lara-Avila, S.; Moth-Poulsen, K. Single-molecule electronics: from chemical design to functional

devices. *Chemical Society Reviews* **2014**, *43* (21), 7378-7411, Review. DOI: 10.1039/c4cs00143e.

(83) Tang, C.; Zheng, J. T.; Ye, Y. L.; Liu, J. Y.; Chen, L. J.; Yan, Z. W.; Chen, Z. X.; Chen, L. C.; Huang, X. Y.; Bai, J.; et al. Electric-Field-Induced Connectivity Switching in Single-Molecule Junctions. *Isience* **2020**, *23* (1), 29, Article. DOI: 10.1016/j.isci.2019.100770.

(84) Batra, A.; Darancet, P.; Chen, Q. S.; Meisner, J. S.; Widawsky, J. R.; Neaton, J. B.; Nuckolls, C.; Venkataraman, L. Tuning Rectification in Single-Molecular Diodes. *Nano Letters* **2013**, *13* (12), 6233-6237, Article. DOI: 10.1021/nl403698m.

(85) Ara, A. M.; Ahmed, M. K. Stark absorption study of perylene doped in a poly (methyl methacrylate) polymer film at different concentrations. *Journal of Bangladesh Academy of Sciences* **2019**, *43* (2), 133-139.

(86) Ara, A. M.; Iimori, T.; Yoshizawa, T.; Nakabayashi, T.; Ohta, N. External electric field effects on fluorescence of perylene doped in a polymer film. *Chemical Physics Letters* **2006**, *427* (4-6), 322-328, Article. DOI: 10.1016/j.cplett.2006.07.001.

(87) Ito, F.; Kogasaka, Y.; Yamamoto, K. Fluorescence Spectral Changes of Perylene in Polymer Matrices during the Solvent Evaporation Process. *Journal of Physical Chemistry B* **2013**, *117* (13), 3675-3681, Article. DOI: 10.1021/jp401002y.

(88) Hopkins, N.; Stanley, R. J. Measurement of the electronic properties of the flavoprotein old yellow enzyme (OYE) and the OYE : p-Cl phenol charge-transfer complex using stark spectroscopy. *Biochemistry* **2003**, *42* (4), 991-999, Article. DOI: 10.1021/bi0268908.

(89) Shen, Z.; Burrows, P. E.; Forrest, S. R.; Ziari, M.; Steier, W. H. Electroabsorption Due to Exictons In Crystalline Molecular Thin-Films Grown by Organic Molecular-Beam Deposition. *Chemical Physics Letters* **1995**, *236* (1-2), 129-134, Article. DOI: 10.1016/0009-2614(95)00195-a.

(90) Jones, B. A.; Facchetti, A.; Wasielewski, M. R.; Marks, T. J. Tuning orbital energetics in arylene diimide semiconductors. Materials design for ambient stability of n-type charge transport. *Journal of the American Chemical Society* **2007**, *129* (49), 15259-15278, Review. DOI: 10.1021/ja075242e.

(91) Houari, Y.; Laurent, A. D.; Jacquemin, D. Spectral Signatures of Perylene Diimide Derivatives: Insights From Theory. *Journal of Physical Chemistry C* **2013**, *117* (42), 21682-21691, Article. DOI: 10.1021/jp407104m.

- (92) Kong, F.; Lin, M. Q.; Qiu, T. The effect of imide substituents on the optical properties of perylene diimide derivatives. *Luminescence* **2018**, *33* (7), 1209-1216, Article. DOI: 10.1002/bio.3537.
- (93) Zhang, F. X.; Ma, Y. S.; Chi, Y. H.; Yu, H. H.; Li, Y. N.; Jiang, T. Y.; Wei, X. F.; Shi, J. M. Self-assembly, optical and electrical properties of perylene diimide dyes bearing unsymmetrical substituents at bay position. *Scientific Reports* **2018**, *8*, 11, Article. DOI: 10.1038/s41598-018-26502-5.
- (94) Mattson, M. A.; Green, T. D.; Lake, P. T.; McCullagh, M.; Krummel, A. T. Elucidating Structural Evolution of Perylene Diimide Aggregates Using Vibrational Spectroscopy and Molecular Dynamics Simulations. *Journal of Physical Chemistry B* **2018**, *122* (18), 4891-4900, Article. DOI: 10.1021/acs.jpcc.8b02355.
- (95) Reichardt, C. SOLVATOCHROMIC DYES AS SOLVENT POLARITY INDICATORS. *Chemical Reviews* **1994**, *94* (8), 2319-2358, Review. DOI: 10.1021/cr00032a005.
- (96) Diehl, F. P.; Roos, C.; Jankowiak, H. C.; Berger, R.; Kohn, A.; Diezemann, G.; Basche, T. Combined Experimental and Theoretical Study of the Vibronic Spectra of Perylenecarboximides. *Journal of Physical Chemistry B* **2010**, *114* (4), 1638-1647, Article. DOI: 10.1021/jp909862x.
- (97) Aldongarov, A.; Barashkov, N. N.; Irgibaeva, I. S. Calculated spectral properties of perylene orange, perylene red, and their complex with sodium azide. *International Journal of Quantum Chemistry* **2007**, *107* (13), 2331-2342, Article; Proceedings Paper. DOI: 10.1002/qua.21312.
- (98) Sanguineti, A.; Sassi, M.; Turrisi, R.; Ruffo, R.; Vaccaro, G.; Meinardi, F.; Beverina, L. High Stokes shift perylene dyes for luminescent solar concentrators. *Chemical Communications* **2013**, *49* (16), 1618-1620, Article. DOI: 10.1039/c2cc38708e.
- (99) Zaremba, D.; Evert, R.; Kielhorn, J.; Jakobs, F.; Caspary, R.; Kowalsky, W.; Johannes, H. H. Molecular weight variations in perylene-doped poly(methyl methacrylate) for luminescent solar concentrators. *Polymer International* **2018**, *67* (9), 1179-1185, Article. DOI: 10.1002/pi.5601.
- (100) Li, Y. L.; Zhang, X. Q.; Zhang, Y. C.; Dong, R.; Luscombe, C. K. Review on the Role of Polymers in Luminescent Solar Concentrators. *Journal of Polymer Science Part a-Polymer Chemistry* **2019**, *57* (3), 201-215, Review. DOI: 10.1002/pola.29192.
- (101) Müller, F. The Flavin Redox-System and Its Biological Function. In *Topics in Current Chemistry*, Boschke, F. L. Ed.; Vol. 108; Springer-Verlag, 1983; pp 71-107.

- (102) Stankovich, M. T. Redox Properties of Flavins and Flavoproteins. In *Chemistry and Biochemistry of Flavoenzymes*, Müller, F. Ed.; Vol. I; CRC Press, 1991.
- (103) Walsh, C. Flavin Coenzymes: At the Crossroads of Biological Redox Chemistry. *Accounts of Chemical Research* **1980**, *13*, 148-155.
- (104) Bruice, T. C. Mechanisms of Flavin Catalysis. *Accounts of Chemical Research* **1980**, (13), 256-262.
- (105) Sancar, A. Structure and function of DNA photolyase and cryptochrome blue-light photoreceptors. *Chemical Reviews* **2003**, *103* (6), 2203-2237, Review. DOI: 10.1021/cr0204348.
- (106) Heyes, D. J.; Lakavath, B.; Hardman, S. J. O.; Sakuma, M.; Hedison, T. M.; Scrutton, N. S. Photochemical Mechanism of Light-Driven Fatty Acid Photodecarboxylase. *Acs Catalysis* **2020**, *10* (12), 6691-6696, Article. DOI: 10.1021/acscatal.0c01684.
- (107) Baymann, F.; Schoepp-Cothenet, B.; Duval, S.; Guiral, M.; Brugna, M.; Baffert, C.; Russell, M. J.; Nitschke, W. On the Natural History of Flavin-Based Electron Bifurcation. *Frontiers in Microbiology* **2018**, *9*, 16, Review. DOI: 10.3389/fmicb.2018.01357.
- (108) Piano, V.; Palfey, B. A.; Mattevi, A. Flavins as Covalent Catalysts: New Mechanisms Emerge. *Trends in Biochemical Sciences* **2017**, *42* (6), 457-469, Review. DOI: 10.1016/j.tibs.2017.02.005.
- (109) Yee, E. F.; Chandrasekaran, S.; Lin, C. F.; Crane, B. R. Physical methods for studying flavoprotein photoreceptors. In *New Approaches for Flavin Catalysis*, Palfey, B. A. Ed.; Methods in Enzymology, Vol. 620; Academic Press Ltd-Elsevier Science Ltd, 2019; pp 509-544.
- (110) Gauden, M.; Grinstead, J. S.; Laan, W.; van Stokkum, I. H. M.; Avila-Perez, M.; Toh, K. C.; Boelens, R.; Kaptein, R.; Van Grondelle, R.; Hellingwerf, K. J.; et al. On the Role of Aromatic Side Chains in the Photoactivation of BLUF Domains. *Biochemistry* **2007**, *46* (25), 7405-7415.
- (111) Christie, J. M.; Salomon, M.; Nozue, K.; Wada, M.; Briggs, W. R. LOV (light, oxygen, or voltage) domains of the blue-light photoreceptor phototropin (nph1): Binding sites for the chromophore flavin mononucleotide. *Proceedings of the National Academy of Sciences of the United States of America* **1999**, *96* (15), 8779-8783, Article. DOI: 10.1073/pnas.96.15.8779.
- (112) Cashmore, A. R.; Jarillo, J. A.; Wu, Y.-J.; Liu, D. Cryptochromes: Blue Light Receptors for Plants and Animals. *Science* **1999**, *284*, 760-765.

- (113) Hitomi, K.; Okamoto, K.; Daiyasu, H.; Miyashita, H.; Iwai, S.; Toh, H.; Ishiura, M.; Todo, T. Bacterial cryptochrome and photolyase: characterization of two photolyase-like genes of *Synechocystis* sp PCC6803. *Nucleic Acids Research* **2000**, *28* (12), 2353-2362, Article. DOI: 10.1093/nar/28.12.2353.
- (114) Ghisla, S.; Massey, V. Mechanisms of flavoprotein-catalyzed Reactions. *European Journal of Biochemistry* **1989**, *181*, 1-17.
- (115) Mueller, R. M.; North, M. A.; Hati, C. Y. S.; Bhattacharyya, S. Interplay of Flavin's Redox States and Protein Dynamics: An Insight from QM/MM Simulations of Dihyronicotinamide Riboside Quinone Oxidoreductase 2. *Journal of Physical Chemistry B* **2011**, *115* (13), 3632-3641, Article. DOI: 10.1021/jp1107922.
- (116) Frago, S.; Goni, G.; Herguedas, B.; Peregrina, J. R.; Serrano, A.; Perez-Dorado, I.; Molina, R.; Gomez-Moreno, C.; Hermoso, J. A.; Martinez-Julvez, M.; et al. Tuning of the FMN binding and oxido-reduction properties by neighboring side chains in *Anabaena* flavodoxin. *Archives of Biochemistry and Biophysics* **2007**, *467* (2), 206-217, Article. DOI: 10.1016/j.abb.2007.08.024.
- (117) Bhattacharyya, S.; Stankovich, M. T.; Truhlar, D. G.; Gao, J. L. Combined quantum mechanical and molecular mechanical simulations of one- and two-electron reduction potentials of flavin cofactor in water, medium-chain acyl-CoA dehydrogenase, and cholesterol oxidase. *Journal of Physical Chemistry A* **2007**, *111* (26), 5729-5742, Article; Proceedings Paper. DOI: 10.1021/jp071526+.
- (118) Ishikita, H. Contributions of protein environment to the reduction potentials of flavin-containing proteins. In *Handbook of Flavoproteins: Complex Flavoproteins, Dehydrogenases and Physical Methods, Vol 2*, Hille, R., Miller, S., Palfey, B. Eds.; Walter De Gruyter GmbH, 2013; pp 321-333.
- (119) Ishikita, H. Redox potential difference between *Desulfovibrio vulgaris* and *Clostridium beijerinckii* flavodoxins. *Biochemistry* **2008**, *47* (15), 4394-4402, Article. DOI: 10.1021/bi702151k.
- (120) Bruggeman, Y. E.; Honegger, A.; Kreuwel, H.; Visser, A.; Laane, C.; Schots, A.; Hilhorst, R. Regulation of the flavin redox potential by flavin-binding antibodies. *European Journal of Biochemistry* **1997**, *249* (2), 393-400, Article. DOI: 10.1111/j.1432-1033.1997.00393.x.
- (121) Christgen, S. L.; Becker, S. M.; Becker, D. F. Methods for determining the reduction potentials of flavin enzymes. In *New Approaches for Flavin Catalysis*, Palfey, B. A. Ed.; Methods in Enzymology, Vol. 620; Academic Press Ltd-Elsevier Science Ltd, 2019; pp 1-25.
- (122) Nelson, D. L.; Cox, M. M. *Principles of Biochemistry*; W. H. Freeman, 2000.

- (123) Daugherty, A. B.; Govindarajan, S.; Lutz, S. Improved Biocatalysts from a Synthetic Circular Permutation Library of the Flavin-Dependent Oxidoreductase Old Yellow Enzyme. *Journal of the American Chemical Society* **2013**, *135* (38), 14425-14432, Article. DOI: 10.1021/ja4074886.
- (124) Pedotti, M.; Rosini, E.; Molla, G.; Moschetti, T.; Savino, C.; Vallone, B.; Pollegioni, L. Glyphosate Resistance by Engineering the Flavoenzyme Glycine Oxidase. *Journal of Biological Chemistry* **2009**, *284* (52), 36415-36423, Article. DOI: 10.1074/jbc.M109.051631.
- (125) Hulley, M. E.; Toogood, H. S.; Fryszkowska, A.; Mansell, D.; Stephens, G. M.; Gardiner, J. M.; Scrutton, N. S. Focused Directed Evolution of Pentaerythritol Tetranitrate Reductase by Using Automated Anaerobic Kinetic Screening of Site-Saturated Libraries. *Chembiochem* **2010**, *11* (17), 2433-2447, Article. DOI: 10.1002/cbic.201000527.
- (126) Toogood, H. S.; Fryszkowska, A.; Hulley, M.; Sakuma, M.; Mansell, D.; Stephens, G. M.; Gardiner, J. M.; Scrutton, N. S. A Site-Saturated Mutagenesis Study of Pentaerythritol Tetranitrate Reductase Reveals that Residues 181 and 184 Influence Ligand Binding, Stereochemistry and Reactivity. *Chembiochem* **2011**, *12* (5), 738-749, Article. DOI: 10.1002/cbic.201000662.
- (127) Hall, M.; Bommarius, A. S. Enantioenriched Compounds via Enzyme-Catalyzed Redox Reactions. *Chemical Reviews* **2011**, *111* (7), 4088-4110, Review. DOI: 10.1021/cr200013n.
- (128) Padhi, S. K.; Bougioukou, D. J.; Stewart, J. D. Site-Saturation Mutagenesis of Tryptophan 116 of *Saccharomyces pastorianus* Old Yellow Enzyme Uncovers Stereocomplementary Variants. *Journal of the American Chemical Society* **2009**, *131* (9), 3271-3280, Article. DOI: 10.1021/ja8081389.
- (129) Reich, S.; Hoeffken, H. W.; Rosche, B.; Nestl, B. M.; Hauer, B. Crystal Structure Determination and Mutagenesis Analysis of the Ene Reductase NCR. *Chembiochem* **2012**, *13* (16), 2400-2407, Article. DOI: 10.1002/cbic.201200404.
- (130) Kabir, M. P.; Orozco-Gonzalez, Y.; Gozem, S. Electronic spectra of flavin in different redox and protonation states: a computational perspective on the effect of the electrostatic environment. *Physical Chemistry Chemical Physics* **2019**, *21* (30), 16526-16537, Article. DOI: 10.1039/c9cp02230a.
- (131) Stanley, R. J.; Jang, H. Electronic structure measurements of oxidized flavins and flavin complexes using stark-effect spectroscopy. *Journal of Physical Chemistry A* **1999**, *103* (45), 8976-8984, Article. DOI: 10.1021/jp991811w.

- (132) Kodali, G.; Siddiqui, S. U.; Stanley, R. J. Charge Redistribution in Oxidized and Semiquinone E. coli DNA Photolyase upon Photoexcitation: Stark Spectroscopy Reveals a Rationale for the Position of Trp382. *Journal of the American Chemical Society* **2009**, *131* (13), 4795-4807.
- (133) Ponder, M.; Mathies, R. Excited-State Polarizabilities and Dipole Moments of Diphenylpolyenes and Retinal. *Journal of Physical Chemistry* **1983**, *87* (25), 5090-5098, Article. DOI: 10.1021/j150643a010.
- (134) Cerda, J. F.; Koder, R. L.; Lichtenstein, B. R.; Moser, C. M.; Miller, A. F.; Dutton, P. L. Hydrogen bond-free flavin redox properties: managing flavins in extreme aprotic solvents. *Organic & Biomolecular Chemistry* **2008**, *6* (12), 2204-2212, Article. DOI: 10.1039/b801952e.
- (135) Stanley, R. J.; van Galen, C. J. Measuring electronic structure properties of flavins and flavoproteins by electronic Stark spectroscopy. In *New Approaches for Flavin Catalysis*, Palfey, B. A. Ed.; Methods in Enzymology, Vol. 620; Academic Press Ltd-Elsevier Science Ltd, 2019; pp 215-250.
- (136) Pauszek, R. F.; Stanley, R. J. A "How-To" Guide to the Stark Spectroscopy of Flavins and Flavoproteins. In *Flavins and Flavoproteins: Methods and Protocols*, Weber, S., Schleicher, E. Eds.; Methods in Molecular Biology, Vol. 1146; Humana Press Inc, 2014; pp 443-466.
- (137) *MatLab R2018A*; The MathWorks Inc.: Natick, MA, USA, 2018.
- (138) *Spectragryph-optical spectroscopy software, Version 1.2, 2020*; F. Menges Software Development: Oberstdorf, Germany, 2020.
- (139) *Gaussian 16 Rev. C.01*; Gaussian, Inc.: Wallingford, CT, USA, 2016.
- (140) Locknar, S. A.; Peteanu, L. A.; Shuai, Z. G. Calculation of ground and excited state polarizabilities of unsubstituted and donor/acceptor polyenes: A comparison of the finite-field and sum-over-states methods. *Journal of Physical Chemistry A* **1999**, *103* (14), 2197-2201, Article. DOI: 10.1021/jp9831381.
- (141) *GaussView, Version 6.0*; Semichem, Inc.: Shawnee Mission, KS, 2016.
- (142) Koziol, J. Studies on Flavins in Organic Solvents-I.* Spectral Characteristics of Riboflavin, Riboflavin Tetrabutryrate and Lumichrome. *Photochemistry and Photobiology* **1965**, *5*, 41-54.
- (143) Sikorska, E.; Sikorski, M.; Steer, R. P.; Wilkinson, F.; Worrall, D. R. Efficiency of singlet oxygen generation by alloxazines and isoalloxazines. *Journal of the Chemical Society-Faraday Transactions* **1998**, *94* (16), 2347-2353. DOI: 10.1039/a802340i.

- (144) Penzkofer, A. Absorption and emission spectroscopic investigation of alloxazine in aqueous solutions and comparison with lumichrome. *Journal of Photochemistry and Photobiology a-Chemistry* **2016**, *314*, 114-124. DOI: 10.1016/j.jphotochem.2015.08.011.
- (145) Zeng, J.; Eckenrode, H. M.; Dounce, S. M.; Dai, H. L. Time-Resolved Molecular Transport across Living Cell Membranes. *Biophysical Journal* **2013**, *104* (1), 139-145, Article. DOI: 10.1016/j.bpj.2012.11.3814.
- (146) Moreaux, L.; Sandre, O.; Mertz, J. Membrane imaging by second-harmonic generation microscopy. *Journal of the Optical Society of America B-Optical Physics* **2000**, *17* (10), 1685-1694, Article. DOI: 10.1364/josab.17.001685.
- (147) Oudar, J. L. Optical Nonlinearities Of Conjugated Molecules - Stilbene Derivatives And Highly Polar Aromatic-Compounds. *Journal of Chemical Physics* **1977**, *67* (2), 446-457. DOI: 10.1063/1.434888.
- (148) Karki, L.; Vance, F. W.; Hupp, J. T.; LeCours, S. M.; Therien, M. J. Electronic Stark Effect Studies of a Porphyrin-Based Push-Pull Chromophore Displaying a Large First Hyperpolarizability: State-Specific Contributions to β . *Journal of the American Chemical Society* **1998**, *120* (11), 2606-2611.
- (149) Willetts, A.; Rice, J. E.; Burland, D. M.; Shelton, D. P. Problems in the Comparison of Theoretical and Experimental Hyperpolarizabilities. *Journal of Chemical Physics* **1992**, *97* (10), 7590-7599. DOI: 10.1063/1.463479.
- (150) Marder, S. R.; Beratan, D. N.; Cheng, L. T. Approaches For Optimizing the 1st Electronic Hyperpolarizability Of Conjugated Organic-Molecules. *Science* **1991**, *252* (5002), 103-106, Article. DOI: 10.1126/science.252.5002.103.
- (151) Campagnola, P. J.; Wei, M. D.; Lewis, A.; Loew, L. M. High-resolution nonlinear optical imaging of live cells by second harmonic generation. *Biophysical Journal* **1999**, *77* (6), 3341-3349. DOI: 10.1016/s0006-3495(99)77165-1.
- (152) Albert, I. D. L.; Marks, T. J.; Ratner, M. A. Remarkable NLO response and infrared absorption in simple twisted molecular π -chromophores. *Journal of the American Chemical Society* **1998**, *120* (43), 11174-11181, Article. DOI: 10.1021/ja982073c.
- (153) McHale, J. L. *Molecular Spectroscopy*; Prentice Hall, 1999.
- (154) Mohammed, N.; Wiles, A. A.; Belsley, M.; Fernandes, S. S. M.; Cariello, M.; Rotello, V. M.; Raposo, M. M. M.; Cooke, G. Synthesis and characterisation of push-pull flavin dyes with efficient second harmonic generation (SHG) properties. *Rsc Advances* **2017**, *7* (39), 24462-24469. DOI: 10.1039/c7ra03400h.

- (155) Richtar, J.; Heinrichova, P.; Apaydin, D. H.; Schmiedova, V.; Yumusak, C.; Kovalenko, A.; Weiter, M.; Sariciftci, N. S.; Krajcovic, J. Novel Riboflavin-Inspired Conjugated Bio-Organic Semiconductors. *Molecules* **2018**, *23* (9), 18, Article. DOI: 10.3390/molecules23092271.
- (156) Rinuy, J.; Brevet, P. F.; Girault, H. H. Second Harmonic Generation of Glucose Oxidase at the Air/Water Interface. *Biophysical Journal* **1999**, *77*, 3350-3355.
- (157) Houk, A. L.; Zheldakov, I. L.; Tommey, T. A.; Elles, C. G. Two-Photon Excitation of trans-Stilbene: Spectroscopy and Dynamics of Electronically Excited States above S-1. *Journal of Physical Chemistry B* **2015**, *119* (29), 9335-9344, Article. DOI: 10.1021/jp509959n.
- (158) Tomasi, J.; Mennucci, B.; Cammi, R. Quantum mechanical continuum solvation models. *Chemical Reviews* **2005**, *105* (8), 2999-3093, Review. DOI: 10.1021/cr9904009.
- (159) *GaussView, Version 6.1*; Semichem, Inc.: Shawnee Mission, KS, 2016. (accessed.
- (160) Locknar, S. A.; Peteanu, L. A.; Shuai, Z. Calculation of Ground and Excited State Polarizabilities of Unsubstituted and Donor/Acceptor Polyenes: A Comparison of the Finite-Field and Sum-Over-States Methods. *J. Phys. Chem. A* **1999**, *103* (14), 2197-2201.
- (161) Aubret, A.; Orrit, M.; Kulzer, F. Understanding Local-Field Correction Factors in the Framework of the Onsager-Bottcher Model. *Chemphyschem* **2019**, *20* (3), 345-355, Review. DOI: 10.1002/cphc.201800923.
- (162) Ponder, M.; Mathies, R. Excited-State Polarizabilities and Dipole-Moments of Diphenylpolyenes and Retinal. *Journal of Physical Chemistry* **1983**, *87* (25), 5090-5098, Article. DOI: 10.1021/j150643a010.
- (163) Langhals, H.; Kinzel, S. Thermochromism of perylenes: Dynamics in aromatics. *Spectrochimica Acta Part a-Molecular and Biomolecular Spectroscopy* **2011**, *78* (3), 1212-1214, Article. DOI: 10.1016/j.saa.2010.12.033.
- (164) Mitroy, J.; Safronova, M. S.; Clark, C. W. Theory and applications of atomic and ionic polarizabilities. *Journal of Physics B-Atomic Molecular and Optical Physics* **2010**, *43* (20), 38, Review. DOI: 10.1088/0953-4075/43/20/202001.
- (165) Rabe, E. J.; Goldwyn, H. J.; Hwang, D.; Masiello, D. J.; Schlenker, C. W. Intermolecular Hydrogen Bonding Tunes Vibronic Coupling in Heptazine Complexes. *Journal of Physical Chemistry B* **2020**, *124* (51), 11680-11689, Article. DOI: 10.1021/acs.jpcc.0c07719.
- (166) Mulliken, R. S.; Person, W. B. *Molecular Complexes*; Wiley-Interscience, 1969.

- (167) Kee, J.; Ok, K. M. Hydrogen-Bond-Driven Synergistically Enhanced Hyperpolarizability: Chiral Coordination Polymers with Nonpolar Structures Exhibiting Unusually Strong Second-Harmonic Generation. *Angewandte Chemie-International Edition* **2021**, *60* (38), 20656-20660, Article. DOI: 10.1002/anie.202106812.
- (168) Reichardt, C. Solvatochromic Dyes As Solvent Polarity Indicators. *Chemical Reviews* **1994**, *94* (8), 2319-2358, Review. DOI: 10.1021/cr00032a005.
- (169) Onsager, L. Electric moments of molecules in liquids. *Journal of the American Chemical Society* **1936**, *58*, 1486-1493, Article. DOI: 10.1021/ja01299a050.
- (170) Koziol, L.; Kumar, N.; Wong, S. E.; Lightstone, F. C. Molecular Recognition of Aromatic Rings by Flavin: Electrostatics and Dispersion Determine Ring Positioning above Isoalloxazine. *Journal of Physical Chemistry A* **2013**, *117* (48), 12946-12952, Article. DOI: 10.1021/jp407193c.
- (171) Fox, K. M.; Karplus, P. A. Old yellow enzyme at 2 Å resolution: Overall structure, ligand binding, and comparison with related flavoproteins. *Nature Structure (London)* **1994**, *2* (11), 1089-1105.
- (172) Park, H.-W.; Kim, S.-T.; Sancar, A.; Deisenhofer, J. Crystal structure of DNA photolyase from *Escherichia coli*. *Science* **1995**, *268* (5219), 1866-1872.
- (173) Breinlinger, E.; Niemz, A.; Rotello, V. M. Model Systems for Flavoenzyme Activity. Stabilization of the Flavin Radical Anion through Specific Hydrogen Bond Interactions. *Journal of the American Chemical Society* **1995**, *117* (19), 5379-5380.
- (174) Cuello, A. O.; McIntosh, C. M.; Rotello, V. M. Model systems for flavoenzyme activity. The role of N(3)-H hydrogen bonding in flavin redox processes. *Journal of the American Chemical Society* **2000**, *122* (14), 3517-3521, Article. DOI: 10.1021/ja994204v.
- (175) Walsh, C. Flavin Coenzymes - At the Crossroads of Biological Redox Chemistry. *Accounts of Chemical Research* **1980**, *13* (5), 148-155, Review. DOI: 10.1021/ar50149a004.
- (176) Eaton, W. A.; Hofrichter, J.; Makinen, M. W.; Andersen, R. D.; Ludwig, M. L. Optical Spectra and Electronic Structure of Flavine Mononucleotide in Flavodoxin Crystals. *Biochemistry* **1975**, *14* (10), 2146-2151.
- (177) Maestre-Reyna, M.; Yang, C. H.; Nango, E.; Huang, W. C.; Putu, E.; Wu, W. J.; Wang, P. H.; Franz-Badur, S.; Saft, M.; Emmerich, H. J.; et al. Serial crystallography captures dynamic control of sequential electron and proton transfer events in a flavoenzyme. *Nature Chemistry* **2022**, *14* (6), 677-+, Article. DOI: 10.1038/s41557-022-00922-3.

(178) Pettersen, E. F.; Goddard, T. D.; Huang, C. C.; Couch, G. S.; Greenblatt, D. M.; Meng, E. C.; Ferrin, T. E. UCSF chimera - A visualization system for exploratory research and analysis. *Journal of Computational Chemistry* **2004**, *25* (13), 1605-1612, Article. DOI: 10.1002/jcc.20084.

(179) Zaluga, C.; Spata, V.A.; Matsika, S. Benchmarking Quantum Mechanical Methods for the Description of Charge-Transfer States in pi-Stacked Nucleobases. *Journal of Chemical Theory and Computation*. **2021**, *17*, 376-387, Article. DOI: 10.1021/acs.jctc.0c00973.